Stretchable Electronic and Photonic Materials from Self-Organized Nanoparticles

by

Yoonseob Kim

A dissertation submitted in partial fulfillment
of the requirements for the degree of
Doctor of Philosophy
(Chemical Engineering)
in the University of Michigan
2016

Doctoral Committee:

Professor Nicholas A. Kotov, Chair
Professor Ellen M. Arruda
Doctor Oriol Arteaga, University of Barcelona
Professor L. Jay Guo
Professor Jinsang Kim
Professor Joerg Lahann

To my parents and sister, for their support and love

ACKNOWLEDGEMENTS

This work would not have been possible without generous guidance and support from a great number of individuals. There is no way that I can express my full gratitude to everyone who has helped me, but I do sincerely appreciate all the help and friendship I have received from each of you. Specifically, I would like to thank my research advisor, Prof. Nicholas A. Kotov, for providing incredible support and guidance both in and out of the research setting. I have thoroughly enjoyed doing this research, and the encouragement, generosity, creativity and criticism I received has made all of the work that went into this a true joy. I would also like to thank my thesis committee, Prof. Ellen M. Arruda, Prof. L. Jay Guo, Prof. Jinsang Kim, Prof. Joerg Lahann, and Dr. Oriol Arteaga, for helpful guidance and insightful feedback during the entire thesis process. Their supports were critical honing my thesis work. I also would like to thank my undergraduate advisor Prof. Adam J. Matzger and my mentor Dr. Kyoungmoo Koh. Without their support, I would never have realized the opportunity to pursue a doctoral degree.

I have had the distinct pleasure of working with many exemplary students, post-doctoral fellows, and professors while performing this thesis research, without whom this all would have been much more difficult and much less enjoyable. I would like to express my sincere gratitude to my fellow group members for helping shape me into the scientist that I am today. I would like to thank Bongjun Yeom, Jian Zhu, Gleiciani Silveira, Huanan Zhang, Jing Lyu, Joong Hwan Bahng, Kyounggun Lee, Liguang Xu, Lizhi Xu, Ming Yang, Seongil Yoo, Shuang Jiang, Siu On Tung, Wonjin Choi, Christine Andres, Dawei Li, and Yiding Liu. I am grateful for Bongjun Yeom, whose expertise, dialogue and arguments benefited and honed this

research. Of the particular mention is Jian Zhu, without whose dedicated mentorship and supportive friendship I would not have navigated to this place of scientific achievement. I will cherish the friendship that we have developed for years to come. Thank you my mentees, Dengwu Zhao, Zhou Chang, Benjamin Catalano, Camille King, Shobhita Kramadhati, Katie Mills, Ceren özbay, and Lee Sin Lim, for being patient with me and for teaching me more than I could have imagined. I have fully enjoyed working with each of you. To those who I have had the opportunity of collaborating with, thank you for allowing me to explore the broader applications of my thesis research and for strengthening the work therein: Dr. Oriol Arteaga (University of Barcelona, Spain), Prof. Ctirad Uher (U-M), Prof. Jang Wook Choi (KAIST, Korea), Prof. Pierre Schaaf (Institut Charles Sadron, France), Prof. Robert Ziff (U-M).

This work is also dependent upon financial support from a number of funding agencies including the STX foundation in Seoul, Korea, a Rackham Predoctoral Fellowship at the University of Michigan, and funding from the National Science Foundation, the Air Force Office of Scientific Research, the US Department of Energy, and the US Department of Defense. I am also grateful to the Korean-American Scientists and Engineers Association and the Korea-US Science Cooperation Center for a scholarship, and to the Korean Institute of Chemical Engineers for a Doh Wonsuk Memorial Award.

Finally, I would like to thank my close friends and family for their support and encouragement throughout my journey, especially during the past six years. To my roommates Dongkyoung Lee and Youngkook Hwang, thank you for your great friendship and for bringing enjoyment to my life outside of a laboratory. To the staff members of the Korean Student Association – Graduate (KSAG) at the U-M, including D. L. and Y. K.: without you

my life in Ann Arbor would be utterly “monotonic”. I am also very proud that we, KSAG, contributed significantly as a member of the Ann Arbor community. To my parents Donghwan Kim and Youngsook Lee, thank you so much for all of the tremendous love and support you have given me throughout my life and for fostering my early desires that allowed me to accomplish this. To my sister, Hyojin Kim, thank you for teaching me the importance and value of family that is an intrinsic aspect of who I have become. Without all of you, I would not be the person that I am today.

TABLE OF CONTENTS

LIST OF FIGURES

ABSTRACT

Nanoscale science and technologies have been developed tremendously during the last two decades, introducing a variety of nanomaterials with unique properties. However, incorporation of these properties into macroscale functional applications has been limited. An essential challenge is the integration of such unique properties into assemblies for macroscale devices. Here we explore self-organization of nanomaterials in solid-state for discovering fundamental understandings of mechanisms and dynamics for various engineering applications.

An example of excellent stretchable conductors from self-organization of nanoparticles (NPs) was first demonstrated. Free-standing stretchable conductors were prepared using layer-by-layer (LBL) assembly and vacuum-assisted flocculation (VAF). Different properties of LBL and VAF were understood from the perspective of structure and property relations. High conductivity and stretchability were observed from both composites, and the properties originated from dynamic self-organization of NPs. Modified percolation theory allowed incorporation of the self-organization and provided an excellent match with experimental data. Stretchable and conductive composites under voltage application provided an additional practical aspect of the composites, damping of vibrations.

Another self-organization of NPs first demonstrated chiroptical nanocomposites for applications of photonic material devices and optoelectronics. They were also LBL assembled, from plasmonic NPs and single-walled carbon nanotubes (SWNTs). A straightforward sample preparation method, conformal deposition of plasmonic materials on pre-twisted substrates, is a distinctive advantage when producing macroscale photonic materials. Chiroptical activities

can be increased up to ten fold and were reversibly tunable. S-like 3D nano-assemblies were responsible for the optical activities and this was confirmed by computational simulations. Universality of the method was confirmed by introducing polymeric fluorescence beads and SWNTs. Deposition of SWNTs expanded the wavelength regimes from UV to near-IR.

Solid-state self-organization at the nexus of mechanics, electronics, and excitonics/plasmonics can be generalized to other nanoscale materials and opens new possibilities for composite-based electronic and optic devices.

CHAPTER I

Introduction

1.1 Motivation: Technological Convergence

Research in nanotechnology has been extremely active during the past three decades, introducing a library of building blocks with unique features under a given size into ultra-precisely assembled supraparticles demonstrating novel behaviors. Discovery of new categories of assembled materials, which are often active and complex, and fundamental understandings of their systems, has triggered innovations in interdisciplinary research. These innovations have recently focused upon advanced performance and new domains for applications including nano-electronics and -photonics, efficient energy conversion and storage, neuro- and cognitive-science, therapeutic pharmacology, and national security[1,2,3,4,5].

These unprecedented advancements have clearly been fueled by various assembly and patterning tools because technology integration invariably begins with the ability to manipulate material building blocks, often in nanoscale. Such tools include bottom-ups, e.g. layer-by-layer (LBL) assemblies, self-assembled monolayers, Langmuir-Blodgett method, DNA origami, etc., and top-downs, e.g. various lithography techniques, various vapor deposition methods, etc.[6]. Each has contributed tremendously in the development of nanotechnologies with unique advantages and disadvantages. However, the most versatile, economically viable,

environmentally benign method at the forefront of technological convergence is LBL assembly[7,8,9,10].

1.2 Moving Forward with Layer-by-Layer Assembly

After its introduction by Gero Decher and co-workers in 1991[11], LBL assembly, a multilayer thin film assembly method, has marked itself as the most versatile method assembling nano- and micro-scale materials as well as fine-tuning its properties (Fig. 1.1). It is undergoing exponential growth both in terms of furnishing novel fundamental mechanisms and new material building blocks. LBL assembly's extensive freedom to employ a myriad of materials and substrates unlimited by dimensionality is the primary reason for its success. Materials can range from small molecules, inorganic particles and synthetic polymers to biomolecules, and substrates just as easily take complex form as spherical form. Thereby, the ability of precise control in nanoscale composition across thickness (thickness of the layers can be readily controlled by varying the number of deposition cycles) has attracted many researchers into the field. This controllability subsequently means that material properties of assembled layers can be fine-tuned as desired. LBL assembled thin films are engineered to have properties including, but not limited to, electro-mechanical, nano-photonic, electro-chemical, electro-neural, and pharmacological. Water-based environmentally benign processes and cost-effective experimental setups offer additional benefit for commercialization[12,13,14].

Initially LBL assemblies were used to deposit oppositely charged synthetic polyelectrolytes on planar substrates[11]. Eventually the method grew to include all kinds of

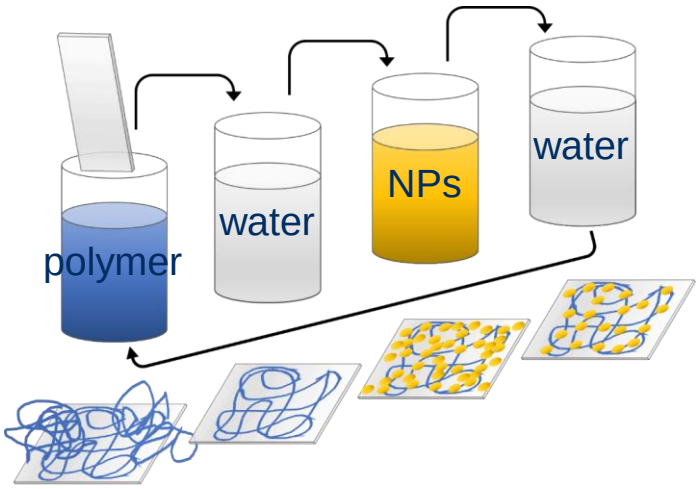

Figure 1.1. Schematic of layer-by-layer assembly. Polymer and nanoparticles are sequentially deposited on the substrate by dipping method.

organic and inorganic nano/micro building blocks[15,10,16,17] on substrates with various dimensionalities. Even binder-free LBL assemblies demonstrated novel properties[18,19]. At the same time, various multilayer deposition mechanisms, other than electrostatic attraction such as hydrogen bonding[20,21], covalent bonding[22], hydrophobic interactions[23] and click chemistry[24,25], are unveiled widening applicability LBL assembly into related fields[26,27,28,29,30]. Multifarious deposition technologies are also introduced such as dipping, spraying, fluidic, spin-coating, and electromagnetic, which are expected to bring different internal structures and thus different material properties[31,32]. With the help of advanced analytical tools, LBL-based nanotechnology paves the way for making advanced nanocomposites for myriad novel applications.

Based on past contributions from many researchers in the LBL community, the field is now enjoying matured knowledge. Now, the paradigms of the field are fast shifting toward how we can use our expanded information to make real impacts to improve personal quality of life. Equipped with a better understanding on nano/micro materials, we have sufficient ability

for this grand challenge. By converging technologies, which we define as having synergistic functionalities from different disciplines, with LBL assembly, we can address vital human needs with new applications. LBL assembly is now ready to create transformative materials and devices.

Four of the most advantageous qualities of LBL assemblies are their ability to construct highly integrated multilayer structures[33], their non-toxic water-based nature[29], their ability to work at room temperature, and the fact that they lend themselves to large scale production at a low cost with a short preparation time[13]. These qualities are proving invaluable when addressing various converging technologies. For instance, electronic and energy materials require qualities of high electron and ion exchange rate. Additionally, the full potential of photonic materials are restricted by the method of lithography which dramatically limits device size and production scale[34]. Further, in the case of neural probes, the high temperature required by chemical vapor deposition restrains the choice of materials considerably limiting performance[6]. Also, pharmacological applications will be benefited from a purely aqueous means for creating drug-carrier complexes[35].

1.3 Thesis Overview

To address the grand challenge and achieve realistic goals, we will pay special attention to the phenomena and fundamentals of self-organization of NPs as a response to external stresses for advanced properties for practical applications into the areas of, including not limited to, stretchable conductors (electro-mechanical systems) and reconfigurable photonic materials

(nano-photonics)[36–39]. The emergent behavior of self-organized NPs is an important direction for future research since it demonstrates generalizable possibilities of making materials with properties overcoming classical limits or unprecedented tunable functionalities.

1.3.1 A Model System: Gold Nanoparticles and Polyurethane

As a model system, we chose citrate-stabilized highly monodisperse gold NPs 13.0 ± 0.3 nm in diameter (Fig. 1.2a). Smaller NPs (< 10 nm) tend to easily aggregate due to high surface-to-volume ratio and larger NPs (> 16 nm) normally have low monodispersity. The thin citrate layer on the surface of the NPs makes them negatively charged. The use of citrate for colloidal stabilization of gold NPs is expected to bring about minimal barriers for charge transport between nanoparticles (Fig. 1.2b), which is not the case of gold nanoparticles with stabilizers with long aliphatic chains, e.g. oleylamine and 1,6-hexanedithiol (Table 1.1).

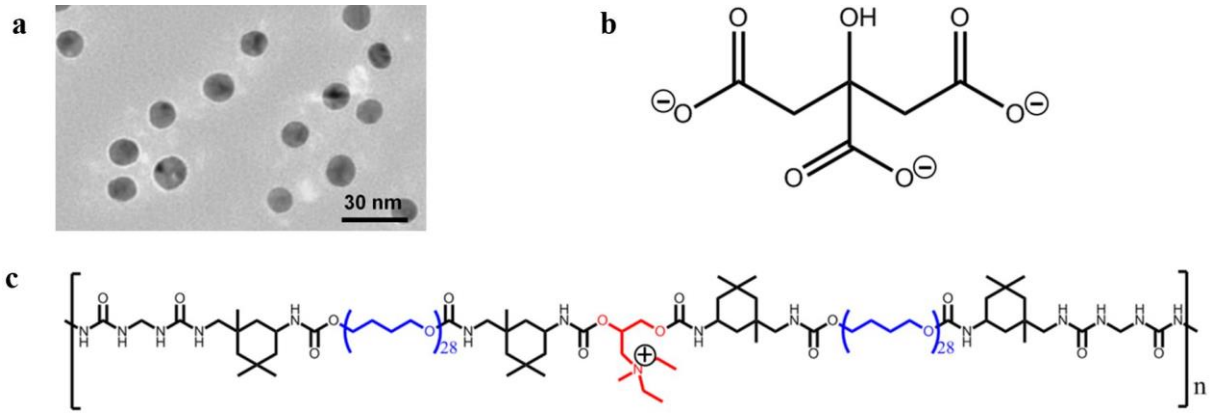

Figure 1.2. a, TEM image of gold nanoparticles. **b**, **c**, Chemical structures of anionic citrate and cationic polyurethane copolymer, respectively.

Table 1.1. Previous cases of LBL films from Au NPs and their conductivity.

Diameter of Au NP (nm)	**Stabilizer**	**Counter polyelectrolyte**	**Thickness of film (nm)**	**Conductivity (S cm^{-1}) (reference)**
5	sodium borohydride	poly(diallyldimethyl ammonium chloride)	60	2 x 10^5 (40)
13	citrate	poly(diallyldimethyl ammonium chloride)	60	1.8 x 10^5 (41)
2.5	citrate	ethanedithiol	52	2.5 x 10^5 (42)
2.5	citrate	ethylenediamine	52	2 x 10^5 (43)
9	oleylamine	1,9-nonanedithiol	60	2 x 10^{-2} (44)
10	1,6-hexanedithiol	alkanedithiol	26	3.7 x 10^{-2} (45)

Nanoparticles may initially appear as unfavorable candidates for the task of filling a polymer matrix for electrical applications. First of all, spherical nanoparticles have a percolation threshold, V_c, that is 10 to 100 times higher than high-aspect-ratio nanometer-scale components. The charge transport between nanoparticles involves a large number of nanoparticle–nanoparticle junctions, resulting in high contact resistance and scattered charge carriers. Additionally, nanoparticles with a strong attraction to polymers cause stiffening of the matrix. On the other hand, nanoparticles in a polymer matrix represent a more dynamic system that has greater freedom for reversible nanoscale restructuring, which is essential for stretchability. Although nanoparticle dynamics in a polymer matrix at high stress/strain levels are poorly understood, one should expect greater matrix mobility from nanoparticles than from nanotubes or nanowires. Therefore, the conducting pathways lost upon deformation could

potentially be recovered in a different particle configuration. It is also important that the conductance between two nanoparticles does not depend on their mutual orientation.

Polyurethane with two sets of 28 repeating units of ductile moieties (Fig. 1.2c, ca. 903 nm of main chain length) was used as a polymeric partner for these particles (1.0% by volume in aqueous solution). Its strong positive charge is complementary to the negative charge of the nanoparticles and allowed us to use LBL deposition to make corresponding composites[46,47]. The application of LBL allowed us to (1) reach high nanoparticle loadings, (2) maintain the uniformity of nanoparticle distribution throughout the material, and (3) make adequate comparisons between nanoparticle composites with different nanoscale fillers[8]. We also used an alternative method of construction, in which the nanoparticle composite materials were obtained by vacuum-assisted flocculation (VAF), allowing us to generalize the properties of nanoparticle composites as stretchable conductors.

1.3.2 Stretchable Conductors

The field of stretchable conductors is the best example where a direct combination of two seemingly disparate properties co-mingle and produce unprecedented applications. A fundamental understanding of stretchable conductors and a better utilization of them has possibilities of opening many sub-fields such as implantable bio-electronics, wearable electronics and flexible photovoltaics[48,49,50]. High performance stretchable conductors are

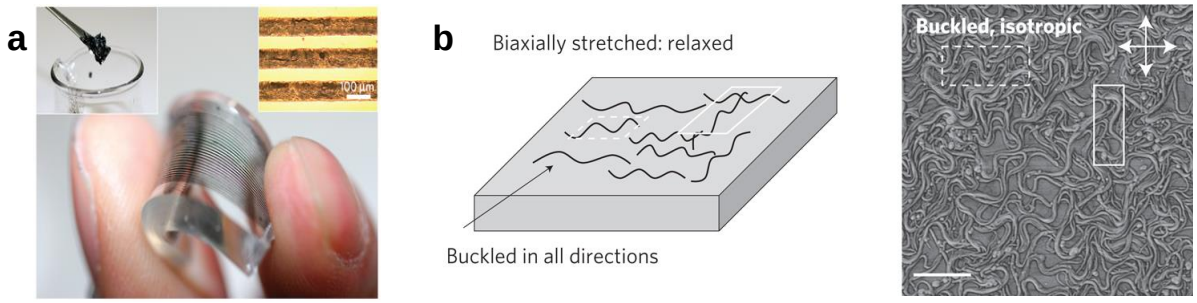

Figure 1.3. Stretchable conductors from carbon nanotubes printed (a)[53] or deposited (b) [54] on elastic rubbery substrate.

prepared from simultaneous incorporation of excellent mechanical stretchability and electronic conductivity. However, this has been very challenging due to the fact that molecular mechanisms of stretching leads to delocalized electronic orbitals.

The best known stretchable conductors have partially overcome this challenge by utilizing high aspect ratio conducting fillers such as single-walled nanotubes (SWNTs) to make promptly percolated networks[51]. Randomly mixed SWNT-polymer composite as either free-standing form or printed ink paste on elastic substrate, polydimethylsiloxane (PDMS), was demonstrated to have conductivity up to 100 S/cm (Fig. 1.3a)[52,53]. SWNTs were also spray-deposited onto PDMS substrate to allow for elastic conductivity upon tensile stretching (Fig. 1.3b)[54]. PDMS has been popularly used as a substrate due to its elastic tensile stretching and near 100% transparency in the visible spectrum. However, the use substrate brings an inherent disadvantage that stretchability is limited by that of the substrate, ca. 150 %. In order to achieve improved mechanical and electrical properties, we must address the following questions: "Can we distribute filler materials more homogeneously?", "Can we incorporate even more conductive fillers?" and "Can we control distribution state and content of fillers for fine-tuned properties?"

LBL-assembled stretchable and conductive composites answering the above questions were recently prepared[55]. Negatively-charged Au NPs distributed in positively-charged polyurethane matrix show exceptional conductivity of 1.1 x 10^4 S/cm and stretchability of 110 %. Sequential deposition enabled homogeneous deposition of the NPs. Conductivity was easily tuned by the content of NPs, by simply changing the dipping time of the substrate in the NP containing beaker. The LBL dipping method readily enabled fully interdigitated NP networks in the polymer matrix allowing for well-established percolated pathways. The fully integrated structures and flexibility of polyurethane networks offer mobility of NPs to make re-organized conductive pathways under applied strains in order to retain high conductivities. This ideal homogeneous network was a good experimental prototype for theoretical analysis. Percolation theory was applied to analyze conductive behavior of the composites with and without tensile strains. Experimentally observed conductivity under strain was higher than the theoretical limit by percolation theory due to re-organized NPs along the tensile direction. The technologically important method of VAF, even simpler and more time-efficient than LBL assembly, was introduced to make composites. VAF composites yielded exceptionally high stretchability, 480%, and high conductivity, 1,800 S/cm. This method makes internal distribution NPs more aggregated than those in the LBL samples. Thus, VAF composite had decreased conductivity but higher stretchability.

More creative converging technologies will inevitably come, not only with LBL, but also by combination with other technological methods. To the LBL-assembled conductive composites, Kirigami (a Japanese art of paper cutting) technique can be applied to introduce constant electrical properties under even higher mechanical stretching. Kirigami involves

strategically configured arrays of cuts to guide buckling/folding processes in a manner that delocalizes stresses under mechanical strain[56,57]. LBL-deposited conductive sheets adjunct to a top-down method of lithography, demonstrated composites containing nearly constant conductance up to 290% of stretching, which without Kirigami had 5% of maximum tensile stretching[58]. This stretchable but non-compromised performance enabled by Kirigami was also applied to photovoltaic panels[59].

LBL assembly may also contribute to effectively create transparent conductors, which have tremendous potential to advance technological applications such as transparent strain/pressure sensors and transparent displays. An above example of spray-deposited SWNT composites have significant transparency due to the low volumetric content of their fillers[54]. This, however, is potentially fraught with the problems of SWNT network delamination and planar-restricted substrate dimensionality. The highly versatile LBL assembly method can be applied to have comparably high conductivity and to have conformal three dimensional geometrical coating[60].

1.3.3 Reconfigurable Photonic Materials

The field of chiroptical photonic materials has rapidly emerged for the potential applications of, for example, negative-index materials that refract trajectories of light in anomalous directions, invisibility clocking that modifies the electromagnetic interactions accompanied by dramatic light confinement, chiral assemblies that rotate the polarization state of light a couple orders of magnitude stronger than those from natural organic materials, ultra-sensitive detection of biomolecules, and even fabrication of transistors[34,61,62,63,64].

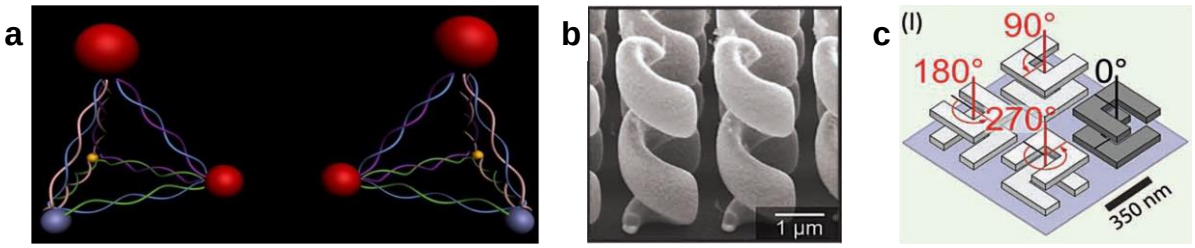

Figure 1.4. Chiroptical photonic materials prepared from the method of DNA bridge (a)[155], glancing angle deposition (b)[114], and high resolution lithography (c)[156].

This advance has benefited most from the ability to produce artificial electromagnetic media on the sub-wavelength scale using the advance of fabrication tools such as high resolution lithography[63] and vapor deposition[65] and nanoscale precision DNA origami[66]. One of the critical limitations of the above approach is that samples prepared from the above methods are restricted by the scale of DNA or lithography. Preparing samples with large scale, high throughput, low cost and short preparation time remain as challenges, and successful outcome could trigger another wave of innovation. Previous studies show the possibility that small scale photonic materials can be enlarged by using bottom-up self-assembly methods. Examples include macroscale 2D superlattices of polyhedral silver nanoparticles assembled using the Langmuir-Blodgett technique[67], ordered macroscale assemblies by a self-assembly process of sedimentation and solution evaporation[68], LBL-assembled 3D colloidal supercrystals for controllable transverse (intralayer) and longitudinal (interlayer) near-field coupling[69], and LBL-assembled fine-tuned inter-particle distance for controlled localized plasmonic coupling[70].

Recently, macroscale and reversibly tunable chiroptical nanocomposites from the straightforward preparation method of LBL assembly was demonstrated[71]. Separate strips of elastic and transparent substrates, PDMS, were twisted clockwise and counterclockwise respectively and then subjected to deposition of a few layers of Au NPs and PU on top, and

were released having planar geometry. Deposition of nanomaterials on 3D geometry and on soft rubbery substrate has strong advantages when employing the versatile deposition method of LBL assembly. This twist-deposit-release process transfers chirality from macroscale substrate to nanoscale LBL films: chiral distribution of stresses was imprinted to the interfaces of multilayers and substrate in the form of buckles. A primary technological advantage is that solid-state macroscale thin films were prepared at low cost with short preparation time. This ensures high applicability of materials.

Mueller matrix polarimetry revealed that the as-prepared planar films had modest chiroptical activities of plus and minus 50 mdeg depending on respective initial substrate twist direction. However, polarization rotation increased by ten-fold under strain of 50% due to NP chains re-organizing into curvier geometries along the *z* axis. 500 mdeg of intrinsic circular dichroism is one of the highest values reported thus far. The chiroptical activities were extremely homogeneous in macroscale and reversibly tunable in real-time up to 10,000 cycles. Homogeneous distribution of NPs throughout the polymer matrix and fully integrated internal structures should subsequently contribute to homogeneous chiroptical activity. The versatile applicability of LBL assembly enabled incorporation of SWNTs, therby widening active ranges of chiroptical responses from UV to near-IR. This proves that more diverse nanomaterials can be deposited for unprecedented applications.

This area of photonic materials from self-assembly has very recently emerged, and many creative outcomes are expected to follow. Additionally, LBL-assembled composites fabricated by a conventional method ushers in newly creative paradigms for engineering as a whole. The above example of Kirigami-applied stretchable conductors exemplifies this.

These all would result in plethora of creative engineering such as tunable circular polarization based sensors. A plethora of ingeniously engineered devices, such as tunable circular polarization based sensors, awaits.

CHAPTER II

Stretchable Nanoparticle Conductors with Self-Organized Conductive Pathways

2.1 Introduction and Background

Research in stretchable conductors is fueled by diverse technological needs. Flexible electronics, neuroprosthetic and cardiostimulating implants, soft robotics and other curvilinear systems require materials with high conductivity over a tensile strain of 100 per cent (refs [72–74]). Furthermore, implantable devices or stretchable displays[53] need materials with conductivities a thousand times higher while retaining a strain of 100 per cent. However, the molecular mechanisms that operate during material deformation and stiffening make stretchability and conductivity fundamentally difficult properties to combine. The macroscale stretching of solids elongates chemical bonds, leading to the reduced overlap and delocalization of electronic orbitals[75]. This conductivity–stretchability dilemma can be exemplified by liquid metals, in which conduction pathways are retained on large deformation but weak interatomic bonds lead to compromised strength. The best-known stretchable conductors use polymer matrices containing percolated networks of high-aspect-ratio nanometer-scale tubes or nanowires to address this dilemma to some extent[52,54,76–79]. Further improvements have been achieved by using fillers (the conductive component) with increased aspect ratio, of all-metallic composition[80], or with specific alignment (the way the fillers are arranged in the matrix)[81,82].

However, the synthesis and separation of high-aspect-ratio fillers is challenging, stiffness increases with the volume content of metallic filler, and anisotropy increases with alignment[83]. Pre-strained substrates[84,85] buckled microwires[86] and three-dimensional microfluidic polymer networks[87] have also been explored.

Here we demonstrate stretchable conductors of polyurethane containing spherical nanoparticles deposited by either LBL assembly or VAF (nanoparticles and polyurethane described in Fig. 1.2). High conductivity and stretchability were observed in both composites despite the minimal aspect ratio of the nanoparticles. These materials also demonstrate the electronic tunability of mechanical properties, which arise from the dynamic self-organization of the nanoparticles under stress. A modified percolation theory incorporating the self-assembly behavior of nanoparticles gave an excellent match with the experimental data.

2.2 Stretchable and Conductive Nanocomposites

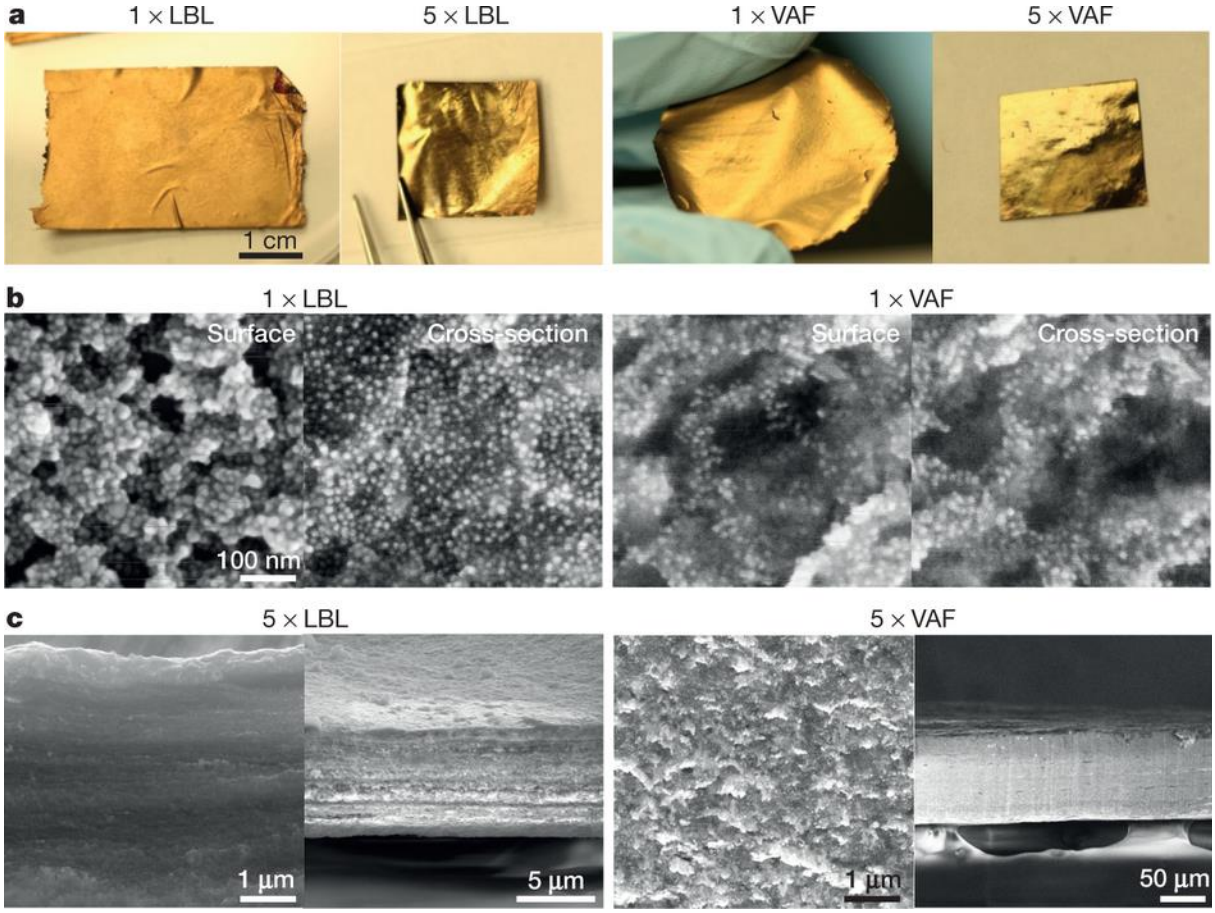

Figure 2.1. Preparation of polyurethane–nanoparticle nanocomposites. a, Photographs of a free-standing film $(PU/NP)_{500}$, a consolidated 5 × LBL stack, a free-standing film made by VAF, and a consolidated 5 × VAF stack. **b**, SEM images of 1 × LBL and 1 × VAF. **c**, Cross-sectional SEM images of 5 × LBL and 5 × VAF**.**

Free-standing composite films were obtained after 500 LBL deposition cycles and the resulting polyurethane–nanoparticle film is denoted $(PU/NP)_{500}$. Their thickness was determined by scanning electron microscopy (SEM) to be 2.0 ± 0.2 µm. The ellipsometric thickness for one to ten layer pairs gave a total thickness of 1.97 ± 0.1 µm for 500 layer pairs (Fig. 2.10a). It is nearly identical to the SEM thickness, which indicates excellent thickness

control of the LBL growth[88,89]. Similar free-standing VAF sheets had an SEM thickness of 30 ± 3.0 μm. Both LBL and VAF sheets had an unmistakably metallic appearance (Fig. 2.1a). LBL and VAF composites were made to have the same volumetric fraction of fillers V_f, 21.7 vol.% (Fig. 2.2a, 2.11). Experimentally determined values of V_c for the LBL and VAF composites were 16.2 vol.% and 17.5 vol.%, respectively. To transition to fully macroscopic materials as-prepared LBL and VAF free-standing films were laminated into stacks[90]. Hot-pressing 3–10 free-standing sheets together at 120 °C and a pressure of 20 MPa for 1 h revealed a high degree of consolidation (Fig. 2.1c). The lamination temperature was chosen because no phase change was observed up to 130 °C for all materials according to differential scanning calorimetry data (Fig. 2.12). The laminated samples of five sheets were denoted 5 × LBL or 5 × VAF and had SEM thicknesses of 6.5 ± 0.7 μm and 110 ± 10 μm, respectively.

LBL and VAF films had different properties even when the gold content was the same. The LBL composites had better dispersed nanoparticles, leading to more efficient conducting pathways than did the VAF composites, whose nanoparticles were more aggregated. Simultaneously, the presence of larger polyurethane domains resulted in a higher stretchability of the VAF composites (Fig. 2.2h–k and 2.13). The free-standing 1 × LBL and 1 × VAF had conductivities σ of 6,800 S cm^{-1} and 510 S cm^{-1} and maximum tensile strains ε_{max} of 16% and 75%, respectively. Lamination increased the conductivity of both types of film and considerably improved stretchability. The conductivities of the 5 × LBL and 5 × VAF composites were 11,000 S cm^{-1} and 1,800 S cm^{-1} for ε = 0% (Fig. 2.2b). Compared to the conductivities of other LBL films from gold nanoparticles stabilized by longer capping agents[88],

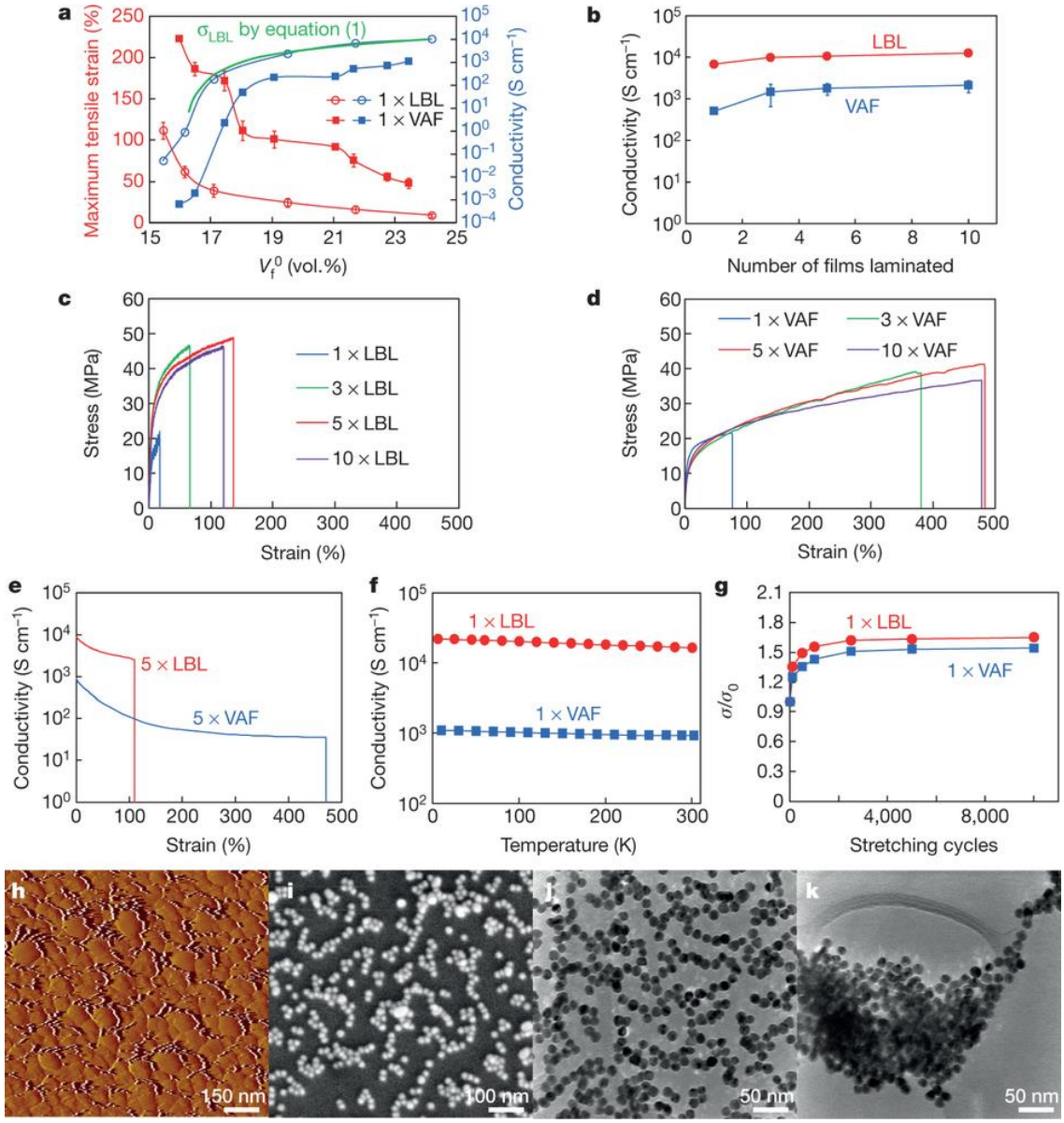

Figure 2.2. Mechanical and electrical properties of polyurethane–nanoparticle nanocomposites. **a**, Dependence of strain and conductivity of 1 × LBL and 1 × VAF on the volumetric gold content at ε = 0%. The green line shows the calculated conductivity of the LBL composite based on the power-law relation in Eq. 2.1 and three-dimensional percolation power law relation. **b**, Conductivity data of laminated films composed of 1, 3, 5 and 10 consolidated films for LBL and VAF. Error bars in **a** and **b** are mean ± s.d. (n = 3). **c**, **d**, Stress–strain curves for consolidated LBL (**c**) and VAF (**d**) stacks composed of 1, 3, 5 and 10 films, respectively. **e**, Conductivity as a function of uniaxial strain of 5 × LBL and 5 × VAF. **f**, Temperature dependence of conductivity for 1 × LBL and 1 × VAF. **g**, Change in conductivity (σ/σ_0) of 1 × LBL and 1 × VAF after recurrent stretching cycles, ε = 5%. **h**–**j**, Atomic-force-microscopy amplitude, SEM and TEM images of $(PU/NP)_2$, respectively. **k**, TEM image of a VAF nanocomposite.

those of our composites were more than 10^5 times better (see Fig. 1.2 and Table 1.1 for details).

The ε_{max} values for 5 × LBL and 5 × VAF were 115% and 486%, respectively (Fig. 2.2c and d). The conductivity of 5 × LBL and the stretchability of 5 × VAF are, to the best of our knowledge, the highest for previously studied composites.

2.3 Self-Organized Nanoparticles for Conducting Pathways

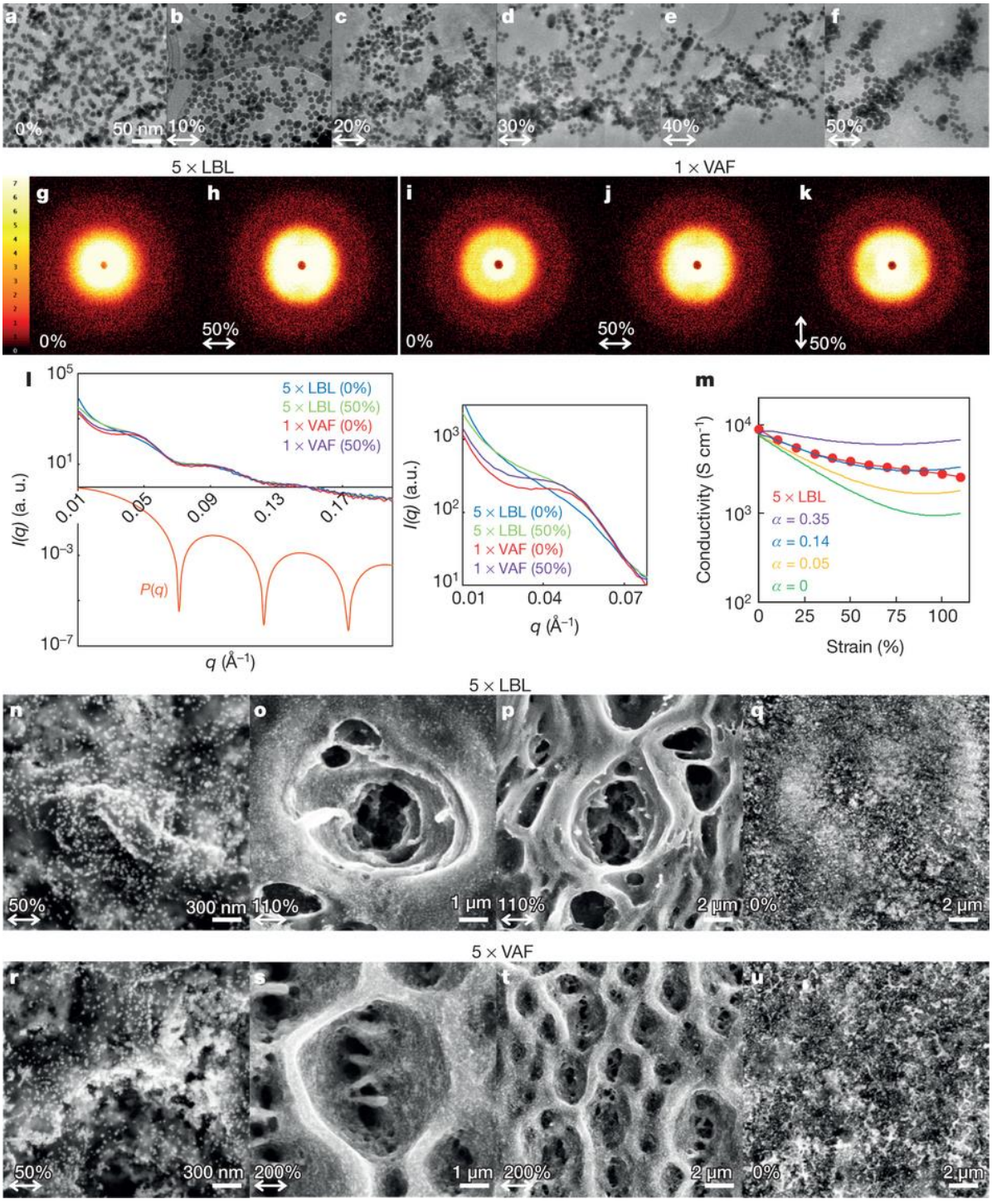

Figure 2.3. Reorganization of nanoparticles under stress.

a–f, TEM images of $(PU/PAA)_2(PU/NP)_4(PU/PAA)_1$ under strains of 0%, 10%, 20%, 30%, 40% and 50%, respectively, where PAA is polyacrylic acid. **g–k**, SAXS beam images of 5 × LBL and 1 × VAF at various strains. **l**, SAXS diffraction curves for films at different strains. $P(q)$ is form factor from the size and shape of nanoparticles. The diffraction curve segments around the peak at $q = 0.045$ Å^{-1} are given in the inset. **m**, Calculated conductivity dependence on strain for LBL composites described by percolation theory for self-assembling systems (Eq. 2.12 and 2.13) with various self-assembly coefficients α in comparison with actual data for 5 × LBL. **n–u**, SEM images of focused-ion-beam milled 5 × LBL and 5 × VAF at various strains. The images in q and u were taken after five consecutive stretches to 110% and 200%, respectively. Milling depths for samples in this study are 1 μm for 5 × LBL and 2 μm for 5 × VAF. Stretching directions are indicated by the double arrows.

As expected, the conductivity of LBL and VAF composites decreased with the increase of strain ε (Fig. 2.2e). ε = 60% resulted in a reduction of conductivity to 3,500 S cm^{-1} for 5 × LBL and a reduction to 210 S cm^{-1} for 5 × VAF. ε = 110% resulted in a reduction to 2,400 S cm^{-1} for 5 × LBL and a reduction to 94 S cm^{-1} for 5 × VAF. However, the conductivity values for high strain were slightly or considerably higher than similar values for carbon-nanotube-based materials[53,79], despite the much smaller aspect ratio of the nanoparticles. Moreover, no other composites have displayed σ = 35 S cm^{-1} at ε = 480%, as 5 × VAF does.

It is thus essential to understand how these composites retain the capability to transport electrons efficiently at very high deformations. From the outset we knew that nanoparticles are capable of self-assembling in solution into chains[91]. Atomic force microscopy, SEM and transmission electron microscopy (TEM) images indicated that nanoparticles in the LBL composites produced chains of 20–40 nanoparticles while they were being deposited (Fig. 2.2h–j). Such chains can behave similarly to high-aspect-ratio nanocomponents, reducing V_c (ref. [92]) while displaying a high conductance similar to that of bulk gold. This ability to self-assemble at the time of LBL deposition was initially hypothesized to be the cause of such an unusual combination of properties. We, however, could not find evidence for nanoparticle-

chain formation in the bulk from small-angle X-ray scattering (SAXS) data immediately after deposition at 0% strain (Fig. 2.3g, i, and l) or by using high-voltage electron microscopy (Fig. 2.14) for the LBL and VAF composites. We next considered the possibility that although they may be almost fully disorganized initially, the nanoparticles can self-organize under stress. Some elements of self-organization have been seen for low filler concentrations and high-aspect-ratio nanomaterials[47,93,94].

Indeed, we found clear evidence of stress-induced nanoparticle organization in both LBL and VAF composites from TEM images, SAXS data and SEM images (Fig. 2.3). First of all, TEM images of ultrathin (130 nm) LBL films under tensile strain showed a high mobility of the nanoparticles in the polymer matrix. As the strain increased, the nanoparticles gradually re-organized into bands along the stretching direction (Fig. 2.3a–f). In the SAXS data the well-developed hourglass-shaped scattering patterns were observed at higher elongations of ε = 50% for both composites, confirming that nanoparticles were organized in elongated structures (Fig. 2.3h, j, and k). The intensity of the diffraction peak at scattering vector q = 0.045 $Å^{-1}$ also substantially increased at ε = 50% for both composites (Fig. 2.3l).

Unlike other stress-induced composite reorganization, the beam patterns and intensity plots of SAXS data that developed upon stretching disappeared when the tension was released. The self-assembled nanoparticle patterns observed here were remarkably different from other patterns observed in both solutions and solids[91,93,94]. To reveal the nanoparticle patterns in the bulk of the composites, focused-ion-beam milling was applied to a depth of 1–2 μm. SEM images of such samples remaining under ε = 110% for 5 × LBL and ε = 200% for 5 × VAF revealed three-dimensional cellular self-organized patterns with characteristic dimensions of 1–

5 μm (Fig. 2.3o, p, s and t). These distinct nanoparticle networks can be the result of local phase separation of the nanoparticles in the polymer under high strain.

Importantly, when the tension was released, these cellular networks were not observed even after five consecutive stretches, indicating that the nanoparticle networks were reconfigurable (Fig. 2.3q and u). However, slight irreversible reconstruction of the material did occur on the surface, leading to formation of bands of nanoparticles running perpendicularly to the stress direction and decreased stiffness (Fig. 2.15). With ε = 5% (the elastic limit of both composites is considered to be less than ε = 10%), the films were repetitively stretched to observe changes in conductivity with deformation cycling. Interestingly, conductivity after 5,000 cycles increased substantially by 1.7-fold for 1 × LBL and 1.5-fold for 1 × VAF (Fig. 2.2g). The resistance of 1 × LBL and 1 × VAF films after 10,000 stretch cycles, measured parallel and perpendicular to the stretching direction, also confirmed the gradual internal rearrangement of the nanoparticles, which are completely isotropic without stress. Resistance in both directions decreased but decreased slightly more in the parallel direction than in the perpendicular direction. SAXS data for 1 × LBL and 1 × VAF films after 10,000 stretch cycles also confirmed the reorganization of nanoparticles (Fig. 2.16).

2.4 A Study of Conductivity by Percolation Theory

The prepared composites presented an interesting case for percolation theory because of (1) the unusually high conductance of particles with minimal aspect ratio and (2) the extensive structural characterization (Figs 2.2, 2.3). We note that there are no examples of applications of percolation theory to self-organized systems. The classical power law relates the conductivity of an unstretched material σ to V_f as follows:

$$\sigma(V_f^0) = \sigma_0\left(V_f^0 - V_c^0\right)^s \qquad \text{(Eq. 2.1)}$$

where σ_0 is the scaling factor, the conductivity of the filler, V_f^0, and V_c^0 are the volumetric fractions of the filler and percolation threshold at ε=0%, respectively, and s is the critical exponent. Calculated conductivity is roughly proportional to the fraction of nanoparticles as we experimentally observed (Fig 2.2a). Unambiguous application of Eq. 2.1 to VAF composites is difficult owing to aggregation of nanoparticles (Fig. 2.2k).

2.4.1 Theoretical Conductivity as a Function of Filler Volume Fraction

In order to describe the behavior of our nanoparticle composites in terms of the power-law of percolation theory (Eq. 2.1), the critical exponents, s, corresponding to both materials were determined to be s_{LBL}=1.50 and s_{VAF}=1.17 from the slopes of dependencies in Fig. 2.4a and b, respectively. The application of the classical percolation theory to VAF composite system is impeded by the fundamental assumption of individual filler particles to be homogeneously dispersed in the matrix which Eq. 2.1 is based on. Despite the successful linearization in the *log-log* plot in Fig. 2.4b, further application of the theory is impeded by

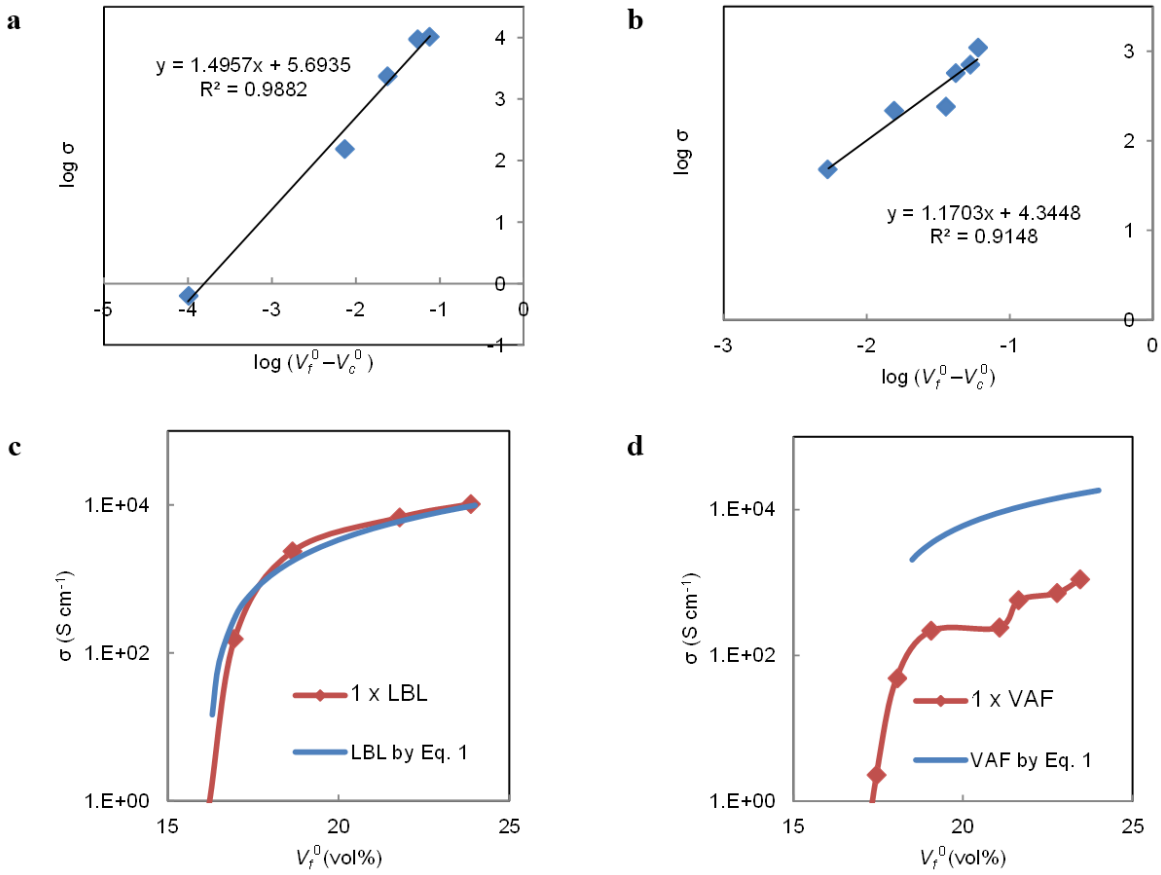

Figure 2.4. Experimental dependence of σ on V_f and its linearization according to the classical power-law relation of 3D percolation theory. a, **b**, Log plots of σ in respect to $\log(V_f^0 - V_c^0)$ with a linear fit as described as Eq. 2.1 for 1 x LBL and 1 x VAF, respectively. **c**, **d**, Comparison of calculated conductivities and actual data of 1 x LBL and 1 x VAF for unstrained composites, respectively.

significant agglomeration of gold particles clearly visible in Fig. 2.2k that result in the distinct mismatch of experimental and predicted values in Fig. 2.4d[95]. Indeed, σ_{LBL} calculated showed excellent agreement with $\sigma_{1 \times LBL}$ in the absence of strain at various volume fraction of fillers (Fig. 2.4c).

2.4.2 Theoretical Conductivity as a Function of Engineering Strain

Conductivity of Au NP filled LBL composites with fixed volume fraction of nanoparticles can be simulated as a function of engineering strain using the 3D power law relation[79,96]. Due to the fundamental restriction of the equation that NPs are homogeneously distributed in the matrix, we restricted consideration of percolation theory to LBL composites, which represent an almost ideal case for this theory owing to the nearly uniform distribution of nanoparticles. V_f was converted as a function of engineering strain using relations below and σ_0, V_c and s were considered as constant upon stretching. Composite volume change was reflected by Poisson's ratio which were experimentally obtained using a high speed camera. Values were obtained by calculating the difference between initial stretching and final rupture (See section 2.4.3 for comparison of calculated conductivity values using constant and strain-specific Poisson's ratio). The material was anisotropic and Poisson's ratios thickness- and width- wise were $\nu_{LBL,\ \text{thickness}} = 0.26$, $\nu_{LBL,\ width} = 0.14$.

$$\nu_w(\varepsilon) = -\frac{(w_2 - w_1)/w_1}{(L_2 - L_1)/L_1} = \frac{w_1 - w_2}{w_1 \cdot \varepsilon} \qquad \text{(Eq. 2.2)}$$

$$\nu_t(\varepsilon) = -\frac{(t_2 - t_1)/t_1}{(L_2 - L_1)/L_1} = \frac{t_1 - t_2}{t_1 \cdot \varepsilon} \qquad \text{(Eq. 2.3)}$$

Volume of composites under stretching can be expressed using following equations:

$$V_f = \frac{V_{gold}}{V_2} \qquad \text{(Eq. 2.4)}$$

$$V_2 = L_2 \cdot w_2 \cdot t_2 \qquad \text{(Eq. 2.5)}$$

Length, width and thickness of composite under stretching can be obtained using following relations:

$$L_2(\varepsilon) = L_1 \cdot (\varepsilon + 1) \qquad \text{(Eq. 2.6)}$$

$$w_2(\varepsilon) = w_1 \cdot (1 - \nu_w \cdot \varepsilon) \qquad \text{(Eq. 2.7)}$$

$$t_2(\varepsilon) = t_1 \cdot (1 - \nu_t \cdot \varepsilon) \qquad \text{(Eq. 2.8)}$$

Eq. 2.7 and 2.8 were obtained from rearrangement of Eq. 2.2 and 2.3, respectively. Thus, volume of stretched composite as a function of strain can be

$V_2(\varepsilon) = L_2(\varepsilon) \cdot w_2(\varepsilon) \cdot t_2(\varepsilon) = L_1 \cdot w_1 \cdot t_1(\nu_t \cdot \nu_w \cdot \varepsilon^3 + (\nu_t \cdot \nu_w - \nu_t - \nu_w)\varepsilon^2 - (\nu_t + \nu_w - 1)\varepsilon + 1)$ (Eq. 2.9)

Therefore, volume fraction of gold in the composite under stretching and calculated conductivity as a function of strain will be obtained as follows:

$$V_f(\varepsilon) = \frac{V_{gold}}{V_2(\varepsilon)} \qquad \text{(Eq. 2.10)}$$

$$\sigma(\varepsilon) = \sigma_0\big(V_f(\varepsilon) - V_c^0(\varepsilon)\big)^s \qquad \text{(Eq. 2.11)}$$

As strain increases, the calculated σ dropped faster than did the experimental data, despite the general tendency of the method to overestimate the conductance for large strains. This finding showed that the current percolation theory cannot explain the dynamic nature of conductive pathways under strain. The influence of stress-induced self-organization processes could be described as an apparent increase of the aspect ratio of the fillers (Fig. 2.3a-f), which reduced V_c and hence increased σ. Thus, V_c^0 in Eq. 2.11 was modified by introducing a self-assembly coefficient α with square-root dependency of ε as follows:

$$V_c(\varepsilon) = \frac{V_c^0}{1 + \alpha\sqrt{\varepsilon}} \qquad \text{(Eq. 2.12)}$$

Therefore, overall conductivity equation including effect of volume change and re-organization of NPs becomes as follows:

$$\sigma(\varepsilon) = \sigma_0 \left(\frac{V_{gold}}{L_1 \cdot w_1 \cdot t_1(\nu_t \cdot \nu_w \cdot \varepsilon^3 + (\nu_t \cdot \nu_w - \nu_t - \nu_w)\varepsilon^2 - (\nu_t + \nu_w - 1)\varepsilon + 1)} - \frac{V_c^0}{1 + \alpha\sqrt{\varepsilon}}\right)^s \qquad \text{(Eq. 2.13)}$$

When α = 0.14 the theoretical curve fitted the experimental data nearly perfectly (Fig. 2.3m). As the coefficient α increases the ability of particles to reorganize to form conductive pathways becomes more pronounced. The numerical value of α reflects the effects of both the ability of nanoparticles to form non-random associations in solids and their directionality.

2.4.3 Use of Constant Poisson's ratio

When calculating volume of composite under stretching, use of strain specific Poisson's ratio could make the calculation more precise, because Poisson's ratio could change under large strains. To check on this point, sample dimensions were measured at each 10% strain level and Poisson's ratio at each level was calculated (Fig. 2.5a, b). Dimensions of the sample at each strain level changed proportionally to tensile deformation and calculated Poisson's ratio at each strain level was nearly constant: averaged strain-specific Poisson's ratio were 0.26 ± 0.01 for thickness wise and 0.15 ± 0.01 for width wise (Fig. 2.5c).

The obtained Poisson's ratio values were further used to calculate theoretical conductivity at every 10% strain level using the above Eq. 2.11 combined with Eq. 2.12 (Fig. 2.6). Calculated conductivity dependence on strain with strain-specific Poisson's ratio had very close match to the one calculated using constant Poisson's ratio. Because dimension change of samples under tensile deformation were linear. Averaged Poisson's ratio with standard deviation were $\nu_{LBL,\ \text{thickness}}$ = 0.26 ± 0.01, $\nu_{LBL,\ width}$ = 0.15 ± 0.01 (Fig. 2.5c) while constant Poisson's ratio used for calculation in Fig. 2.6a were $\nu_{LBL,\ \text{thickness}}$ = 0.26, $\nu_{LBL,\ width}$ = 0.14.

a

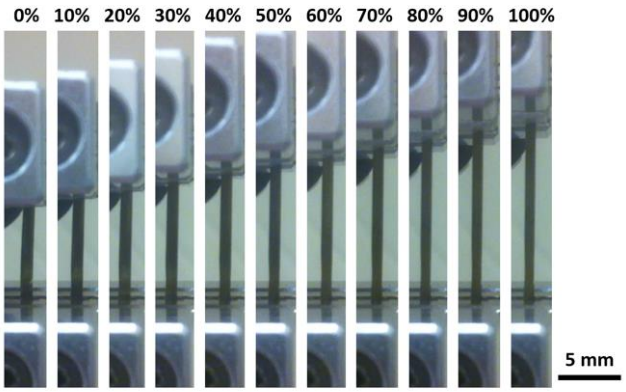

b

	0%	10%	20%	30%	40%	50%	60%	70%	80%	90%	100 %
Length (mm)	7.3	8.03	8.76	9.49	10.22	10.95	11.68	12.41	13.14	13.87	14.6
Width (mm)	1	0.985 5	0.971	0.951	0.939	0.921	0.902	0.89	0.883	0.872	0.861
Thickness (mm)	0.005 50	0.005 35	0.005 19	0.005 11	0.004 92	0.004 78	0.004 63	0.004 50	0.004 37	0.004 23	0.004 08

c

	0%	10%	20%	30%	40%	50%	60%	70%	80%	90%	100 %	Mean± S.D.
Width wise	n/a	0.14 5	0.14 5	0.16 3	0.15 3	0.15 8	0.16 3	0.15 7	0.14 6	0.14 2	0.13 9	0.151± 0.009
Thickness wise	n/a	0.27 3	0.28 2	0.23 6	0.26 4	0.26 2	0.26 4	0.26 0	0.25 7	0.25 7	0.25 8	0.261± 0.012

Figure 2.5. a, Photographic images of 5xLBL composite under stretching up to 100%. **b**, Dimensions of samples at each 10% strain level. **c**, Poisson's ratio of the sample width- and thickness- wise at each 10% strain level.

Use of strain-specific Poisson's ratio (even smaller strain levels such as every 5% could more precisely) could potentially give us better fitted calculated conductivity under strain. This will be especially true for samples where non-linear deformation properties are dominant. However, in our case, due to sample's linear deformation upon stress, the effect of introducing strain-specific Poisson's ratio was not significant. Therefore, application of constant Poisson's ratio is valid in this study.

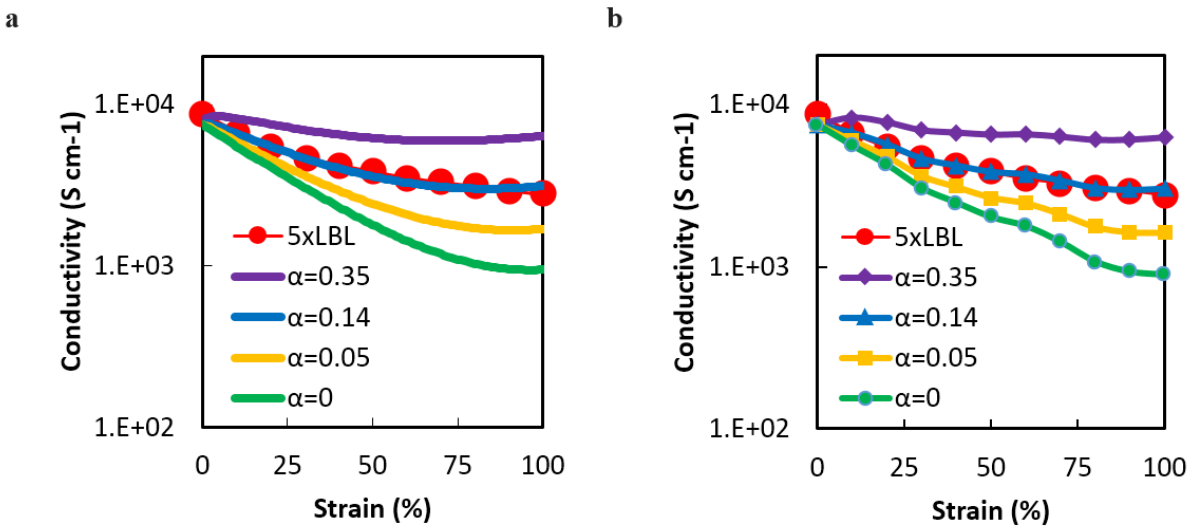

Figure 2.6. a, Calculated conductivity dependence on strain for LBL composites with constant Poisson's ratio in comparison with actual data for 5xLBL. **b**, Calculated conductivity dependence on strain for LBL composites with strain specific Poisson's ratio in comparison with actual data for 5xLBL.

2.4.4 Theoretical Conductivity as a Function of True Strain

Engineering strain is sometimes not appropriate to use for analysis when the strain level is high, often greater than 50%, where non-linear deformation is dominant. Although, the samples in this study underwent linear deformation, true strain method was applied to calculated simulated conductivity and the resulted is compared with the ones from using engineering strain.

Experimentally measured dimensions of length, width, and thickness under stretched state (data from Fig. 2.5) were used for calculation using the equation below:

$$\sigma(\varepsilon) = \sigma_0 \left(\frac{V_{gold}}{L_2 \cdot w_2 \cdot t_2} - V_c^0(\varepsilon) \right)^s \qquad \text{(Eq. 2.14)}$$

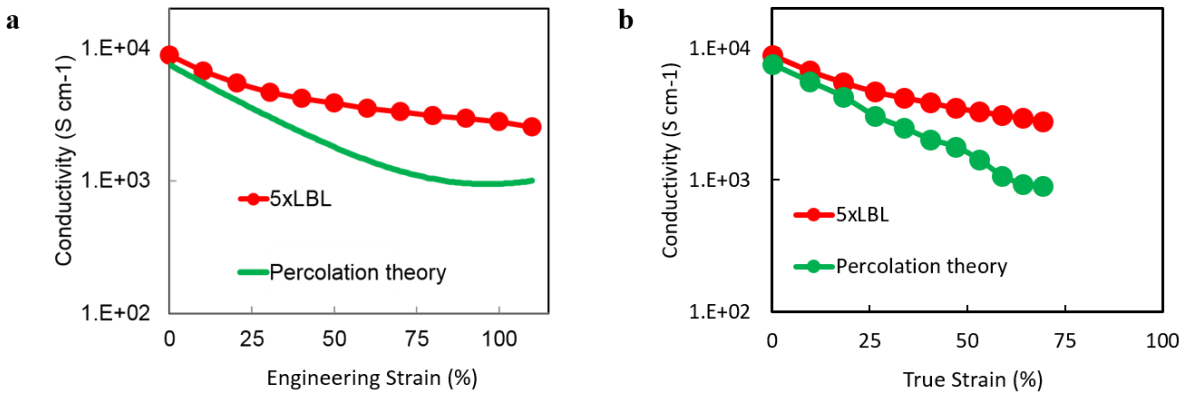

Figure 2.7. a, Calculated conductivity dependence on engineering strain for LBL composites using equation 2.13 with α=0 in comparison with actual data for 5xLBL. **b**, Calculated conductivity dependence on true strain for LBL composites using equation 2.14 in comparison with actual data for 5xLBL.

Natural log relation of strain made "maximum tensile true strain" to be shorter than the one using engineering strain. Except the difference in strain level, the results show that calculated conductivity values and patterns using either engineering strain or true strain were almost the same (Fig 2.7). This is presumably due to linearly deformed sample dimensions upon uniaxial tensile stretching.[1]

[1] In this study, strain values were expressed using engineering stain rather than true strain. Use of engineering strain to measure and evaluate strain-stress relations of materials, especially for stretchable conductors which mostly tensile deformed in uniaxial manner, is the most commonly used methods: literally, all published work of "stretchable conductor" studies used engineering strain rather than true strain. This is because researchers in this field are more interested in change of electrical properties of samples under applied strains (Refs. Chun et al.; Baik, S. Nature Nanotech. 5, 853–857 (2010), Lipomi et al.; Bao, Z. Nature Nanotech. 6, 788-792 (2011), Matsuhisa et al.; Someya, T. Nat. Commun. 6, 7461 (2015), Stoyanov et al.; Kofod, G. Adv. Mater. 25, 578-583 (2013), Sekitani et al.; Someya, T. Science 321, 1468-1472 (2008), Shim et al.; Kotov, N.A. ACS Nano, 3, 1711–1722 (2009)). Additionally, considering practicality of the topic and real applications in diverse industries, use of engineering strain will be more suitable for the researchers in each different field to communicate better. However, we would like to make a note that further analyses using true strain could be one of interesting future research directions from a view point of solid mechanics. (Refs. Hencky, H. "Über die Form des Elastizitätsgesetzes bei ideal elastischen Stoffen". Zeitschrift für technische Physik. 9, 215–220. (1928). Rees, David "Basic Engineering Plasticity: An Introduction with Engineering and Manufacturing Applications." Butterworth-Heinemann. ISBN 0-7506-8025-3 (2006).)

2.5 Charge Transport Mechanism

An understanding of charge transport in these materials is academically and practically

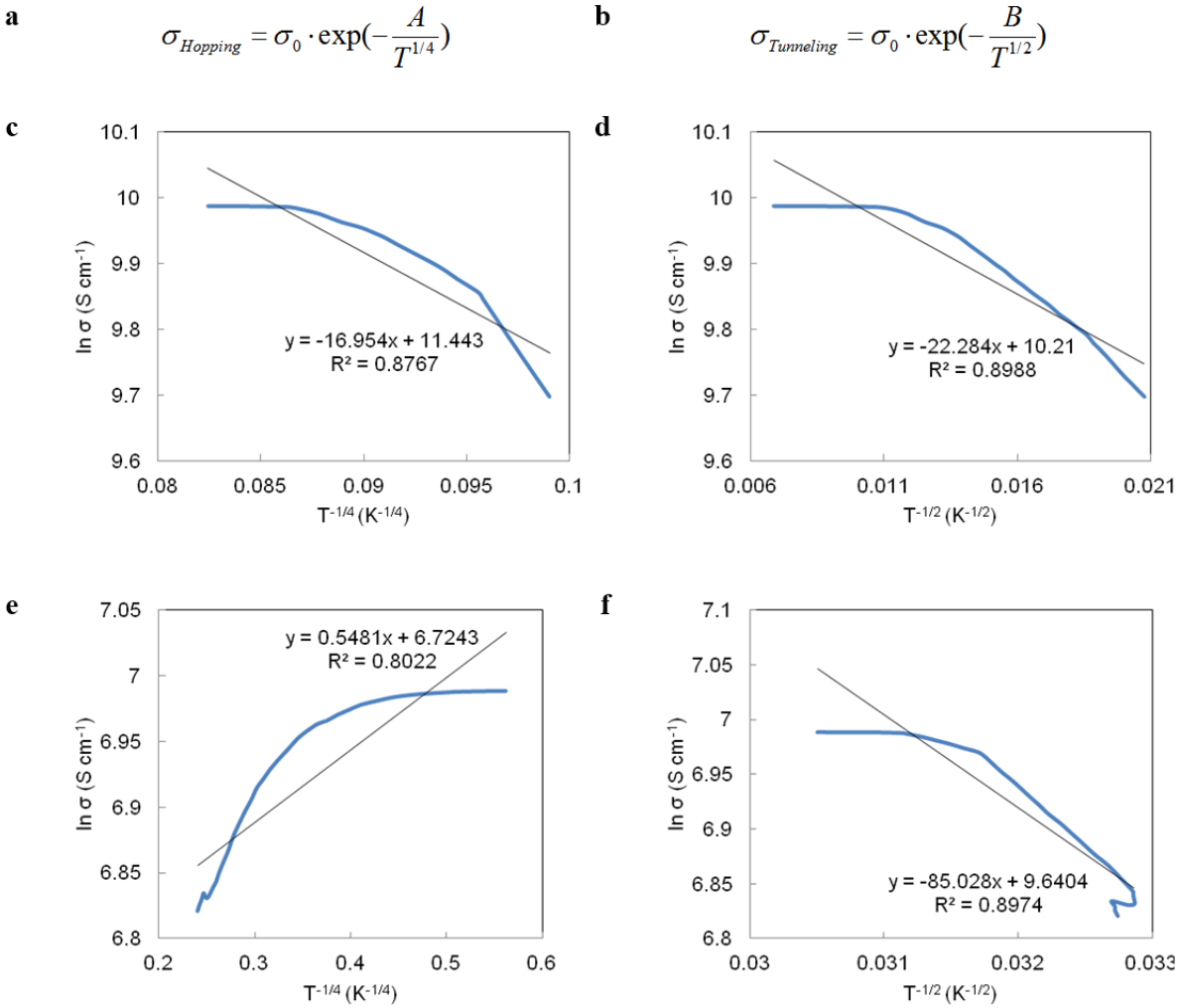

Figure 2.8. Charge transport in polyurethane-nanoparticle nanocomposites. a, b, Equations for variable-range hopping and tunneling mechanisms, respectively. **c, d,** Plots of *ln* σ *vs* $T^{-1/4}$ and $T^{-1/2}$ from data points of 1 x LBL film (Fig. 2.2f), respectively. **e, f,** Plots of *ln* σ *vs* $T^{-1/4}$ and $T^{-1/2}$ from data points of 1 x VAF film (Fig. 2.2f), respectively.

essential. Three different conduction mechanisms are possible between neighboring gold nanoparticles: (a) direct contact; (b) variable-range hopping and (c) tunneling. The relative contribution of hopping and tunneling mechanisms depends on the shape of the barrier, the separation of the sites and thermal energy[97,98,99]. Dependence of conductivity on temperature

provides a reliable criterion by which conduction mechanism that dominates the samples can be unveiled. Fitting the equations for variable-range hopping and tunneling conduction mechanism demonstrate that electron transfer mechanism in LBL and VAF stretchable conductors is governed neither by hopping nor by tunneling: plots of $ln\ \sigma$ *vs* $T^{-1/4}$ and $T^{-1/2}$ drawn from data points from Fig. 2.2f with equations in Fig. 2.8a and 2.8b did not conform to expected linear dependence.

Fitting the temperature dependence of conductivity from 2 to 300 K with variable-range charge transport equations revealed clear metallic behavior via direct nanoparticle contact (Fig. 2.2), whereas the temperature dependence of conductivity from 2 to 300 K in the stretchable conductors from carbon nanotubes showed semiconducting behavior and hopping electron transport[81]. Importantly, gold nanoparticle composites had high electron mobilities of $1.75 \times 10^{-4}\ m^2\ V^{-1}\ s^{-1}$ for $1 \times$ LBL and $5.45 \times 10^{-5}\ m^2\ V^{-1}\ s^{-1}$ for $1 \times$ VAF, and the carrier concentration of $5.83 \times 10^{28}\ m^{-3}$ for $1 \times$ LBL at 300 K approached very closely to that for bulk gold, $5.90 \times 10^{28}\ m^{-3}$ (Fig. 2.17).

2.6 Additional Practical Aspect: Damping of Vibration

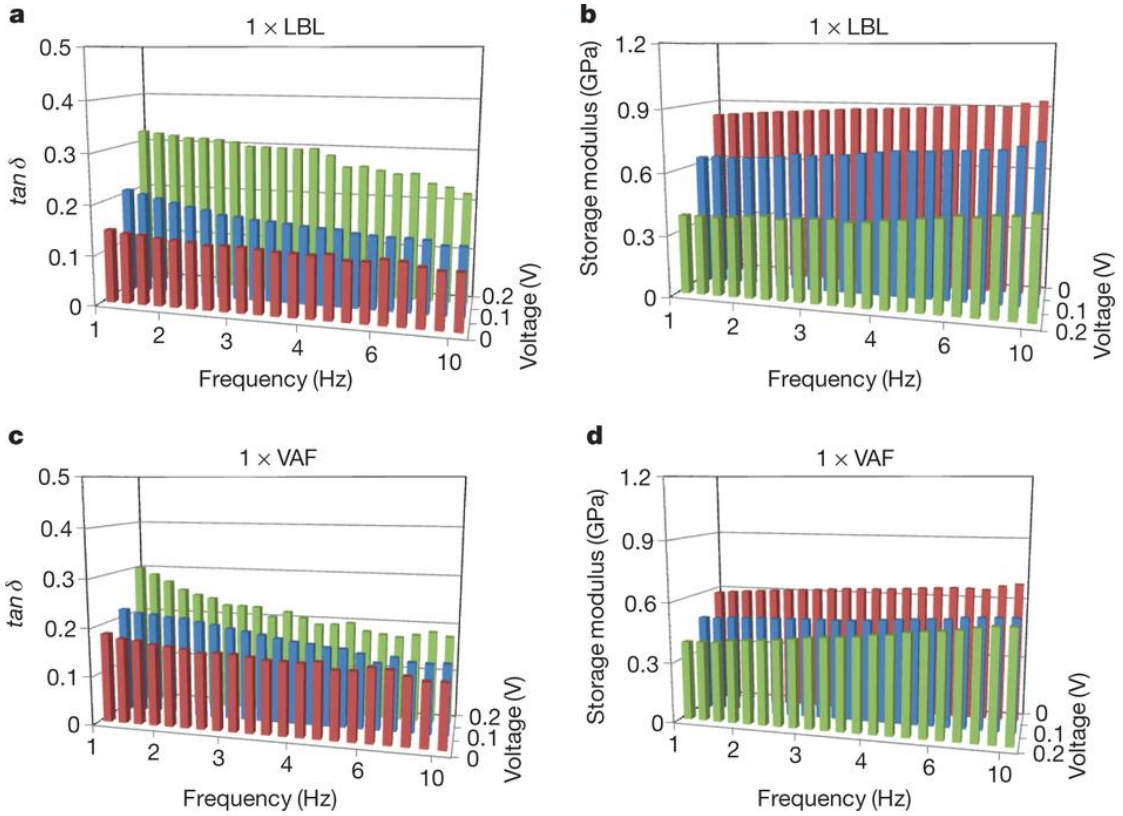

Figure 2.9. Viscoelastic properties of polyurethane–nanoparticle nanocomposites for different applied voltages. **a**, **b**, Damping parameter tanδ and storage modulus for 1 × LBL, respectively. **c**, **d**, Damping parameter tanδ and storage modulus of 1 × VAF, respectively.

As one of many possible demonstrations of the practical relevance of the new composites, we performed a dynamic mechanical analysis under small voltage to illustrate the electro-tunability of their viscoelastic properties. The relaxation of composites at a frequency of 1–10 Hz significantly increased when a small voltage of 0.2 V was applied, owing to repulsive transient charges on nanoparticles. As such, the damping parameter tanδ increased by 2.2-fold and 1.6-fold and the storage modulus decreased by 2.1-fold and 1.5-fold for 1 × LBL

and 1 × VAF, respectively (Fig. 2.9 and 2.19). Solid materials with electro-tunable mechanical properties are more practically viable than metallic structures filled with liquid electrolytes[100].

2.7 Conclusion and Outlook

From a fundamental perspective, these composites with high gold-nanoparticle loading displayed a previously unknown reorganization into cellular networks under stress. To some degree such restructuring imitates the behavior of atoms in liquid metals, while retaining structural integrity and strong bonding. The nanoparticle dynamics in such composites can be described by a variation of classical percolation theory and can be extended to a variety of other nanoparticle–polymer systems. Further improvements can be achieved by the development of commercially affordable conducting fillers and new polyelectrolytes to optimize properties. Further fabrication of such composites could aim to meet the demands of applications in medicine, optoelectronics, and energy storage devices that require electro-tunable properties.

2.8 Materials and Methods

Unless otherwise specified, LBL and VAF films had same gold contents in all the tests. The described measurements were performed under room temperature and relative humidity of 20-30% for both LBL and VAF composites.

Synthesis of Au NPs. To ultrapure DI water (950 mL) in a 1 L glass beaker equipped with a magnetic stir bar was added Gold(III) chloride trihydrate (180.0 mg, 0.458 mmol). Gold(III) chloride trihydrate, sodium citrate tribasic dihydrate (Sigma-Aldrich) were used as-

received. The mixture was heated to boil under vigorous stirring followed by additional heating for 20 min. Subsequently, 50 mL of 34 mM sodium citrate solution was added to the mixture. The aqueous solution was heated for 20 min followed by cooling to room temperature. Citrate stabilized Au NPs with diameter 13 ± 0.3 nm were synthesized. As-prepared aqueous solution was directly used for the preparation of VAF films. In some cases, it was further concentrated to be used as dipping solution for LBL films. For the concentration process, the as-made aqueous Au NPs dispersions were transferred into 50 mL centrifuge tubes and concentration of the solutions increased via Sorvall Legend Mach 1.6R (Thermo scientific, MA, USA) at the speed of 10,000 rpm for 1 hr. Less than 5 mL of concentrated of Au NPs solution was settled at the bottom of the tube. Supernatant of 45 mL were removed by suction pipettes, while taking special care to prevent disturbing of the sedimented nanoparticles. Finally, the resultant NPs were collected to be used for LBL process.

Preparation of LBL films. For LBL assembly, substrates were sequentially dipped into a diluted solution of PU and a dispersion of concentrated Au NPs with each step followed by rinsing with DI water and drying with compressed air. As-received cationic polyurethane aqueous dispersion (30 vol%, MW ≈ 92,000, Hepce Chem Co., South Korea) was used after diluting to 1 vol% solutions in deionized (DI) water. This deposition cycle constitutes a pair of layers, and can be repeated n times as necessary to obtain desirable thickness. The resulting film will be denoted as $(PU/NP)_n$. Desirable gold contents in the composites were acquired by controlling the dipping time of a substrate to the dispersion of Au NPs.

Glass slides (25 mm x 75 mm, Fisher Scientific) cleaned by piranha solution (Sulfuric acid:hydrogen peroxide, from Sigma-Aldrich, in a 3:1 volume ratio.) overnight were dipped

into a 1 vol% solution of PU, for 5 min, rinsed with DI water for 1 min and gently dried with compressed air. Note that the piranha solution is dangerous and extremely reactive with organic substances so appropriate handling precautions must be ensured at all times. Then they were dipped into a dispersion of concentrated Au NPs, for several minutes, rinsed 1 minute, and again dried with compressed air. After having desired thickness, free-standing films were isolated by etching of the glass slides with 1 vol% HF (Sigma-Aldrich) solution. Note that HF solution even diluted is very toxic so extreme precautions must be taken at all times. After through rinsing with water, the detached films were dried in an oven at 60 ºC overnight and then kept in ambient conditions (room temperature and relative humidity of 20-30%) for another overnight prior to measurement of properties. Conditions and procedures for preparation of LBL films with various Au contents were same except dipping time to the dispersion of concentrated Au NPs. LBL films containing 15.4 vol%, 16.2 vol%, 16.9 vol%, 19.4 vol%, 21.7 vol%, 24.0 vol% of Au NPs were prepared with dipping times of 1 min, 2 min, 3 min, 8 min, 14 min, and 20 min, respectively. When substrate is dipped into the Au NPs dispersion, tiny amounts of PUs, which might be weakly bonded, are slowly diffused into dispersion of Au NPs. In the process of cyclic deposition, PUs are accumulated in the dispersion of Au NPs and when that over the specific threshold, Au NPs are flocculated. To keep the homogeneity of LBL film, careful monitoring of flocculation is needed. If it is observed, the dispersion of Au NPs needs to be changed. LBL thin film of $(PU/PAA)_2(PU/NP)_4(PU/PAA)_1$ was prepared for TEM experiments. Detail methods for films preparation here were exactly same as above typical process. Dipping time of glass slide into PAA was 5 min.

Preparation of VAF films. For VAF film preparation, mixture and stirring of a dispersion of as-prepared Au NPs and a diluted solution of PU followed by filtration were done. Desirable gold contents in the composites were achieved by controlling the volume of a dispersion of as-prepared Au NPs solutions.

To a 1 L glass beaker containing 1 L of as-prepared Au NPs dispersion (no additional concentration steps were applied) equipped with a magnetic stir bar was slowly added 1 mL of 1.0 vol% aqueous PU. The mixture was kept stirring for 15 min followed by filtration. Filter papers of 0.8 μm pore size with 47 mm diameter, and filtration assembly were obtained from Fisher Scientific. The resultant gold-colored film was peeled off from the filter paper. It is recommended to dry the film completely before taking it out from the filtration assembly. Individual films peeled off has some fibrous material that came from the filter paper, thus removal of those materials is needed by gentle scratching. Conditions and procedures for preparation of VAF films with various Au contents were same except volumetric ratio of a dispersion of as-prepared Au NPs solutions. VAF films containing 15.9 vol%, 16.4 vol%, 17.3 vol%, 18.0 vol%, 19.1 vol%, 21.0 vol%, 21.7 vol%, 22.8 vol%, and 23.4 vol% of Au NPs were prepared with 250 mL, 500 mL, 650 mL, 700 mL, 800 mL, 900 mL, 1,000 mL, 1,050 mL, and 1,100 mL of as-prepared Au NPs dispersion, respectively. To make a 30 μm thick VAF film, total ca. 1,800 mL solution needs to be filtered.

Characterizations. Initial stages of LBL deposition were monitored using an 8453 UV-vis Chem Station spectrophotometer (Agilent Technologies, CA, USA). Thickness of initial assembly of LBL film was calculated using a BASE-160 Spectroscopic Ellipsometers (J. A. Woollam Co., Inc., NE, USA). Calculations were fitted using a Cauchy's model. The

LBL film for ellipsometry was prepared on silicon wafers following the same procedure previously described as LBL film.

Stress-strain curves were obtained by testing ~1 mm wide and 5-7 mm long rectangular strips of samples with a mechanical strength tester 100Q (TestResources Inc., MN, USA). Tests were performed at a rate of 0.01 mm/s for LBL films and 0.08 mm/s for VAF films with a ~111 N range load cell. Five samples were tested for each film. The force measurements from the load cell were divided by the measured initial thickness and initial width of the sample gauge section to give nominal stress. This procedure results in a plot of nominal stress versus nominal strain. The cyclic tensile test (Fig. 2.2g) was performed by a Servopneumatic Axial/Torsion Test Instrument with custom made grips (EnduraTEC, MN, USA). Tests were performed at a rate of 0.01 mm/s.

Conductivity measurements with two-probe and four-probe methods were obtained using an 34401A Digital Multimeter, 6 ½ Digit (Agilent Technologies, Inc., CA, USA). Measurements of conductivity as a function of strain (Fig. 2.2e) were done in a custom four-probe set up depicted in Fig. 2.18. Measured resistance and applied tensile strain were recorded simultaneously by a video camera, and close up images of sample were photographed by a high speed camera to calculate the thickness of sample at some strain level with the assumption that volume of sample was kept constant. The temperature dependence of conductivity was measured by four probe method using a Magnetic Property Measurement System (MPMS) (Quantum Design, Inc., CA, USA). The MPMS is basically a cryogenic probe which integrates a superconducting magnet with a SQUID detection system and a

temperature controller in a specially designed Dewar. These sophisticated configurations provide rapid precision measurements over a temperature range from 2 to 300 K.

Filler fraction of sample was determined by a Pyris 1 TGA (PerkinElmer, MA, USA) with a temperature ramp from 25 °C to 800 °C at 10 °C/min under an air atmosphere at a flow rate of 20 mL/min. The Differential Scanning Calorimetry analysis was performed using a Q200 (TA Instruments, DE, USA). Scanning electron microscopy (SEM) images were obtained with an FEI Nova Nanolab dual-beam FIB and scanning electron microscope. TEM images were obtained with a JEOL 2010F Analytical Electron Microscope. HVEM images were obtained with the high voltage electron microscope (1,250 kV, JEOL, JEM-ARM 1300S). AFM imaging was performed with a Nanoscope III atomic force microscope (Digital Instruments/Veeco Metrology Group). X-ray scattering data were obtained with a Bruker NanoStar Small-Angle X-ray Scattering System equipped with Siemens Kristalloflex 770 X-Ray Generator, and Cu Kα Radiation (0.1542 nm) X-ray tube with Peak power of 1.5 kW on a Hi Star Area 2D detector with 1 min of exposure time. Damping parameter tanδ and storage modulus of the samples were obtained with an RSA 3 dynamic mechanical analyzer (TA instruments) with applied ε=0.5 % within the frequency range of 1-90 Hz. Load cell with a maximum capacity of 3.5 N and a resolution of 1 μN was used.

2.9 Supplementary Information

2.9.1 Particle Deposition

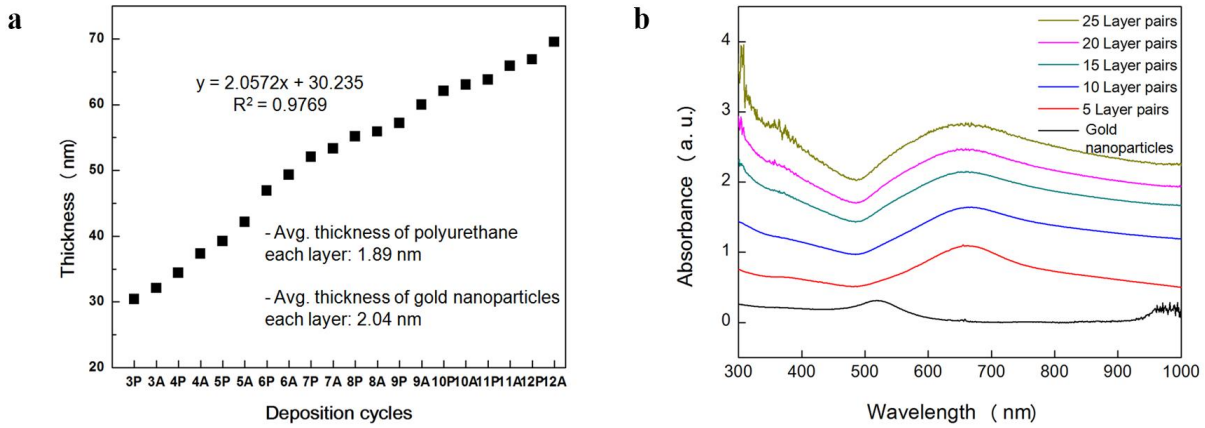

Figure 2.10. a, Dependence of thickness of the $(PU/NP)_n$ film on the number of the deposition cycles. Polyurethane (3P, 4P, 5P…) and gold nanoparticles (3A, 4A, 5A…) layers with the same number correspond to one deposition cycle. Thickness change was measured by ellipsometry as the LBL film was deposited on a silicon wafer. Thickness of each layer was averaged on the basis of three independent measurements. Average thickness increments for polyurethane and gold nanoparticles layers are 1.89 nm and 2.04 nm, respectively. **b**, UV-Vis absorbance spectra measured every 5^{th} layer pairs of LBL assemblies. The multilayers were formed on both sides of a glass substrate.

The shift of the plasmon peak from 515 nm (free gold nanoparticles) to 650-660 nm for LBL films is indicative of strong plasmonic coupling and nanoparticles proximity to each other, which is beneficial for efficient charge transport between nanoparticles.

2.9.2 Thermal Responses

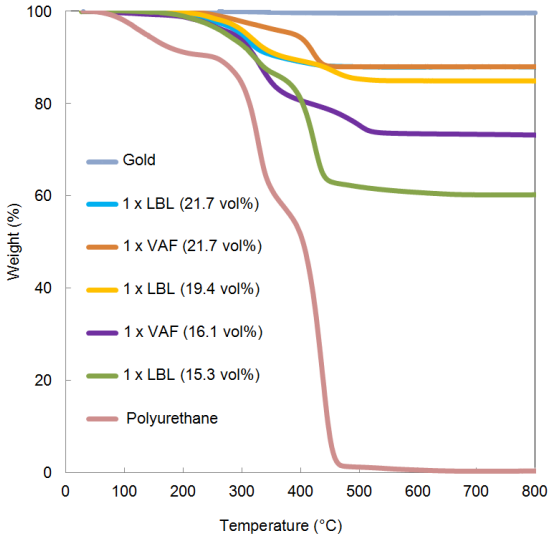

Figure 2.11. Thermal gravimetric analysis (TGA) of pure gold, pure polyurethane, and single free-standing, 1x, LBL and VAF films with different gold contents. The vol% given in parentheses refers to V_f of gold in each film and 21.7 vol% is equal to 87.7 wt%.

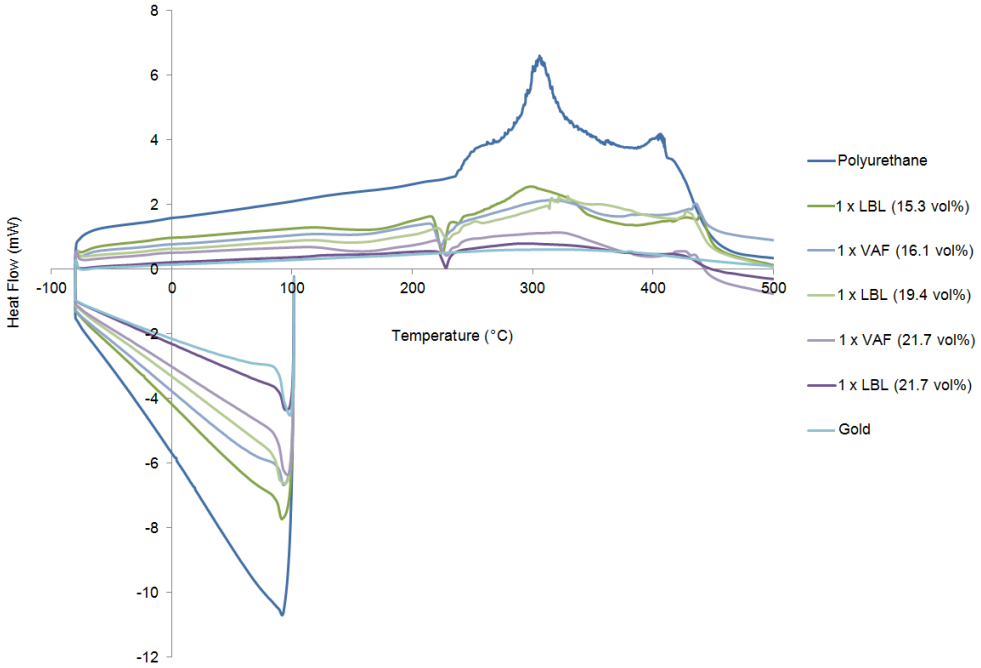

Figure 2.12. Differential scanning calorimetry (DSC) for pure polyurethane, LBL films, VAF films, and pure gold. Nanoparticle contents of composites are given in parentheses and refer to V_f of gold in each film.

2.9.3 Percolated Networks

Theoretical values of V_c volume fractions, which reflected site percolation probability and filling factor together, for nanoparticles composite assuming that (a) one nanoparticle takes place one lattice spot and (b) a cluster is connected only with nearest neighbors, for simple cubic lattice, body-centered cubic lattice, and face-centered cubic lattice are 0.162, 0.163, and 0.144, respectively[101,102].

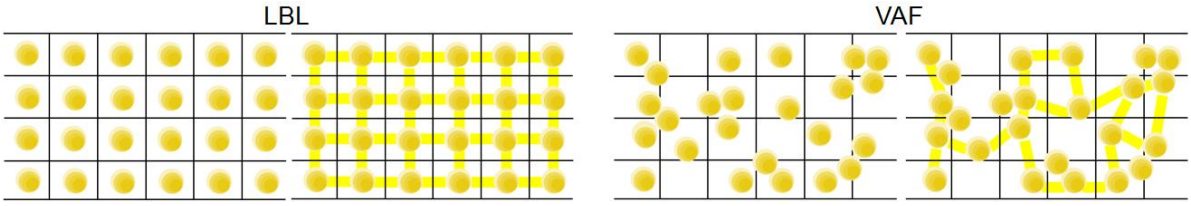

Figure 2.13. Idealized schematics of well-dispersed nanoparticles in LBL and VAF composites with distributed random aggregates (number of particles is same for both cases and spaces are filled with polymers in the lattice) in a 2D cross-sectional grid array with percolation pathways to nearest neighbors of nanoparticles.

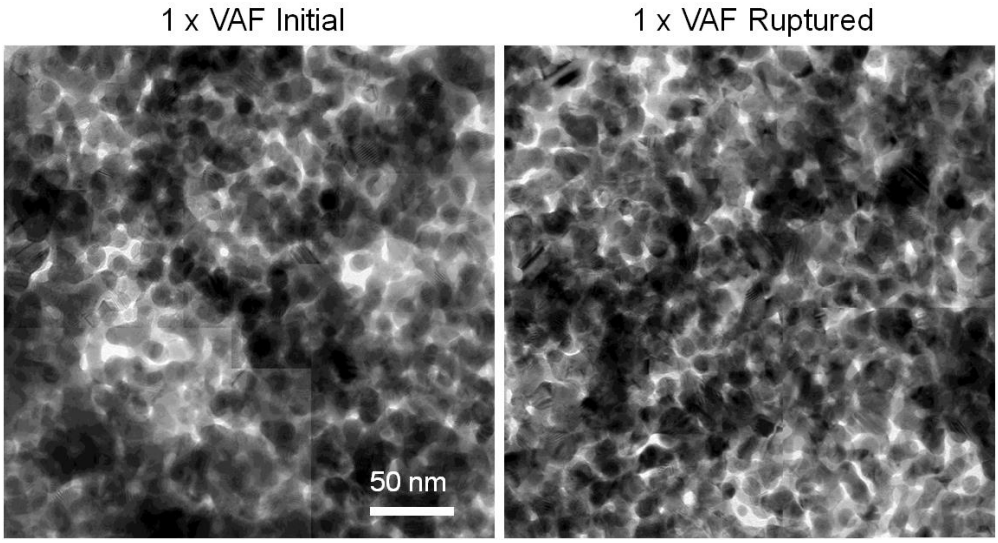

Figure 2.14. High-voltage electron microscopy (HVEM) images of 1 x VAF. Imaging was performed on the ruptured point. The specimens were prepared by using FIB.

2.9.4 Mechanical and Electrical Properties after Repetitive Stretching

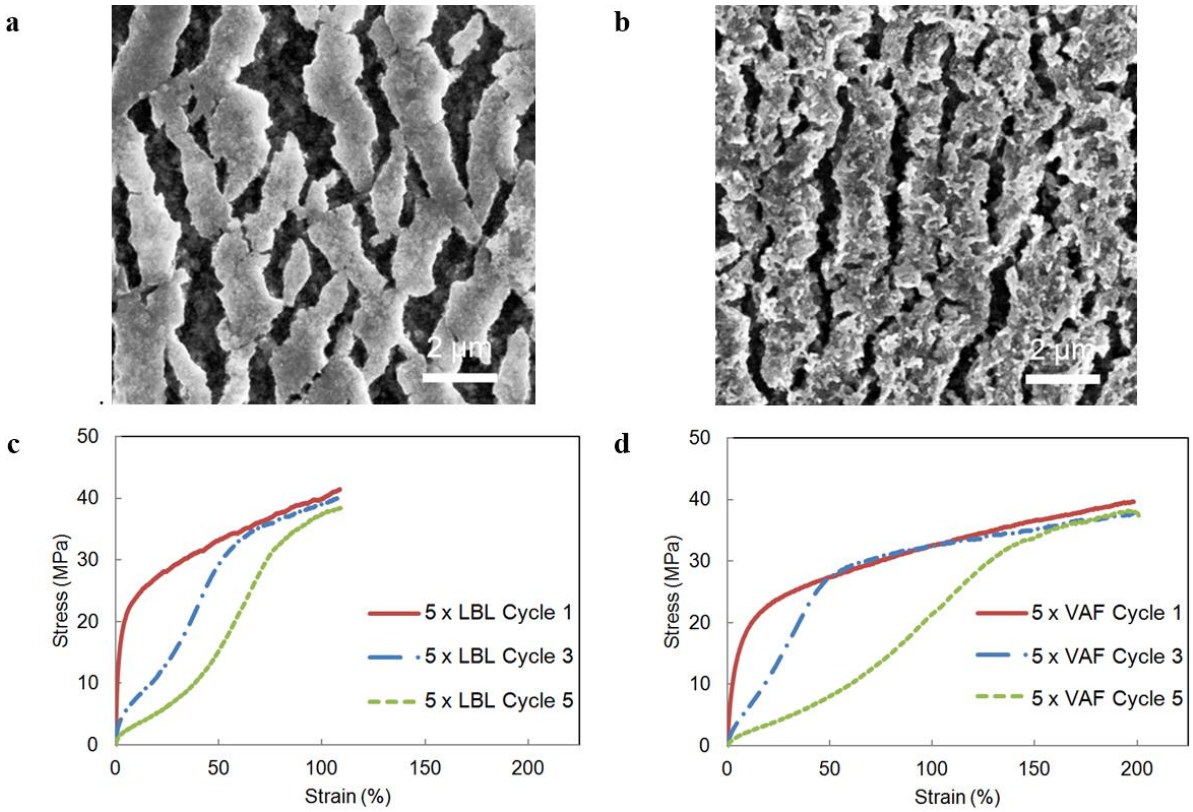

Figure 2.15. a, **b**, SEM images of surfaces of 5 x LBL and 5 x VAF in a relaxed state after five consecutive stretches to 110% and 200%, respectively. **c**, **d**, Stress-strain curves for 5 x LBL and 5 x VAF after specific stretching cycles with ε=110% and 200%, respectively.

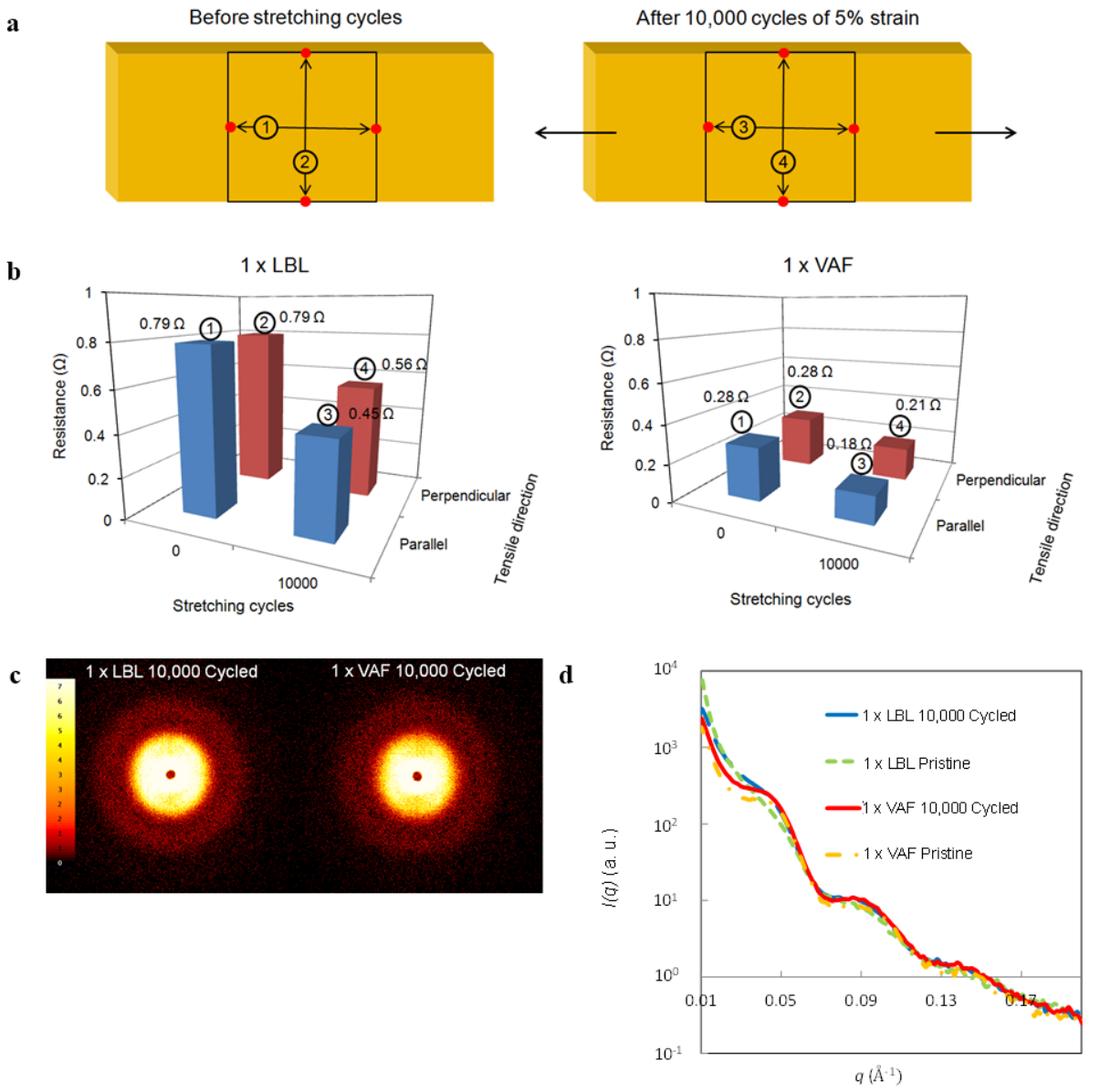

Figure 2.16. Conductivity and small-angle X-ray scattering (SAXS) data after recurrent stretching cycles. a, Illustration of the conductivity measurements by two probe method in different directions after 10,000 stretching cycles with ε=5%. ①: parallel to the tensile direction before strain cycles, ②: perpendicular to the tensile direction before strain cycles, ③: parallel to the tensile direction after strain cycles, and ④: perpendicular to tensile direction after strain cycles. **b**, Resistance data by two-probe method in the directions and recurrent stretching cycles for 1 x LBL and 1 x VAF, respectively. **c**, SAXS beam images of 10,000 cycled 1 x LBL and 1xVAF films. Samples were horizntally placed for measurements. d, Plots of scattering intensity, *I(q)*, in respect to scattering vector, *q*, for 1 x LBL and 1 x VAF. SAXS measurements were performed on the center of the films.

2.9.5 Electron Transport under Various Conditions

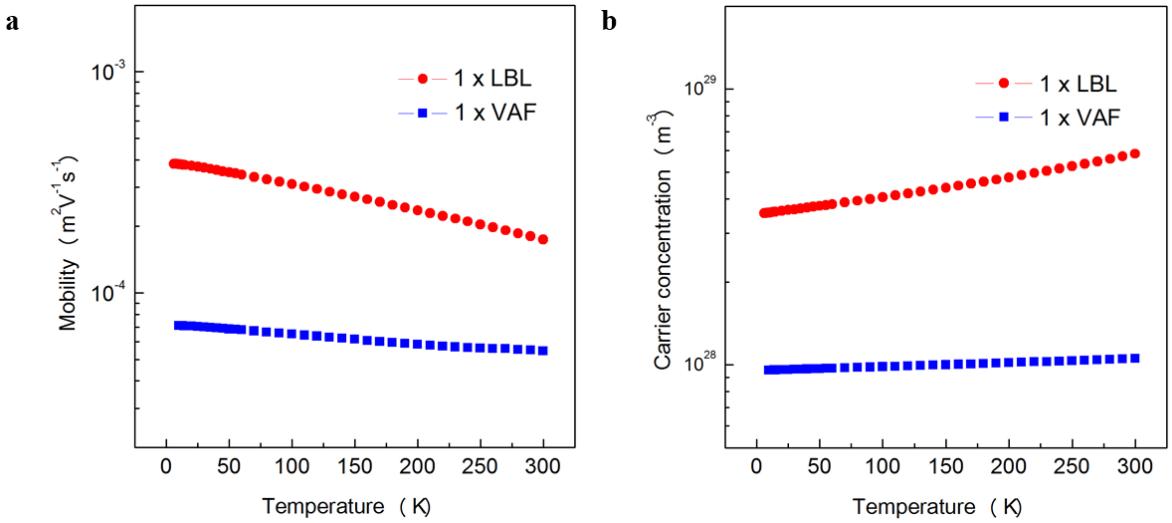

Figure 2.17. a, Electron mobility and **b**, Carrier concentration of 1 x LBL and 1 x VAF determined by the Hall effect measurements.

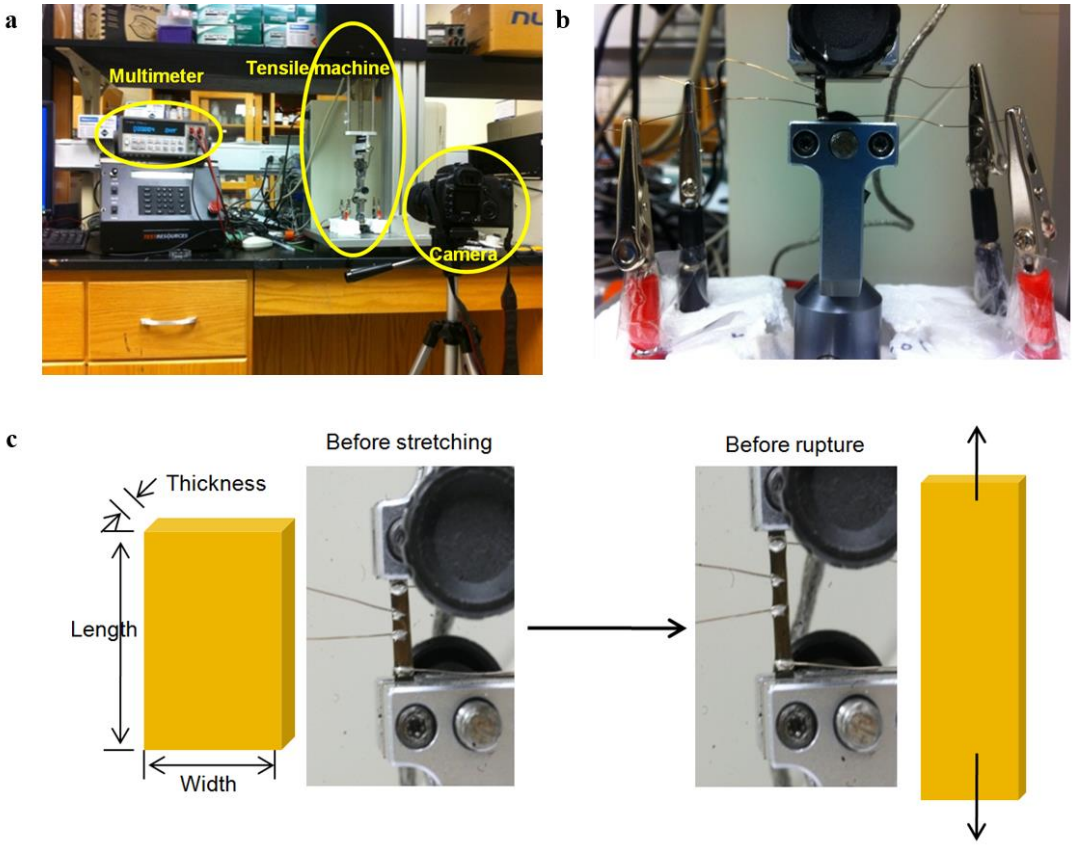

Figure 2.18. Photographic images for the set up used in measuring conductivity and calculating *v* to tensile strain dependence with four-probe method exemplified for a 1 x VAF. Geometrical terms are specified. The four probes were placed on the sample as shown in **b** and **c**. Change of resistance on the multimeter and change of strain on the display of tensile machine (just below the multimeter) were video recorded together as shown in **a**. Calculated Poisson's ratios were as follows: $v_{\text{LBL, thickness}} = 0.26$, and $v_{\text{LBL, width}} = 0.14$, $v_{\text{VAF, thickness}} = 0.39$, and $v_{\text{VAF, width}} = 0.12$.

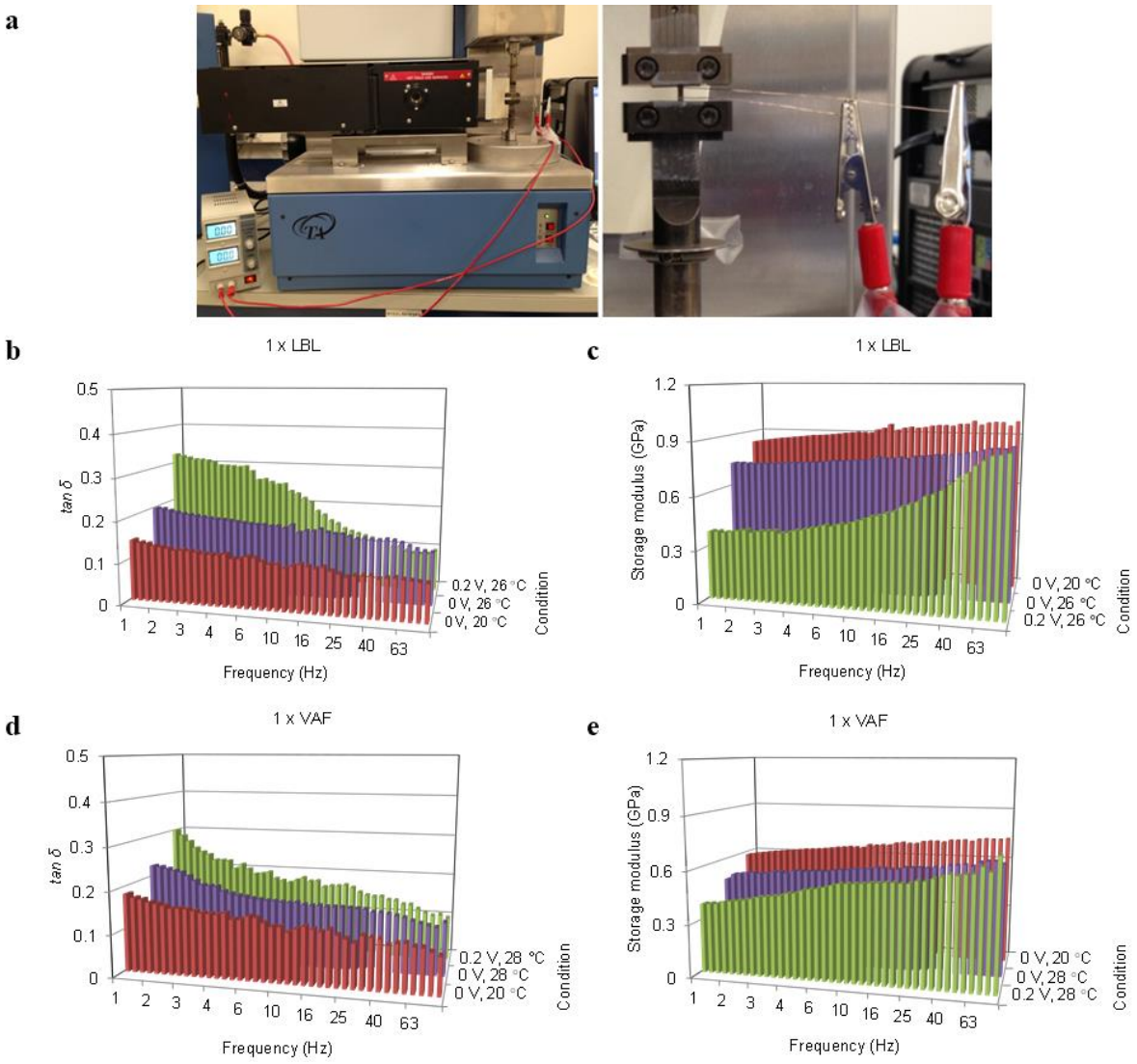

Figure 2.19. Damping properties of polyurethane-nanoparticle nanocomposites with 0 V at the relevant temperatures (purple bars) under frequency ranges from 1-90 Hz with reference conditions with 0 and 0.2 V. a, Experimental setup for measuring damping properties with voltage. **b**, **c**, damping parameter *tan δ* and storage modulus of 1 x LBL, respectively. **d**, **e**, damping parameter *tan δ* and storage modulus of 1 x VAF, respectively.

When 0.2 V was applied, temperature of composites increased to 26 °C and 28 °C for 1 x LBL and 1 x VAF, respectively. To show that change of damping properties at the low frequency region were mainly caused by applied voltage, those with no voltage and at the temperature of 26 °C for 1 x LBL and 28 °C for 1 x VAF were measured. Data showed applied

small voltage significantly tuned damping properties especially at the low frequency region while only temperature couldn’t tune the damping properties at specific frequency ranges instead it slightly affected over the entire frequency region.

CHAPTER III

Reconfigurable Chiroptical Nanocomposites with Chirality Transfer from the Macro- to the Nanoscale

Reproduced with minor modifications with permission from Kim, Y.; Yeom, B.; Arteaga, O.; Yoo, S. J.; Lee, S. G.; Kim, J. G.; Kotov, N. A., "Reconfigurable chiroptical nanocomposites with chirality transfer from the macro- to the nanoscale." *Nature Materials* (2016) doi:10.1038/nmat4525.

3.1 Abstract

Nanostructures with chiral geometries exhibit strong polarization rotation. However, achieving reversible modulation of chirality and polarization rotation in device-friendly solid-state films is difficult for rigid materials. Here, we describe nanocomposites, made by conformally coating twisted elastic substrates with films assembled layer-by-layer from plasmonic nanocolloids, whose nanoscale geometry and rotatory optical activity can be reversibly reconfigured and cyclically modulated by macroscale stretching, with up to tenfold concomitant increases in ellipticity. We show that the chiroptical activity at 660 nm of gold nanoparticle composites is associated with circular extinction from linear effects. The polarization rotation at 550 nm originates from the chirality of nanoparticle chains with an S-like shape that exhibit a non-planar buckled geometry, with the handedness of the substrate's macroscale twist determining the handedness of the S-like chains. Chiroptical effects at the nexus of mechanics, excitonics and plasmonics open new operational principles for optical and optoelectronic devices from nanoparticles, carbon nanotubes and other nanoscale components.

3.2 Introduction and Background

Optically active chiral materials have been known since the time of Louis Pasteur and are predominantly based on chiral geometries of sp^3-hybridized carbon atoms[103]. Chiral isomers typically found in organic chemistry generally exhibit modest chiroptical anisotropy, have limited spectral range, and are problematic to separate. The advent of nanoscale engineering has brought about the ability to create new types of chiral structures that can be made by design in pure forms of stereoisomers. Chiral metallic and semiconducting nanostructures have been shown to exhibit particularly strong optical activities in a wide region of the electromagnetic spectrum[104–106]. The origin of high chiroptical activity of nanoscale assemblies[104] is linked to high polarizability of nanoscale inorganic materials, leading to plasmonic and excitonic effects on the polarization rotation of incident photons[107].

Both bottom-up and top-down manufacturing processes have been used to impart nanoscale chirality to complex systems of electronic oscillators, often described as photonic materials[34,61,108,109]. Use of chiral helical templates[66,110,111] and chiral polymeric matrices[112,113] exemplifies bottom-up assembly of electronic resonators, whereas direct laser writing[114], lithography[115], and glancing angle deposition[116] represent current top-down methods. These preparatory techniques have expanded the technological relevance of chirality from drug design to new optical devices[61,108,64,114] and (bio)chemical analyses[117]. However, both the bottom-up and top-down methods tend to produce 'rigid' systems: their chiral geometry is determined by either strong chemical bonds, supramolecular networks or lithographic masks. Modulation of rotatory optical activity in these structures necessitates modifications of their manufacturing protocols, templates or DNA-bridging sequence, and so on. 'Flexible' chiral geometries have

thus far been demonstrated only in solutions[118–120] and reversible modulation of optical properties will be transformative for solid-state optical devices, microelectromechanical systems and other technological areas of chiroptical materials that are just beginning to emerge[34,64,66,114,115].

Gold and other NPs dispersed in polymers can self-organize into nanoscale geometries with three-dimensional (3D) patterns[55,94]. High charge carrier concentrations and strong asymmetries of these assemblies are conducive to strong polarization rotation in their composites. Considering the well-recognized versatility of nanoscale composites, finding a method to prepare NP assemblies with specific handedness in NP organization would lead to a large family of new optical materials with a possibility of high rotatory activity.

3.3 Macro-to-Nano Transfer of Chirality

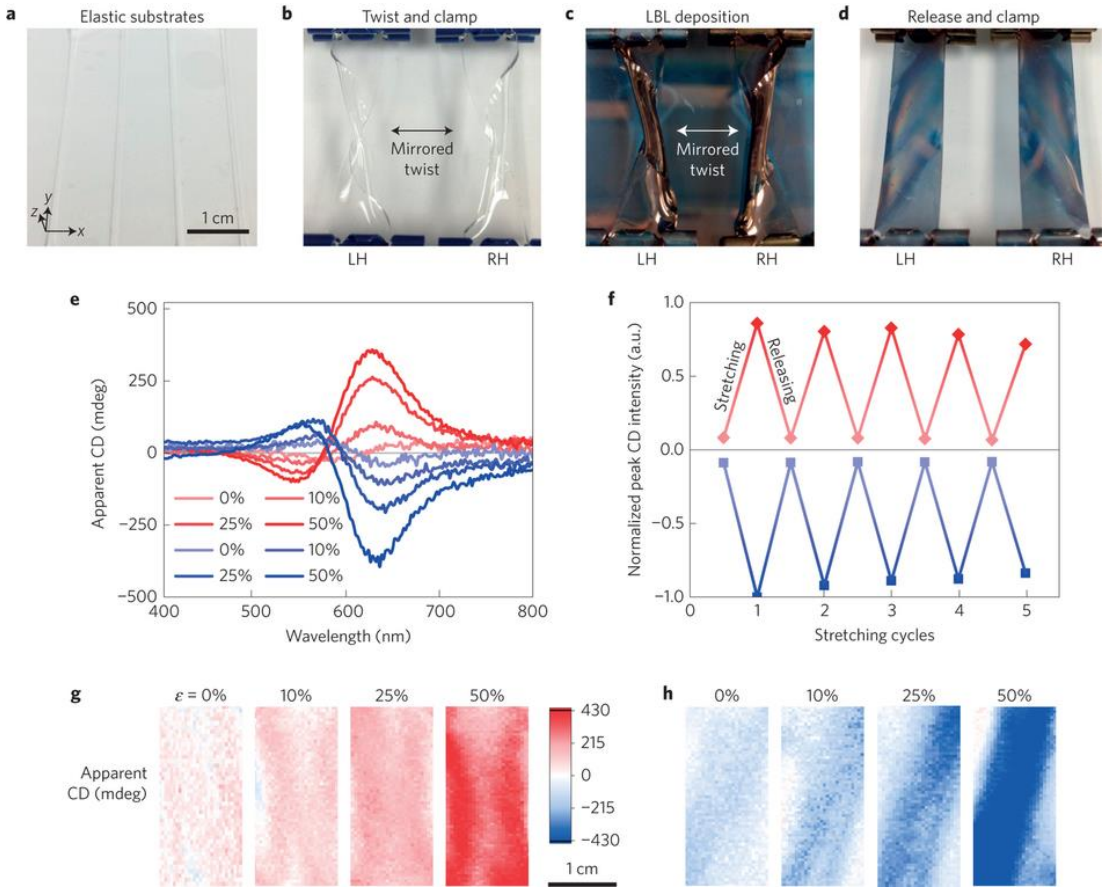

Figure 3.1. Strain-modulated rotatory optical activity in AuNP multilayers. a, Neat PDMS substrates on a glass slide with right-handed Cartesian coordinates. **b**, PDMS substrates twisted in opposite directions. Samples with left-handed and right-handed twists are denoted as LH and RH, respectively. Clamps in **b** are retained during LBL deposition. **c**, PDMS substrates after deposition of $(PU/NP)_5$ in LH or RH twisted states. **d**, Relaxed (flattened) PDMS substrates coated with Au NP multilayers. Samples were stretched along the *y* axis. Scale for **a**–**d** is given in **a**. **e**, Apparent CD spectra of LH and RH samples under ε = 0, 10, 25 and 50%. **f**, Peak CD values of LH and RH for five cycles of reversible stretching from 0 to 50% (see also Fig. 3.27 for up to 10,000 cycles). For all spectra in this study, red colors signify LH samples and blue colors signify RH samples. **g**,**h**, Macroscale mapping of rotatory optical activity under various strain levels from 0% to 50% of LH and RH samples, respectively. Color bar for apparent CD in mdeg and scale for images **g**,**h** are given in **g**. Mapping data were obtained from peak and dip wavelengths of LH and RH, respectively: (**g**) 650 nm, 636 nm, 622 nm and 618 nm for ε = 0, 10, 25 and 50%, respectively, and (**h**) 650 nm, 644 nm, 628 nm and 624 nm for ε = 0, 10, 25 and 50%, respectively. With a beam size of 1.5 mm, apparent CD spectra in the wavelength regime of interest were also measured for each corner and center of the sample strip to show high spatial homogeneity (Fig. 3.32 and 3.33). A total of 20 scans were averaged to obtain the maps of optical activity.

Herein we describe solid-state chiroptical materials for which their handedness at nanoscale can be controlled in a top-down fashion using macroscale deformations. This can be accomplished by taking advantage of 3D stress transfer from macroscale substrates to nanoscale films made by LBL assembly, providing high structural uniformity and transparency[12]. Moreover, polarization rotation can be cyclically modulated by mechanical stretching. Elastic poly(dimethylsiloxane) (PDMS) substrates were initially twisted around the y axis of the substrate in a clockwise or anticlockwise direction by an angle, ω, equal to 360˚ for most experiments (Fig. 3.1a,b); the corresponding samples were denoted as left-handed (LH) or right-handed (RH) (Fig. 3.1d). Most tests in this study were carried out with Au NPs having a diameter of 13.0 ± 0.3 nm that exhibited no chiroptical activity as established by circular dichroism (CD) spectroscopy (Fig. 3.22). Negatively charged Au NPs (Fig. 1.2a,b) were deposited[46] on PDMS (Fig. 3.1c) in the twisted state using positively charged poly(urethane) (PU) (Fig. 1.2c) as an LBL partner. A total of five bilayers, denoted as $(PU/NP)_5$, were deposited; and the substrate was subsequently allowed to relax to the original planar shape (Fig. 3.1d). Besides Au NPs, (6,5) single-walled carbon nanotubes (SWNTs) and 100 nm polymer beads were used for our studies to demonstrate the generality of the observed phenomena.

The layered composites from Au NPs exhibited strong rotatory optical activities observed as distinctive CD peaks around plasmonic resonance wavelengths (Fig. 3.1e). As-prepared, the LH sample had a dip (580 nm) and a peak (660 nm) with an absorbance of 0.87 (Fig. 3.22). LH and RH samples exhibited mirror-image peaks, indicating that chiroptical activity of the materials is determined by the macroscale twist. Emergence of chiroptical

activity was observed with a rotational angle, ω, of 180˚ (Figs 3.24 and 3.25). The simplicity and practicality of controlling the direction of polarization rotation of the films compared with microfabrication techniques or the traditional synthetic methods of organic or NP chemistry[114–116,121] should be noted. Also, no biological or other templates with a priori chirality were used in this work. Benchmark samples prepared without twisting of the original PDMS substrates, samples carrying no Au NPs, or those made under other conditions revealed no rotatory optical activity in the range of wavelengths relevant to this study (Fig. 3.22).

In a search for unique properties that enantioselective composites can contribute to the fields of chemical chirality and chiroptical materials, we investigated how planar stretching of the NP films along the sample's *y* axis (Fig. 3.1) affected their rotatory optical activity. The apparent CD bands became considerably more intense when the strain, ε, increased. Quite remarkably, ellipticity values for plasmonic peaks increased by at least one order of magnitude for both LH and RH samples on stretching to 50% (Fig. 3.1e). Importantly, the chiroptical peaks returned to near their original values when the stress was released. Reversibility of the strain-induced optical response can also be appreciated from the repeated stretch-release cycles (Fig. 3.1f, 3.27 and 3.28b). Also, mappings of the entire centimetre-scale sample area with a pixel resolution of 0.25mm revealed that optical responses at all strain levels in the sample's plane were homogeneous (Fig. 3.1g,h).

3.3.1 Stress Accumulation on Hyperelastic Substrates

COMSOL Multiphysics with a module of Solid Mechanics was employed to better understand deformation mechanics of hyperelastic PDMS strip. For all simulations,

extremely fine physics-controlled mesh was used. Then parametric sweep of the calculations with a rotational increment equal to 3.6° was performed. PDMS (Sylgard 184) substrate is a hyper elastic material (non-linear deformation under large strain, often > 40%) as opposed to Hooke's law in linear elasticity. To adequately calculate mechanical properties of PDMS, the Arruda-Boyce model[122], derived from statistics on polymer chain networks, was set up on COMSOL. Although calculations were also done with other hyper elastic models such as neo-Hookean, Mooney-Rivlin[123,124], and Yeoh[125], this analysis will focus on the results from the Arruda-Boyce model due to its superior ability to represent three-dimensional stress-strain relation with a minimal number of parameters, and its initial shear modulus and chain extensibility. In the settings of the model, N (limiting chain extensibility) was set as 8, as was the basic assumption of the Arruda-Boyce model. Even larger extensibility, such as with N = 40 or 82 for more soft materials, also resulted in calculated values very similar to those from with N = 8. Interestingly, the Mooney-Rivlin two parameter model resulted in von Mises stress one order of magnitude smaller than those from the Arruda-Boyce and Yeoh models. However, stress distribution patterns were very similar for all three models.

In the COMSOL simulation, torsion was applied to the PDMS strip in order to observe the effect of torsion alone. The result differed greatly from the actual PDMS strip (Fig. 3.2). Length during torsion decreased continuously as the rotational angle increased, which one would naturally assume, but this differed from the actual PDMS strip in a surprising way in terms of length, stress distribution and surface smoothness. Additionally, after 360° of torsion, the actual PDMS strip did not drop below the initial strip plane geometry while the torsion-only

simulation did. In the simulation, a rotational angle of 324° was the maximum, likely limited by severely corrugated surface mesh.

In addition to simple torsion, the strip was further stretched to keep the initial length. This was done by setting "no displacement" in all directions, with special attention to the

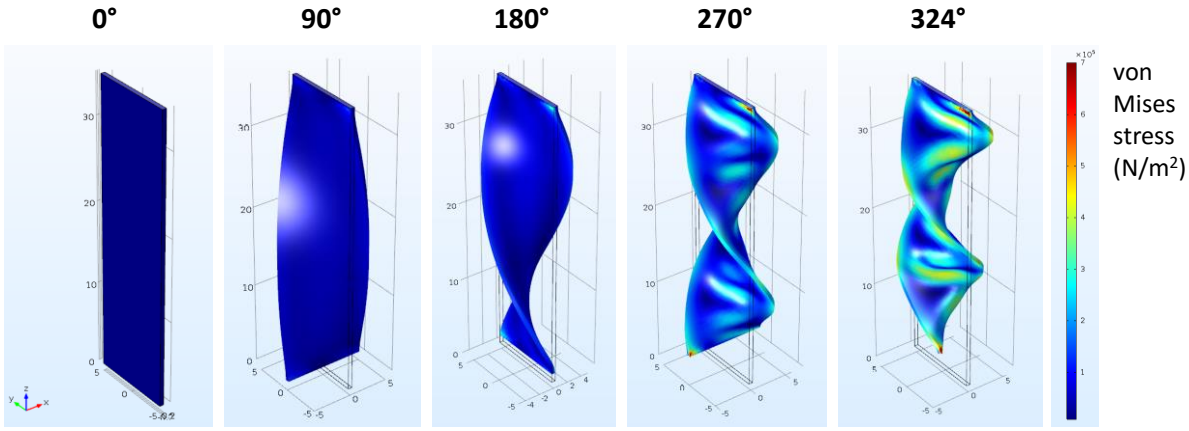

Figure 3.2. Geometrical change with von Mises stress distribution while torsion was solely applied on the strip of PDMS. Top boundary was fixed by setting constraint and bottom boundary was allowed to be rotated along the longitudinal axis. Unit for numbers around the grid: mm.

longitudinal direction. This made the simulation result nearly the same as the real strip (Fig. 3.3). Setting "no displacement" in the longitudinal direction (slight stretching from the perspective of torsion-only applied geometry) was key in making the strip geometry, from which two-fold rotational symmetry structure was obtained, and along the central symmetry line a gradient of curvatures was obtained (Fig. 3.3). From the experimental perspective, bending stress at each representative point was calculated using the Hooke's law, with an assumption of pure bending, to be 0.98 MPa, 0.57 MPa and 0.38 MPa for points 1, 2 and 3,

respectively[126] (Fig. 3.34 and Eq. 3.3). Calculated von Mises stress at each comparable point

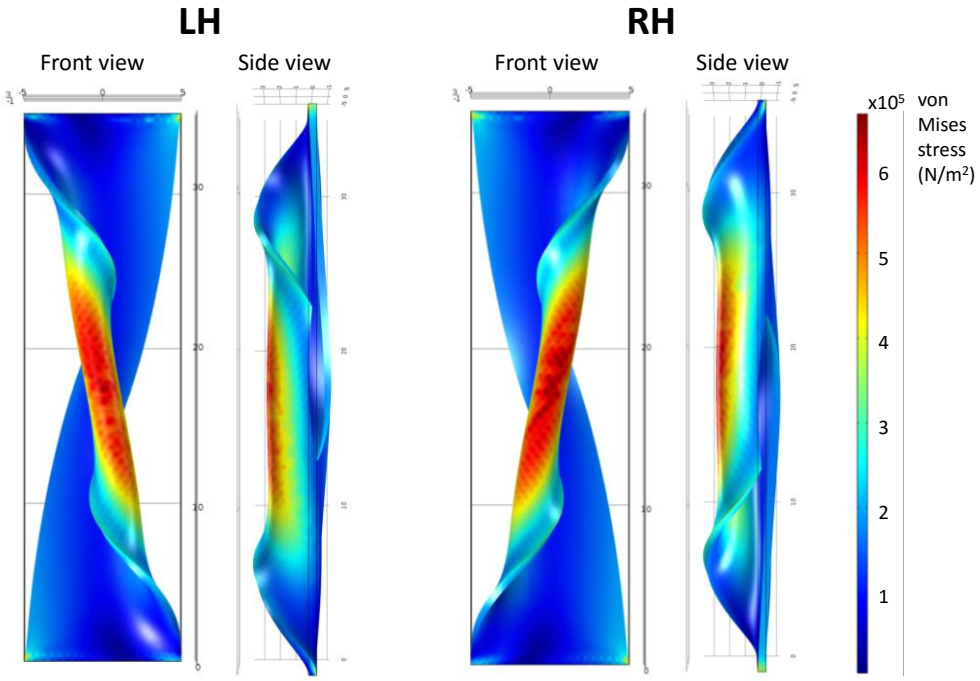

Figure 3.3. Geometrical change with von Mises stress distribution while "torsion plus no displacement" was applied on the strip of PDMS. Simulated images of strips in clockwise and counter clockwise rotation for LH and RH strips, respectively, with von Mises stress distribution represented by colored scale. Unit for numbers around the grid is mm.

was also obtained to be 0.67 MPa, 0.43 MPa and 0.25 MPa. The reason we was able to obtain almost the same calculated results from using both linear (the Hooke's law equation) and hyperelastic models (the Arruda-Boyce model) is that cured PDMS (Sylgard 184) substrate is a hyperelastic material with non-linear deformation under large strain, often > 40%. Overall, COMSOL simulation using the Arruda-Boyce model for non-linear deformation of hyper elastic materials worked exceptionally well in terms of reproducing nearly identical geometry and nearly identical stress distribution.

3.3.2 Stress Evaluation for Each Principal Direction

The accumulated stress presented as von Mises stress in Fig. 3.3 is further evaluated to show contribution from each principal direction using second Piola Kirchhoff stress.

As it can be clearly seen from the colored figures, stress contribution from planar directions were significant (Fig. 3.4). Lateral contribution (Y component) from the torsion was the dominant. Longitudinal contribution (Z component) was also fairly significant which should originate from slight stretching of the strips while torsion, by the setting of no displacement. Another planar component (YZ) was also notable. However, stress

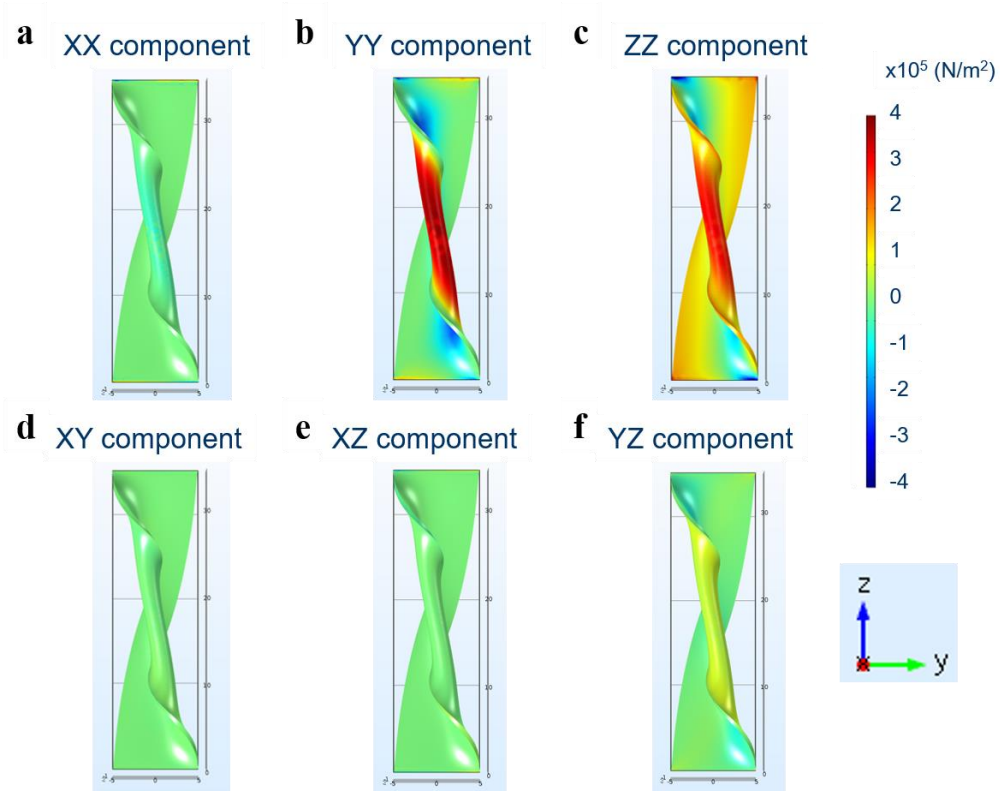

Figure 3.4. Stress evaluation for each principal direction. Principal directions are represented in the right corner of the figure. Stress distribution is represented by colored scale. Unit for numbers around the grid is mm.

contribution from the direction normal to the original plane (X component) and related out of plane components (XY and XZ) were very minor.

3.4 Rotatory Optical Activity in Superposed Layers

3.4.1 Origin of Rotatory Optical Activity

Rotatory optical activity of the stratified optical media can be complex when each layer interacting with the transmitting beam has a distinctively different optical property, such as dichroic and birefringent. The observed CD bands can be associated with structural chirality of the individual strata, that is, deposited LBL films; we will refer to this portion of rotatory optical activity as CD_{NP} in the case of NP films. Also, rotatory optical activity can be associated with superposed achiral films when the principal axes of linear dichroism (LD) in one film and linear birefringence (LB) in the other film form a non-zero dihedral angle; we shall refer to this contribution as circular extinction from linear effects, CE_{linear}.

Besides the chiroptical activity arise from material properties of consisting layers, we carefully considered the following mechanisms for potential source of optical activities: (1) dipolar interaction between chiral molecules (or segment of a polymeric chain) and plasmonic particles[107], (2) effective medium interactions when metal nanoparticles embedded in a chiral medium[127] (formed, for instance, by twisting the polymeric chains of LBL components), (3) chiroplasmonic effects from a chiral molecule or portion of a polymeric chain located in hot-spots between metal particles[128] and (4) polarization rotation associated with combinatory

effects of vectorial LD and LB, i.e. a non-zero dihedral angle between the principal axes of linear optical activities as well as significat magnitudes of them, CE_{linear}.

To better understand the possibile contribution of the above mechanisms, we recorded absorbance and CD spectra from UV to near-infrared (NIR) range for chiroptical nanocomposites both from AuNPs and SWNTs. The multiple relevant control samples, e.g. AuNPs, SWNTs, PU, PVA and PDMS etc., were measured as well (Fig. 3.16, 3.22 and 3.23). No chiroptical activities for absorption band of polymers were found. Also, no CD signals in the relevant ranges wavelengths for the aggregates of PU/AuNP and PVA/SWNT (mix ratio of solution is 1:1000 v/v) were observed. The obtained data do not allow us to base this manuscript on optical effects mentioned above.

Additionally, we evaluated a possibility that strong polarization rotation and strain modulation are related to the plasmonic enhancement of chiral activity of organic components located in gaps between the NPs[129]. However, interparticle gap measured by X-ray scattering and direct observation from traditional TEM and TEM tomography showed virtual constancy of 13.8 ± 0.1 nm before and after stretching (Fig. 3.40 and 3.41). This data indicates that variations of electrical-field intensity in the plasmonic hot-spots alone, without considerable reorganization of NP networks in the composite, are not responsible for the strain-induced chiroptical effects.

On the balance of diverse data sets, including experimental and computational simulations, and careful considerations, we exclude possibilities of above (1)-(3) mechanisms for the origin of chiroptical activities. Mechanism (4) is responsible for the apparent CD in the cracked side originating from superposition of linear anisotropies with a non-zero dihedral

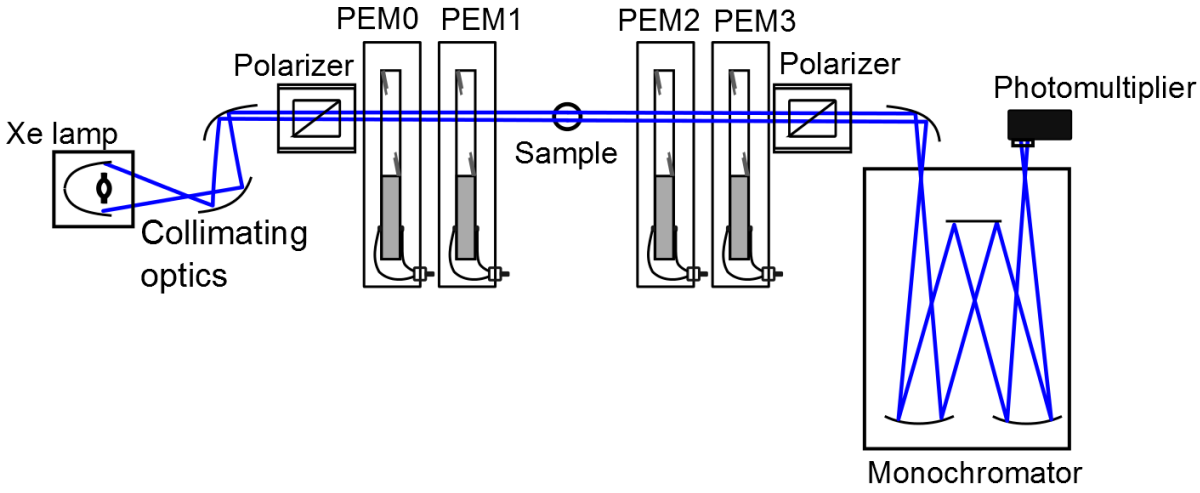

Figure 3.5. Schematic of Mueller polarimetry device setup.

angle in stratified optical media, while the buckled side indeed had chiroptical activity by strain-induced assembly of plasmonic/excitonic nanoscale materials. This conclusion was comprehensively analyzed and supported by data from experimental measurements of Mueller matrix polarimetry and its polar decomposition and theoretical study of differential Mueller matrix in the following sections.

3.4.2 Mueller Matrix Polarimetry

Given the large amount of strain resulting in increased LB in PDMS and non-zero dihedral angles in between PDMS and NP films, one should expect that the measured apparent CD spectra are a superposition of CD_{NP} and CE_{linear}. To elucidate the complex optical activity, we first implemented Mueller matrix polarimetry[130] to obtain each component of apparent CD, apparent CB, LD and LB, in each distinct optical strata, buckled layer, PDMS and cracked layer.

Polarimetric chiroptical measurements were done with the spectroscopic Mueller polarimeter[130]. This instrument uses four photoelastic modulators (PEMs) with different

frequencies to modulate polarization state of light both before and after the sample (Fig. 3.5). Fourier analysis of the time varying signal delivers simultaneously all sixteen elements of the Mueller matrix with high precision. All transmission measurements were done in the straight-through configuration, using a rectangular spot size of approximately 15 mm x 8 mm. A smaller round beam, with 1.5 mm diameter, was also applied to measure optical activity of small spots for test of homogeneity.

The 4x4 Mueller matrix (**M**) is a linear operator that provides the optical response of a material for any arbitrary form of polarization. Complete polarimeters measure all the elements of the Mueller matrix, while partial polarimeters measure only some selected elements. For instance, all commercial circular dichroism spectropolarimeters were intended for analysis in solutions to deliver only M03 element of the Mueller matrix. This is achieved by modulating only the input light polarization with a single PEM placed before the sample. Under certain conditions M03 can be taken as CD, but, in most general cases, especially for complex optical media with several optically active strata, reliable measurements and calculations of CD require knowledge of all Mueller matrix elements.

In a homogeneous and non-depolarizing medium, the normalized Mueller matrix has at most six parameters[131]. A non-depolarizing Mueller matrix is called a Mueller-Jones matrix and can be represented as follows[132]:

$$\mathbf{M} = \exp(\mathbf{L}) = \exp\begin{bmatrix} 0 & -LD & -LD' & CD \\ -LD & 0 & CB & LB' \\ -LD' & -CB & 0 & -LB \\ CD & -LB' & LB & 0 \end{bmatrix} \qquad \text{(Eq. 3.1)}$$

where, **L** is the differential Mueller matrix. The elements of **L** have a direct physical interpretation as the fundamental optical properties for light-matter interaction: LD - horizontal

linear dichroism, LB - horizontal linear birefringence, LD´- 45˚ linear dichroism, LB´- 45˚ linear birefringence, CD - circular dichroism and CB - circular birefringence.

Once **M** is experimentally determined, **L** can be calculated numerically from its logarithm (**L** = Ln**M**) or analytical approach[133]. Then the CD of a medium can be obtained. However, when there is a depolarization, the symmetry of **L** may be broken, and the optical properties are then taken as the average values of related elements, e.g. CD = (L03+L30)/2[132]. However, for the plasmonic samples measured herein, the depolarization was negligible and the symmetry of Eq. 3.1 is applicable (Fig. 3.6).

The physical interpretation that we have provided for the elements of **L** corresponds to a medium that is homogenous in the direction of light propagation. In the case of inhomogeneous system, for example, by a medium and an anisotropic substrate, the representation given by Eq. 3.1 is still valid but, in such conditions, the apparent optical effects in **L** do not necessarily correspond to fundamental properties of the medium. Because, it is possible that the optical effects in **L** arise from the compounded effect of the different strata, e.g. dichroic NP layers and a birefringent PDMS substrate. Thus, apparent CD of our samples could be decomposed into one from assembled NPs and the other from combinatory effects of vectorial linear parameters. The latter, called as circular extinction due to linear effects, CE_{linear}, tend to be significant if LB of substrate is large and it is non-parallel with respect to LD of medium. For optically complex systems it can result in misinterpretation of apparent CD data, directly obtained from Mueller matrix polarimetry. To avoid that, we carefully considered optical activity of each strata of our samples along the light path and then employed polar decomposition to further deconvolute different contributions to the apparent chiroptical

activity. For comprehensive study, we also considered spatial homogeneity of our samples and analyzed their optical properties by theoretical studies of differential Mueller matrix.

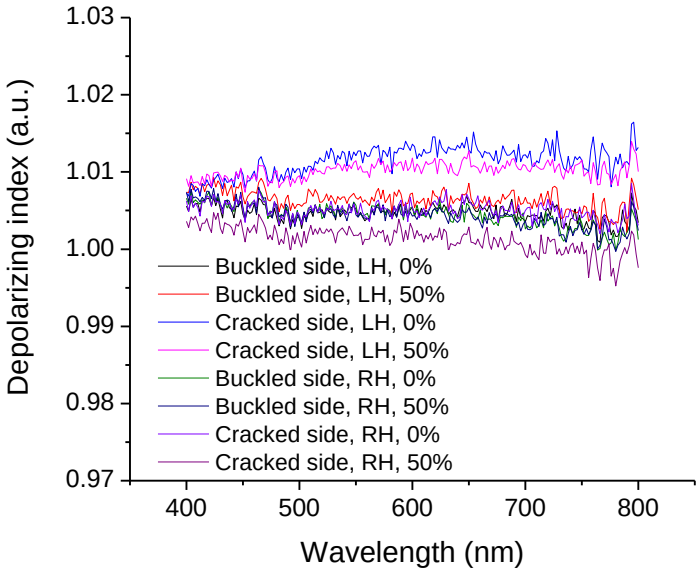

Figure 3.6. Depolarizing index of single sided samples of LH and RH under ε=0% and 50%.

3.4.3 Polar Decomposition of apparent CD into CD_{NP} and CE_{linear}

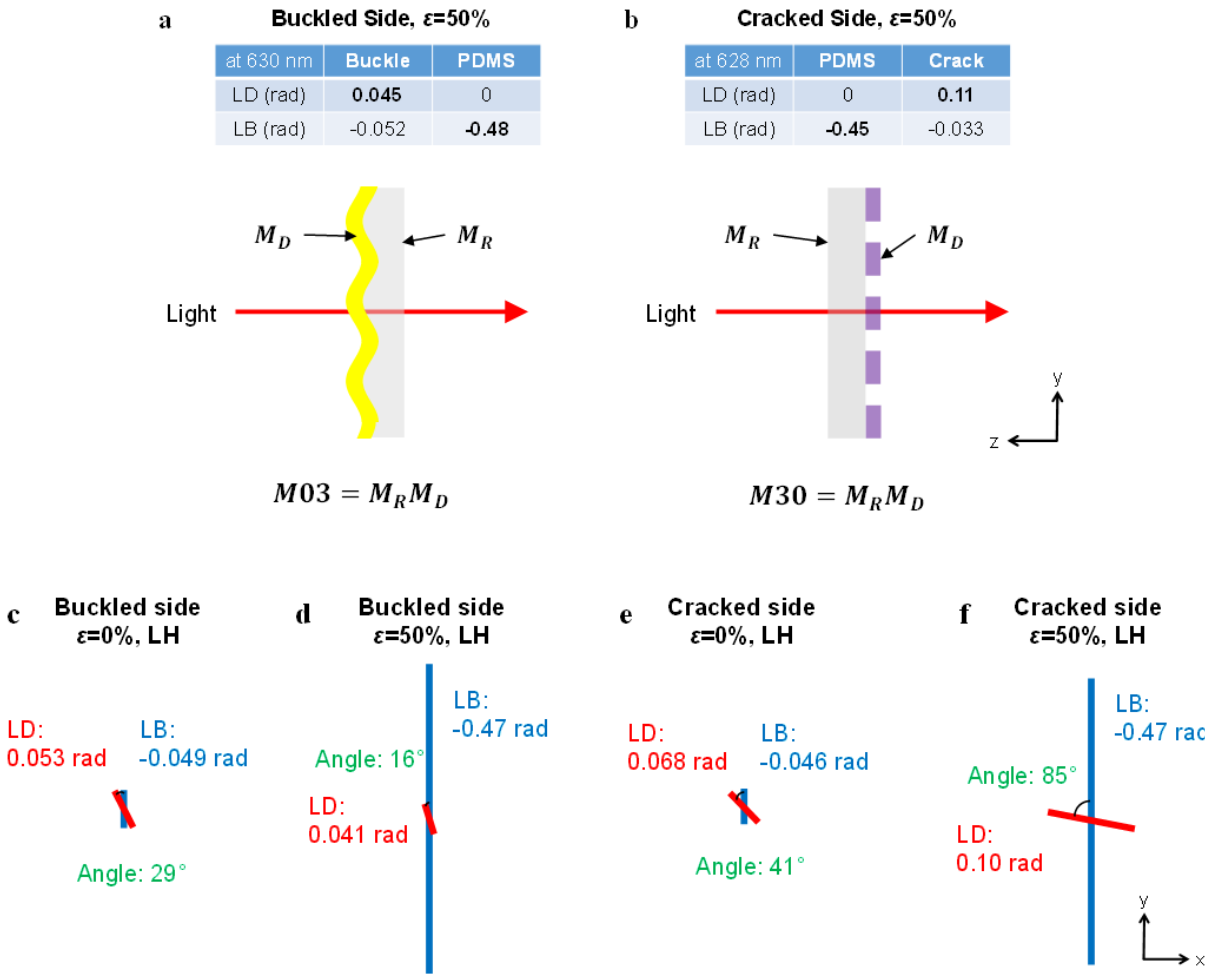

Figure 3.7. Schematics for understanding of polar decomposition in experimental procedure for buckled side (a) and cracked side (b). Summarized data (values of LH and RH were averaged) for experimental LD and LB of each layer. M_D and M_R were assigned to each layer accordingly. M03 and M30 were regarded as CD_{NP} for buckled and cracked sides, respectively. **c-f**, Diagrams for magnitude of LD from NP layer and LB from PDMS with dihedral angles in between them for buckled side, ε = 0%, LH (**c**), buckled side, ε = 50%, LH (**d**), cracked side, ε = 0%, LH (**e**), and cracked side, ε = 50%, LH (**f**). LD is from NP layer and LB is from PDMS substrate. Direction of LB was considered same as stretching direction regardless of tensile stress with an assumption that even very small tensile stress (which was actually applied to make sample surface flat for measurements) would align polymer chains parallel to the direction.

In this section, we study case-by-case the chiroptical activity for our samples arising from distinctness of the optical strata (NPs layers and PDMS) in the direction of light propagation. Based on the experimental Mueller matrix polarimetry data, NP layer had strong LD whereas PDMS had strong LB (Fig. 3.7 and 3.16). Any non-depolarizing Mueller matrix can be decomposed in the product of two Mueller matrices, one being a pure retarder and the other a pure diattenuator. As the matrix product is not commutative two possibilities are allowed[134].

$$\boldsymbol{M = M_R M_D,} \quad \text{(Eq. 3.2a)}$$

$$\boldsymbol{M = M_D M_R,} \quad \text{(Eq. 3.2b)}$$

where, $\boldsymbol{M_R}$ corresponds to a retarder, i.e. a medium having only retarding properties such as LB and CB, and $\boldsymbol{M_D}$ corresponds to a diattenuator, i. e. a medium having only diattenuating properties such as LD and CD.

Our single-sided samples agree well enough with this product decomposition (Fig. 3.7). In this case PDMS substrate is the retarding medium and NP layer would be the diattenuating medium. The agreement to this product model is not perfect because NP film also displays some LB but it tends to be much smaller than the one coming from PDMS substrate, especially when samples are strained.

In all optical measurements in this study, light passed through samples in the order of "buckled side, PDMS then cracked side" for double-side samples, and "buckled side then PDMS" and "PDMS then cracked side" for single-side samples. Angle of light incidence was always kept same as normal to the samples' surface. Thus, for the analysis of buckled side on PDMS, Eq. 3.2a will hold and M03 will be better representing CD_{NP}, while Eq. 3.2b will hold

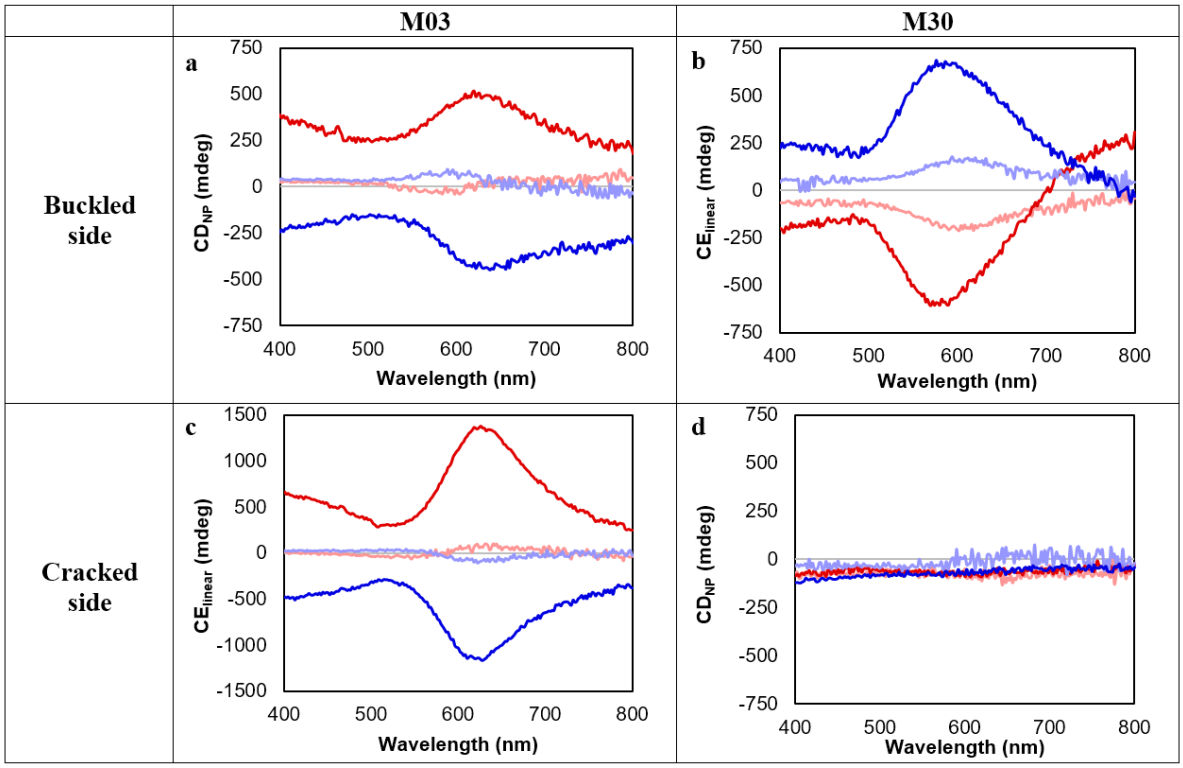

Figure 3.8. M03 and M30 elements from Mueller matrix polarimetry measurements. Spectra for LH and RH samples under ε = 0% and 50% for buckled side only (**a**, **b**) and cracked side only (**c**, **d**) on PDMS substrate. For all spectra in this study, red and blue colors indicate LH and RH samples, and lighter and darker colors indicate ε = 0% and 50%, respectively, unless otherwise specified.

for cracked side on PDMS and M30 will be CD_{NP}. M03 of buckled side had fairly strong response, while M30 from cracked side had nearly zero response (Fig. 3.8). This is a demonstration that buckled side had strong CD_{NP} from assembled NPs, whereas cracked side did not. This may not be completely correct but should be the most reasonably acceptable way of interpreting apparent CD in our superposed solid-state layers.

We found that the optical activity of the cracked side is primarily associated with CE_{linear}, while contributing little to the CD_{NP}. The analysis also indicated that chiroptical activity from the cracked side is responsible for the apparent CD peak at 640-660 nm in Fig. 3.1e. On the

other hand, the apparent CD peak observed at 550 nm corresponds to the rotatory activity of the buckled layer, which included both CD_{NP} and CE_{linear} (Fig. 3.8). The study of CE_{linear} can have potential technological significance as witnessed in Fig. 3.21 but, here stereoselective preparation of chiral nanostructures in solid state represents particular academic and technological novelty. Thus, identification of the nanoscale organization of the LBL films of NPs on the buckled sides and understanding of their chiroptical activity, CD_{NP}, will be the primary focus now.

3.5 Solid-State Self-Assembly into Chiral Superstructures

3.5.1 Strain-induced Chiral Assembly

To explain the mechanism of strain-modulated chiroptical activity of NP multilayers on buckled sides, we first needed to identify the representative chiral elements in the composite films responsible for polarization rotation. Observed reversal of CD spectra with the direction of initial twist indicates that mechanical deformation of the PDMS substrate is essential for the emergence of nanoscale chirality (Fig. 3.1e). When twisted substrate was released, NP layers on convex and concave surfaces were exposed to compressive and tensile stresses, respectively, opposite to those built into the twisted substrates (Fig. 3.9b,c). The stress distribution along the surfaces of the sample is not uniform but has a strong gradient (Fig. 3.9d-i). For instance, the bending stresses for points 1, 2 and 3 on the convex side in Fig. 3.9a,b are calculated to be about 0.98MPa, 0.57MPa and 0.38MPa, respectively (Fig. 3.3). This stress gradient (Fig. 3.9) combined with mismatched materials properties (Table 3.1) should effectively transfer

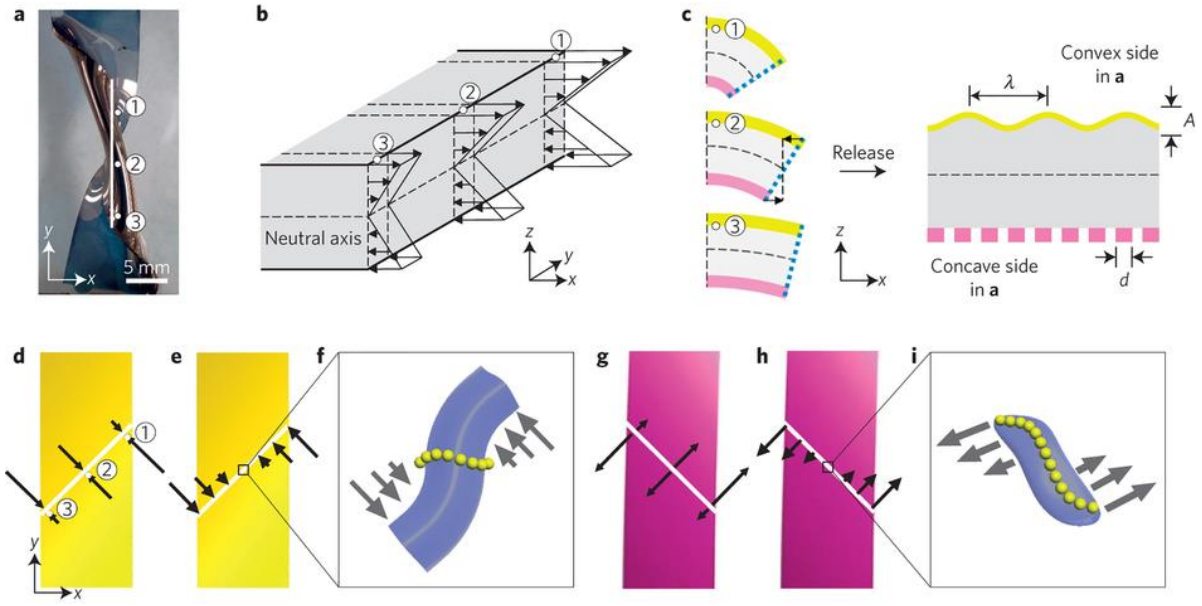

Figure 3.9. Stresses in twisted PDMS substrates with LBL composite films. a, Photograph of a twisted and clamped LH sample with marked spots 1, 2 and 3 on the convex side. **b**, Stress distribution in a PDMS substrate. Stresses of different magnitudes are generated at points 1, 2 and 3 for twisting deformation of the samples. Stresses of the same magnitude but opposite directions are generated in convex and concave surfaces of samples. **c**, Schematic of the cross-sectional view of the sample in **a**. Deposited NP layers undergo compression and extension on convex and concave sides, to form buckled and cracked sides in the relaxed flat state, respectively. Yellow and pink colors represent buckled and cracked sides, respectively. Blue dashed line indicates the edge of the film. *A* and *d* are the height of the buckles and width of the gold islands in the cracked side, respectively. **d**,**e**, Gradients of compressive stresses and net stresses on a buckled side exhibiting C_2 symmetry. **f**, Schematic of an S-like NP chain constituting buckles. **g**,**h**, Gradients of tensional stresses and net stresses on a cracked side exhibiting C_2 symmetry. **i**, Schematic of an NP chain constituting islands. The NPs assemble in the chain structures similarly to those in the buckles in the cracked side due to the strain gradient; however, the chirality factor in this case is small owing to the smallness of the out-of-plane component.

macroscale chirality (10^{-2} m) to nanoscale thin films (10^{-10}-10^{-6} m) on release of samples. This transfer also should allow us to obtain optical activity in the visible spectral range. However, a symmetrical stress distribution (that is, samples obtained on a roll-shaped substrate) led to negligible chiroptical activities (Fig. 3.37). The buckles have asymmetric shapes with dimensions of 10^{-6} m (Fig. 3.38), which coincide with the expected dimensions of plasmonic

structures known to generate strong polarization rotation at 400-800 nm (refs [66,112,115,116,121]). We initially reasoned that NP buckles are responsible for the chiroptical activity. However, stretching LH and RH samples along the *y* axis caused them to be more symmetrical in the *x*-*y* plane especially at a higher strain level. This factor presumably leads to a decrease of chiroptical activity and differentiation between strained LH and RH samples, which is opposite to experimental observations (Fig. 3.8, 3.10b, and 3.48a).

This contradiction prompted us to explore multiple optical effects possible for hybrid polymer-particle materials. These included, among others, dipolar coupling between chiral sp^3 atoms with NP plasmons, interactions of metal NPs with a chiral medium, and electrodynamic effects for highly polarizable systems in the presence of chiral components[117]. The absence of CD signals for composite components regardless of twist or NP presence for 200-900 nm observed in the numerous blank experiments (Fig. 3.22 and 3.23) did not allow us to attribute the observed chiroptical phenomena to any of these effects mentioned above. This is also true for different absorbing materials including semiconducting SWNTs (see below). We gave extensive consideration to 'hotspot'-induced chiroptical activity[107,117,129]. However, the average distance between NPs obtained from small-angle X-ray scattering (SAXS) and transmission electron microscopy (TEM) data was found to be on average of 13.8 ± 0.1 nm, and was virtually unaffected by stretching (Fig. 3.40 and 3.41). The constancy of the interparticle gap indicated that variations of electrical-field intensity in the plasmonic hotspots alone, without considerable reorganization of NP networks in the composite, are not responsible for the strain-induced chiroptical effects; these effects are likely to make only a minor contribution to the observed phenomena.

3.5.2 Reconfigured S-like NP chains

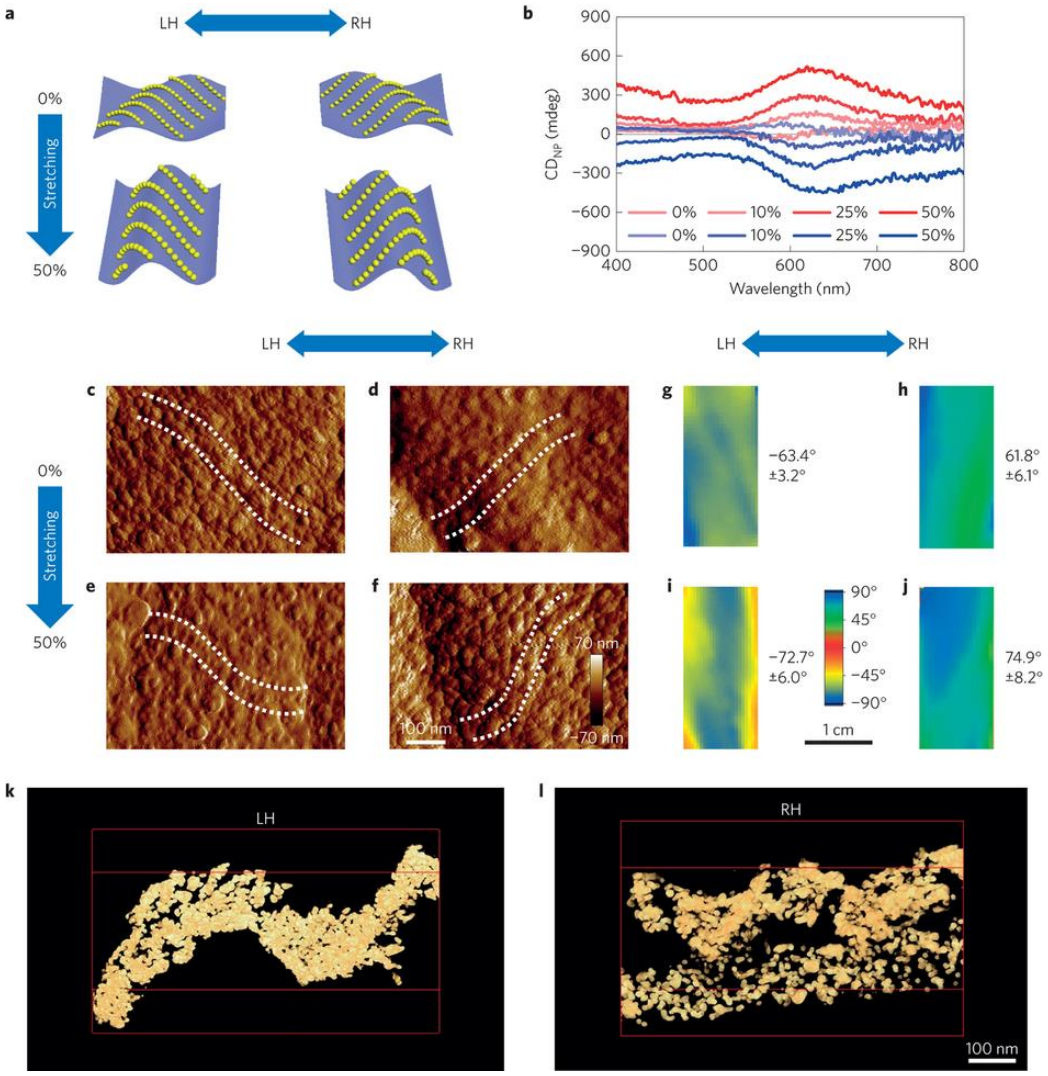

Figure 3.10. Strain-induced chiroptically active NP assemblies on buckled sides. All data in this figure set are from samples having only buckled sides. **a**, Schematic drawings of mirrored images of NP chains under ε = 0 and 50%. **b**, CD_{NP} spectra of LH and RH samples under various strains from 0 to 50%. See fig. 3.11 for simulated spectra. Red colors signify LH samples and blue colors signify RH samples. **c**–**f**, Magnified AFM images of LH, ε = 0% (**c**), RH, ε = 0% (**d**), LH, ε = 50% (**e**), and RH, ε = 50% (**f**). Large-area AFM images are in Fig. 3.38. Height (z axis) and planar (x–y plane) scales for images **c**–**f** are given in **f**. **g**–**j**, LD orientation of LH, ε = 0% at 600 nm (**g**), RH, ε = 0% at 600 nm (**h**), LH, ε = 50% at 565 nm (**i**), and RH, ε = 50% at 568 nm (**j**). A total of 20 scans were averaged to obtain the maps of optical activity. Color angle bar and scale for images **g**–**j** are given in **i**. Angles are projectable using classical 2D Cartesian coordinates. **k**,**l**, 3D TEM tomography images of $(PU/NP)_5$ of LH (**k**) and RH (**l**). See Supplementary Movies 1–4* for full 3D rendering. Scale for images **k**,**l** is given in **l**.

To better understand the emergence of chiroptical activity, we studied the surface of buckled sides with AFM and TEM. Aside from the formation of buckles, deformation of LBL films on flattening of PDMS substrates also resulted in the formation of NP chains with S-like shapes (Figs 3.9d-i, 3.10c-f and 3.38). Although the geometry of NP assemblies in strained LBL films can be very complex, we reasoned that S-like NP chains can serve as the simplest geometrical element capable of visualizing and capturing the essential geometrical and optical properties of these films. Hence, we evaluated their 3D geometry thoroughly with and without strain. The S-like NP chains are fully 3D, significantly protruding in the *z* direction as observed by TEM tomography of the cross-sectioned samples (Fig. 3.10k,l and Supplementary Movies 1-4[*]) and AFM (Fig. 3.10c-f, 3.38, 3.43 and 3.44). TEM tomography images confirmed the surface topography and interparticle distances obtained from AFM and SAXS, respectively.

The S-like chains in LH and RH samples are chiral, as they cannot be superposed owing to the out-of-plane component (height; Fig. 3.10). Note that some of these chains might have also formed spontaneously during LBL deposition (Fig. 3.41f) but they were reorganized during the substrate release from the twisted to the planar state. Maps of LD orientation helped us to quantitatively understand directions of NP chains (Fig. 3.10g-j), and these precisely matched with patterns observed from magnified AFM images (Fig. 3.10c-f). For complementary optical mapping information for single-sided samples, see Fig. 3.42. One could note that NP islands on the cracked side are also made from such chains (Fig 3.42). However, they had a flattened geometry predominantly confined to the *x-y* plane of the film, thus excluding chiral conformations and CD_{NP}, being responsible, however, for CE_{linear}. The geometry of NP chains

can be described in terms of a chirality factor, *F*, representing deviation from the linear (achiral) approximant in three dimensions (Eq. 3.7 and Fig. 3.47). For NP chains on the buckled side, ε = 0%, the *F*-factors were 1.4 (LH) and 2.6 (RH). A parallel can be made between the chirality factor *F* and so-called Guye's asymmetry products used in organic chemistry, which are known to correlate with molecular optical activity. Stretching of samples along the *y* axis was accompanied by compression along the *x* axis and protrusion along the *z* axis due to a high Poisson's ratio of PDMS along the *x* axis. Accordingly, the length of the NP chains decreased but their height and width increased (Fig. 3.45). In other words, the NP chains became curvier in the *x*-*y* plane and more protruded in the *z* direction. Not only did such geometrical transformation lead to stronger coupling with circularly polarized photons, but it also increased chain chirality. The chirality *F*-factor for the buckled side increased to 5.9 (LH) and 8.7 (RH) at ε = 25%, and further increased to 7.1 (RH), and 9.2 (RH) at ε = 50% (Fig. 3.47).

3.5.3 Computational Simulations

Computational simulations of chiroptical properties based on numerical solutions of the Maxwell equation using the finite element method confirmed that these transformed chains must reveal increased optical activity (Fig. 3.11 and a section of 3.9.14). For buckled sides, a single S-like shaped chain and an array of five chains were used to simulate their chiroplasmonic properties (Fig. 3.11a-d and 3.49) with geometries obtained from AFM images (Fig. 3.38, 3.43 and 3.44), SAXS data (Fig. 3.40) and TEM images (Fig. 3.41). The simulated spectrum from the single chain of LH, ε = 0%, yielded a sigmoidal chiroptical spectrum with negative and positive peaks at 550 and 575 nm, respectively (Fig. 3.11e). The NP chains

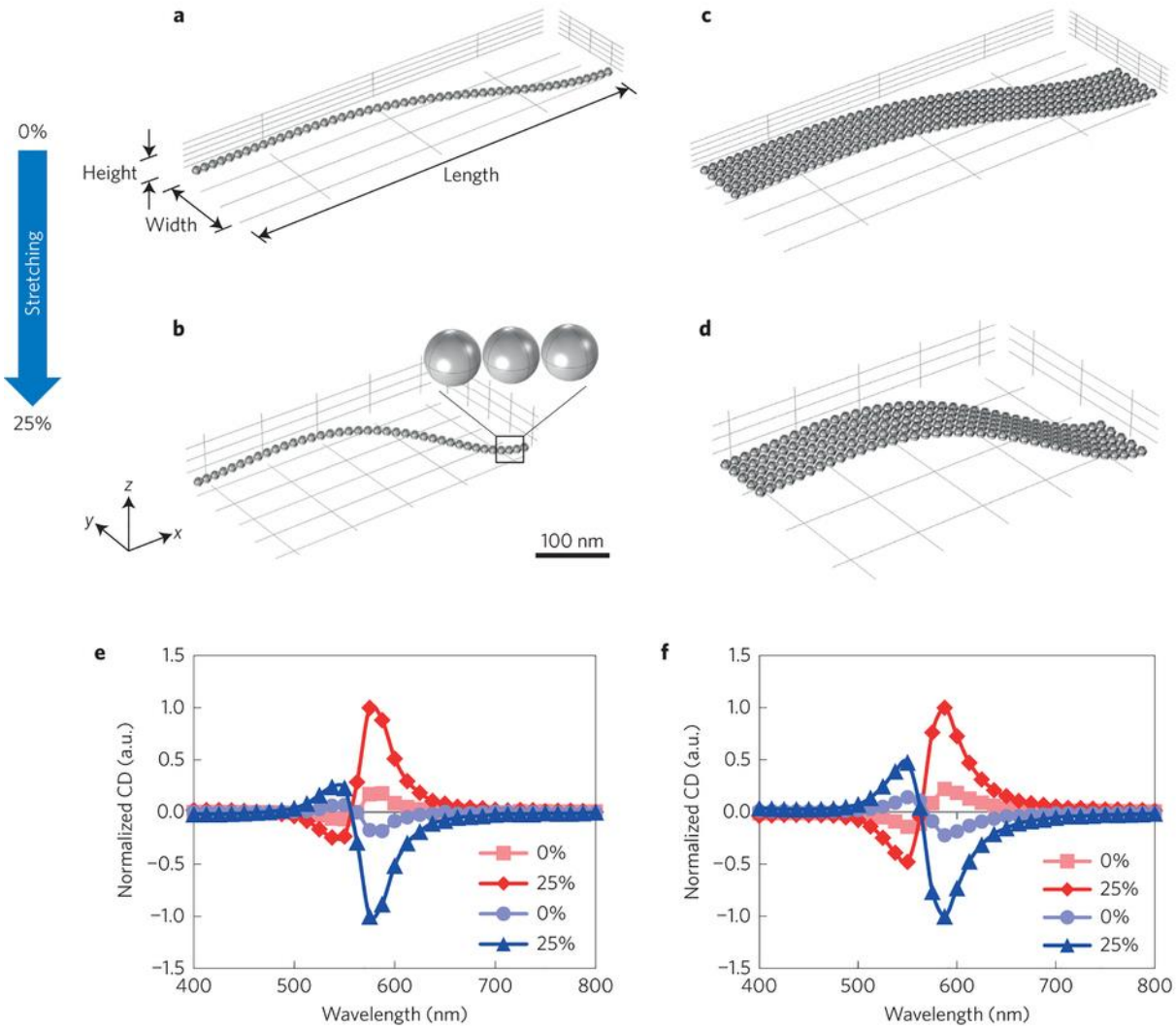

Figure 3.11. Simulated chiroptical properties of S-like Au NP chains. a–**d**, LH NP chain models used in computational simulations for buckled sides with characteristic dimensions. Single chains with ε = 0% and 25% are shown in **a** and **b**, respectively. Arrays of five chains with ε = 0% and 25% are shown in **c** and **d**, respectively. Five chains are arrayed with a gap of 20 nm in the *y* direction. Models of opposite handedness can be found in Fig. 3.49. Scale for images **a**–**d** is given in **b**. **e**,**f**, Calculated CD spectra from a single chain (**e**) and an array of five chains (**f**). Red colors signify LH samples and blue colors signify RH samples.

observed in RH samples revealed calculated spectra that mirrored those of LH samples. Overall, the simulated spectra of the buckled side closely matched the experimental data (Fig. 3.10b). When the strain increased to 25%, calculated chiroptical peaks at positive maximum

also increased their intensity by 5.5- fold. Shape, spectral position and growth of calculated peaks with strain increase were similar to the increase of CD_{NP} shown in the experimental data (Fig. 3.10b). Simulated *g*-factors showed comparable magnitude and shape of spectra to those found in the experiment (Supplementary Fig. 3.48). The differences between simulated and experimental spectra, for example the differences in the spectral width of CD peaks, are to be attributed to the diversity of NP arrangements in the experimental films. In addition, simulated results from an array of five S-like chains showed a similar pattern of CD spectra to the single chain even with the larger contribution of scattering (Fig. 3.11 and 3.50).

3.5.4 Non-Superimposable Chains

The terms chiral and chirality were introduced by Lord Kelvin (Lord Kelvin, Robert Boyle Lecture at the Oxford University (1893)): "I call any geometrical figure, or group of points, chiral, and say that it has chirality if its image in a plane mirror, ideally realized, cannot be brought to coincide with itself." Following the definition above, chirality is understood if a geometry cannot be mapped to its mirror image by rotations and translations alone. Simply, a geometry is chiral when it cannot be superimposed with its mirror symmetric image.

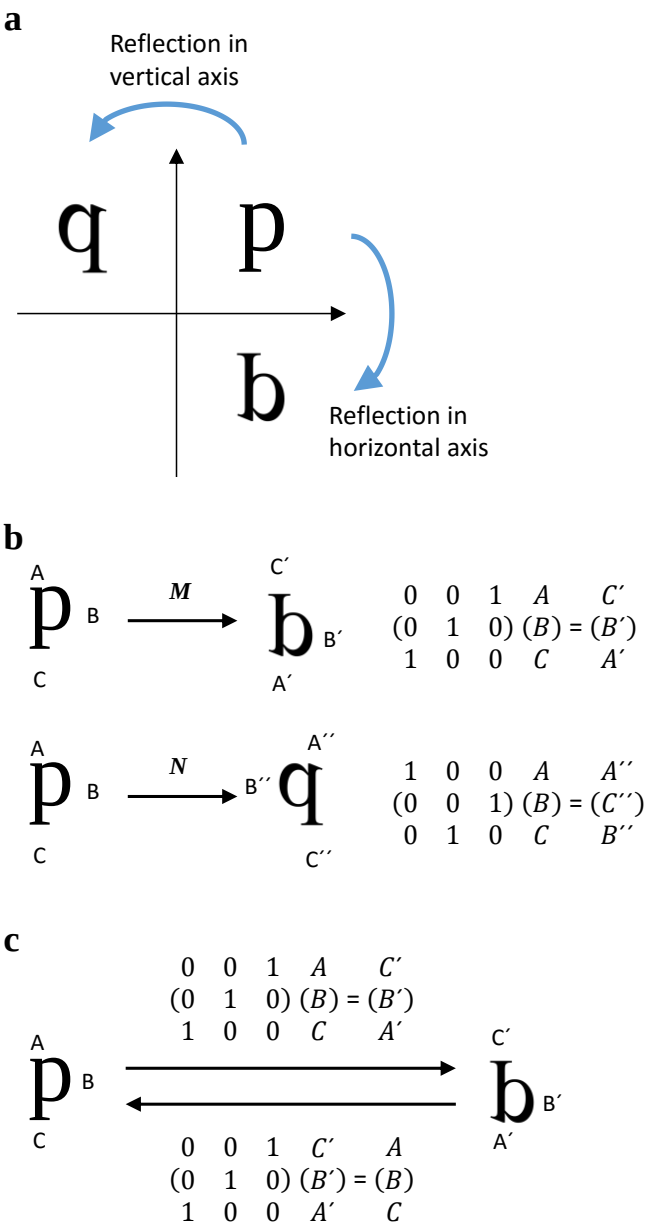

Figure 3.12. a, **p** as an original image and **b** and **q** as horizontal and vertical reflection images. **b**, Transformation matrices for horizontal and vertical reflections. **c**, Consecutive applications of horizontal reflections to **p**.

However, from the perspective of "mathematical matrix", a one-handed object in a Euclidean space can be obtained by applying a transformation matrix, such as reflection about an axis (or a line), from the other side. In this regard, reflected entities can be seen as the same.

Here we have a simple 2D case (Fig. 3.12). **b** and **q** are reflected images of **p**. The letter **p** can be characterized by a configuration of A, B and C in a column matrix. The transformation operation can be represented as a (3x3) matrix[135]. The reason reflected images can be regarded as the same can be that "a reflection is an involution". When the same tensor transformation is applied twice, every element of the geometry will be brought back to its original position: $M(M(x)) = x$, for all x in the domain of M (Fig. 3.12c). With this perspective, **p** and **b** can be recognized as interchangeable. This may be why the view point of the observer is important[136]. However, in a Cartesian vector space, that does not mean each component in **p** is same as each in **b**: $x \neq M(x)$, for all x in the domain of M. Therefore, **p** is different from **b** even after applications of translation or rotation. They cannot be superposed. All these properties can be logically extended to chiral geometries in a 3D coordinate system, and essentially the same results will be obtained.

NP chain models with handedness obtained from AFM measurements of sample were compared if they are non-superimposable. A RH chain was obtained from LH chain using "mirror transformation" function in COMSOL software over a mirror plane of x-z plane to be placed on the same coordinate system (Fig. 3.13b). Then the RH chain was further rotated and translated to overlap starting and ending particle positions with the LH chain (Fig. 3.13c,d). Mirror plane was inserted between two entities for comparison of geometries (Fig. 3.13e-g). However, chains cannot be superposed and significant gaps between the two were observed. Circular dichroism COMSOL simulation results using each model show distinctively opposite responses (Fig. 3.11). Therefore, LH and RH chains are different because they cannot be superimposed.

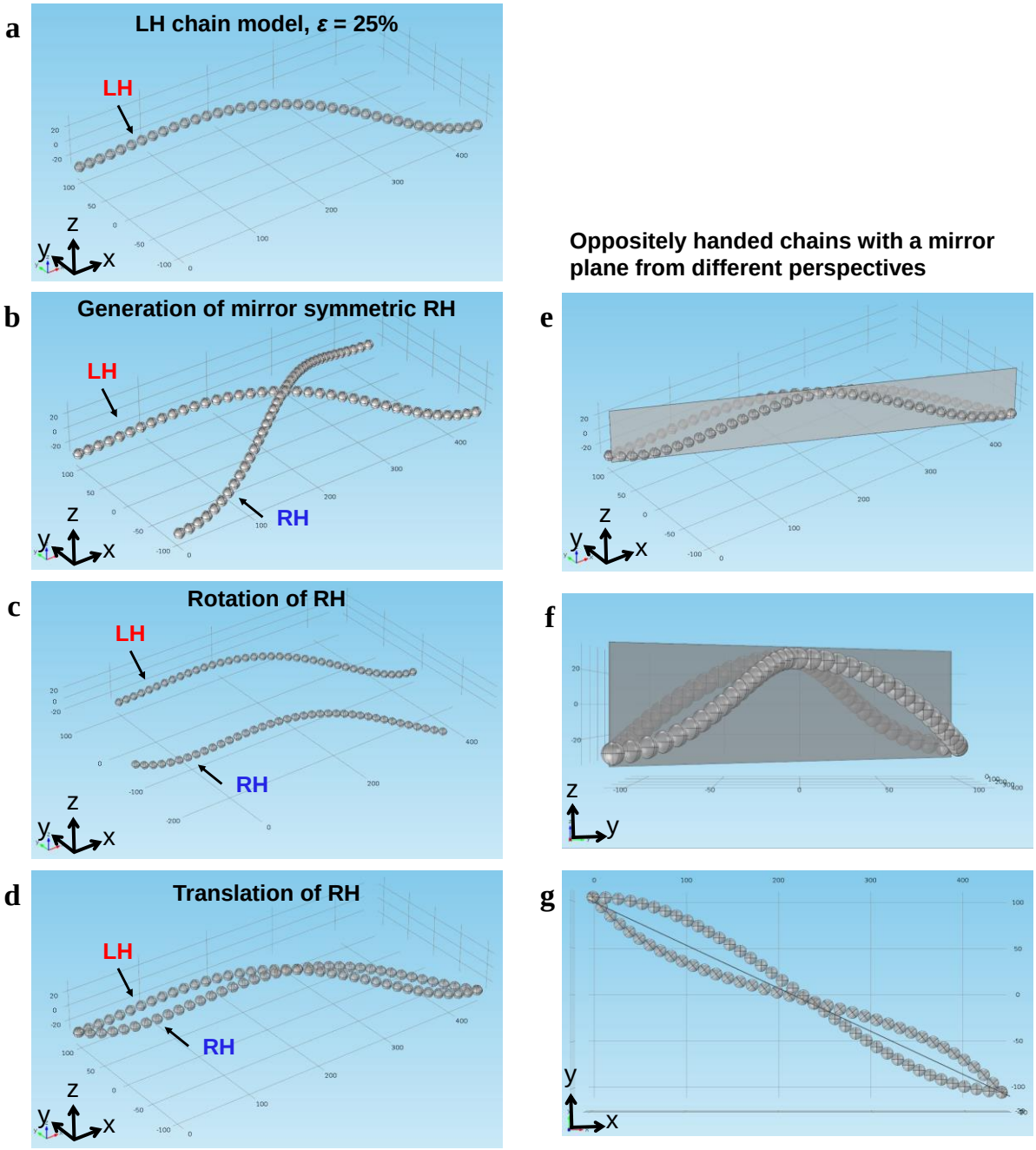

Figure 3.13. a, Chain model for LH, ε = 25%. **b-d**, RH chain model was generated by mirror transformation function and then further rotated and translated. **e-g**, Oppositely handed chains with a mirror plane were viewed from different perspectives.

Non-superimposable NP chains can also be addressed by comparing von Mises stress distribution of "torsion + no displacement" PDMS and surface vectors from initial plane geometry of both left-handed and right-handed cases (Fig. 14). Stress distribution and arrow vectors in LH and RH strips are mirror symmetric and cannot be superimposable, though mathematically one handedness can be generated from the other side.

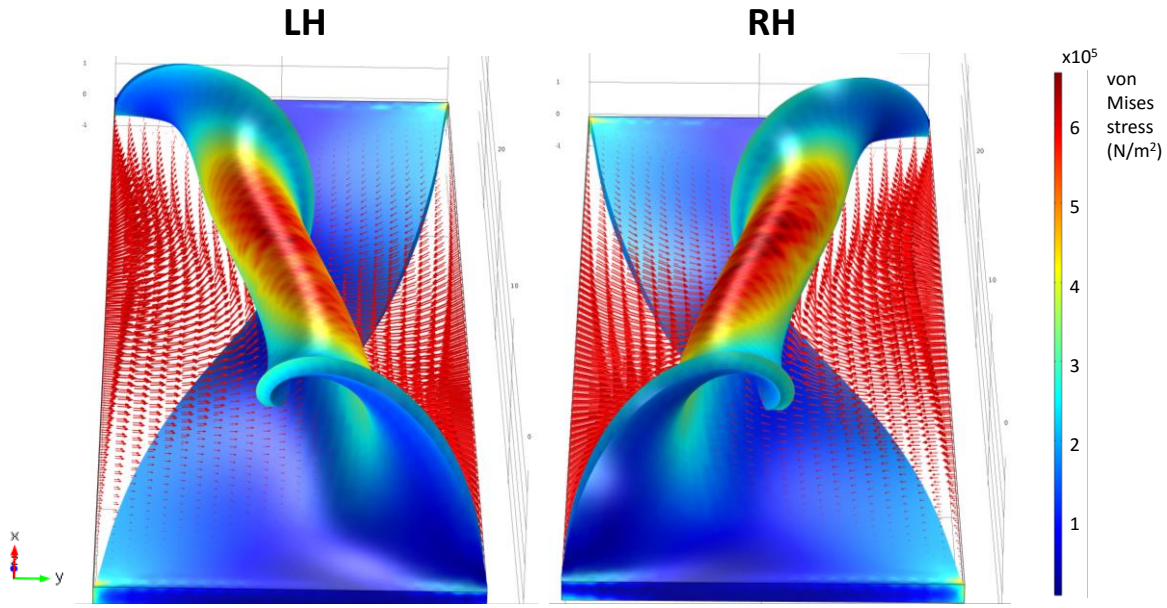

Figure 3.14. "Torsion and no displacement" applied LH and RH PDMS strips. von Mises stress distribution is expressed by color scale and relative vector from each mesh node is expressed by arrow.

3.6 Generality of the Macro-to-Nano Chirality Transfer Method

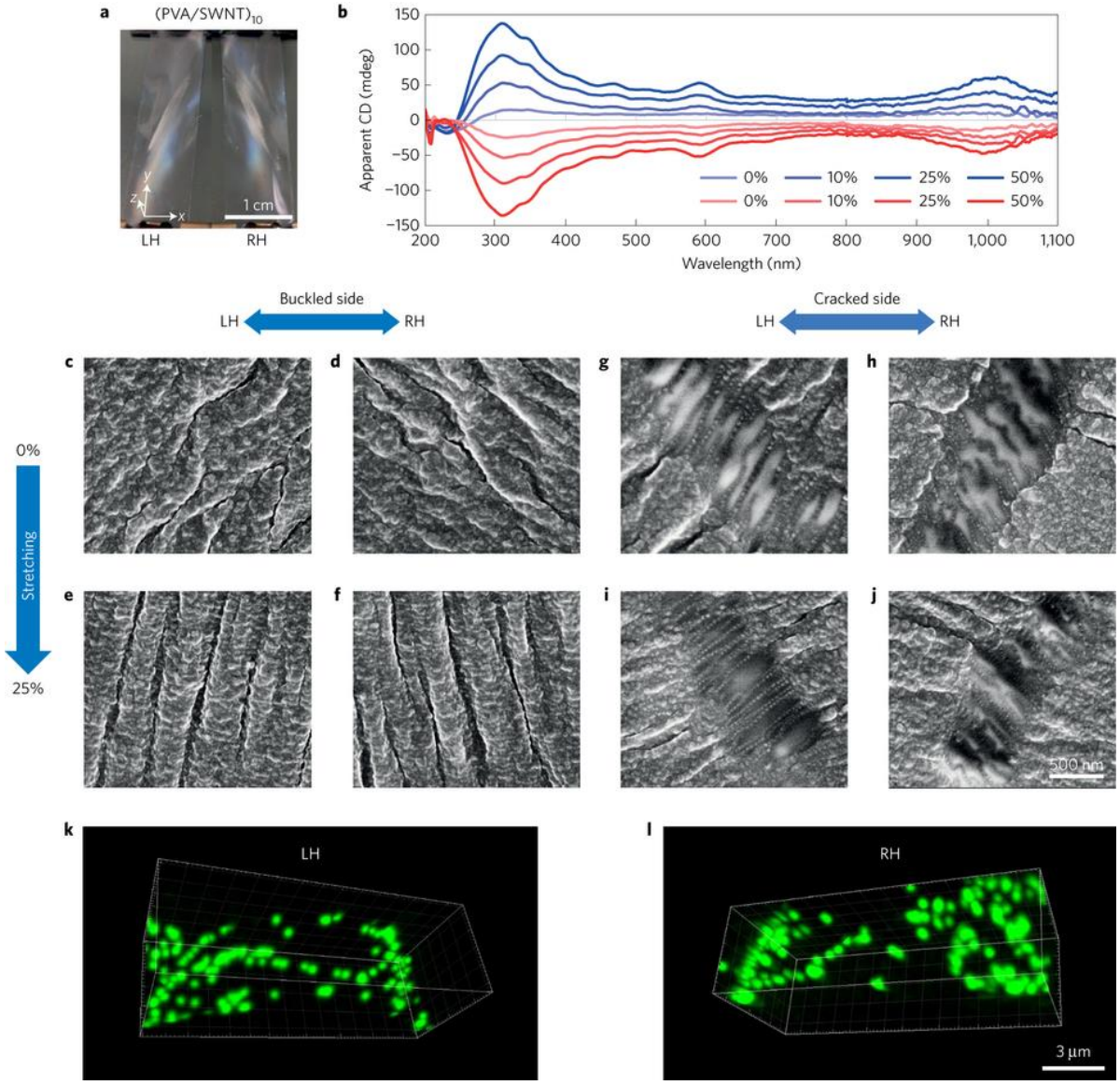

Figure 3.15. Strain-modulated chiroptical multilayers from semiconducting nanotubes. a, Optical images of $(PVA/SWNT)_{10}$ nanocomposites from LH (left) and RH (right). **b**, Apparent CD spectra of double-sided LH and RH samples under ε = 0, 10, 25 and 50%. Apparent CD spectra were measured from JASCO J-815. **c**–**j**, Scanning electron micrographs of buckled and cracked sides of LH and RH samples under ε = 0 and 25%. Scale for images **c**–**j** is given in **j**. **k**,**l**, STED microscopy images of $(PVA/SWNT)_{10}(Nano\ Beads)_1$ for buckled sides of LH and RH, respectively. See Supplementary Movie 5 for full 3D rendering.* Scale for images **k**,**l** is given in **l**.

The chirality transfer based on asymmetric macroscale strains should not be specific to Au NPs—the technique is potentially applicable to films from a variety of nanoscale components. As such, we implemented the same process for purified (6,5) SWNTs, with a median diameter of 0.78 nm, LBL-assembled with poly(vinyl alcohol) (PVA) (Fig. 3.15a and 3.26). Our special interest in adding nanotubes to the toolbox of chiroptical materials is justified by their significance to a variety of composite-based devices. LH and RH samples consisting of $(PVA/SWNT)_{10}$ layers showed mirror-symmetrical CD spectra from 200 nm to 1,100 nm, representing multiple absorption peaks of (6,5) SWNTs (Fig. 3.23b, 3.26c,d and 3.28a). The intensity of the chiroptical bands reversibly increased by more than one order of magnitude following stretching to 50% (Fig. 3.15b and 3.26). Apparent anisotropy *g*-factors for double-sided samples were as high as 0.007 at 1,000 nm and 0.012 at 350 nm for $\varepsilon = 50\%$. Scanning electron microscopy imaging of SWNT multilayer topography (Fig. 3.15c–j and 3.35) revealed 3D S-like shapes along buckles. These were similar to those found in NP films and had opposite mirror symmetry in LH and RH samples. Control experiments showed that the chiroptical activity originated solely from the macroscale twist experienced by the LBL films, rather than any intrinsic chirality of the nanotubes (Fig. 3.23). To further demonstrate the generality of the enantioselective manufacturing of nanocomposites and to obtain an additional visual representation of the 3D S-like shapes forming in the twist–deposit–release process, we added a layer of 100 nm fluorescent nanoscale beads (NanoBeads) on top of $(PVA/SWNT)_{10}$. Super-resolution stimulated emission depletion (STED) microscopy unequivocally demonstrated that the nanoscale beads are aligned in S-chains on the full wavelength of buckles (Fig. 3.15k,l and Supplementary Movie 5*). Note that the macro-to-nano chirality transfer

may not be applicable to thin films made from dyes and other molecular scale materials due to the difference in deformation and assembly patterns compared with nanoscale materials.

3.7 Conclusion and Outlook

Macroscopic gradients of biaxial strain fields stereoselectively convert achiral and *x-y* isotropic composite films into chiral material with nanoscale topography. The out-of-plane component of 3D nanoscale assemblies can be reversibly enlarged by elastic deformations, which markedly enhance the polarization rotation of transmitted photons. Macro-to-nano chirality transfer demonstrated for NPs, nanobeads and SWNTs can be extended to other nanoscale components. This new family of composites enable one to combine mechanical, plasmonic and excitonic properties of various nanoscale 'building blocks' with manufacturability, scalability and uniformity of hybrid organic-inorganic materials made by LBL assembly[12]. Real-time modulation of the polarization rotation over thousands of cycles (Fig. 3.27 and 3.28b) originating from strain dependence of chiral geometries and dihedral angles between LD/LB principal axes and the possibility of integrating semiconductor nanomaterials with solid-state optics, each contribute to a plethora of creative engineering opportunities in the areas of information, optoelectronic[64] and optomechanical devices.

3.8 Materials and Methods

Preparation of substrates. PDMS (Dow Corning Sylgard 184; ratio of base to cross-linker, 10:1 by mass) was poured, mixed and degassed in a petri dish. Curing in an oven at 70

˚C over 6 h produced PDMS membranes that were 0.5 mm thick. These were then cut into strips of 10 mm (width) x 45 mm (length) x 0.5 mm (thickness) as shown in Fig. 3.1a.

Preparation of PU, Au NPs, PVA and SWNTs. As-received cationic polyurethane aqueous dispersion (30 vol%, MW ≈ 92,000, Hepce Chem Co., South Korea) was used after diluting to 1 vol% solutions with deionized (DI) water. Gold(III) chloride trihydrate and sodium citrate tribasic dihydrate (both from Sigma-Aldrich, USA) were used as received. Citrate-stabilized AuNPs with a diameter of 13.0 ± 0.3 nm were synthesized as described elsewhere[55]. As-received polyvinyl alcohol (MW ≈ 13,000 - 23,000, Sigma-Aldrich, USA) was used after diluting to 0.2 vol% solutions with DI water. Single-walled carbon nanotubes, (6,5) chirality ≥ 95%, and sodium dodecylbenzene sulfonate (both from Sigma-Aldrich, USA) were used as received. To the dispersion of 0.2 mg/mL SWNTs, sodium dodecylbenzene sulfonate was added (nanotube-to-surfactant ratio was 1:25 by weight), followed by tip-sonication for 1 h (5 sec for each pulse on and off with 40% amplitude). The as-prepared dispersion was then centrifuged using a Sorvall LegendMach 1.6R centrifuge (Thermo Scientific, USA) at 10,000 r.p.m. for 1 h to separate any larger aggregates.

Preparation of chiroptical composite films. Strips of PDMS were twisted in clockwise and counterclockwise directions along the *y*-axis by an angle, ω, equal to 360˚ and fixed using clamps for LH and RH substrates, respectively (Fig. 3.1b). Next, the surfaces of PDMS were activated for 30 min by a UV ozone cleaner (model no. 342, Jelight Company) to modify the hydrophobic surface of PDMS with hydrophilic functionalities. Note that this step produces ozone, therefore good ventilation is required. Activated and pre-twisted PDMS strips were dipped into a 1 vol% aqueous solution of positively-charged PU for 5 min, rinsed

with DI water for 1 min and gently dried with compressed air. Then they were dipped into a dispersion of negatively-charged Au NPs for 20 min, rinsed for 1 min and again dried with compressed air. Five bilayers were sequentially deposited (Fig. 3.1c) to have a thickness of 40 nm on a silicon wafer by ellipsometry (Fig. 3.36a). Electrostatic attraction was found to be a reasonable driving force for deposition. This one cycle of deposition constitutes one bilayer of PU/NP. For measurements of chiroptical properties, samples were released and allowed to flatten (Fig. 3.1d). Single-sided samples were prepared by detachment of one side using adhesive tape. For preparation of $(PVA/SWNT)_{10}$, a nearly identical procedure was used except with different lengths of dipping time: 5 min into 0.2 vol% PVA solution and 5 min into a SWNT dispersion. The sequential deposition of 10 bilayers onto a silicon wafer resulted in a thickness of 18 nm by ellipsometry (Fig. 3.36b).

Preparation of samples for STED imaging. As-prepared $(PVA/SWNT)_{10}$, in twisted state, was further dipped into a 0.1 vol% solution of fluorescence beads (FluoSpheres® Carboxylate-Modified Microspheres, 100 nm, (505/515), Life Technologies) for 20 min, rinsed with DI water for 1 min and gently dried with compressed air, followed by flattening, $(PVA/SWNT)_{10}(Bead)_1$. Fluorescent labeled chiroptical nanocomposite was mounted on a glass slide with mounting media (ProLong® Diamond Antifade Mountant, Life Technologies) on which a cover slip with refractive index of 1.5 was placed.

Characterization. Transmission electron microscopy (TEM) images were obtained with a JEOL 2010F analytical electron microscope. Absorbance measurements in UV-Vis-NIR were performed on BioMate™ 3S Spectrophotometer (Thermo Scientific). Thickness of the initial assembly of the LBL film was calculated using a BASE-160 spectroscopic

ellipsometer (J. A. Woollam) and a multi-wavelength-imaging null-ellipsometer (EP3 Nanofilm). LBL film for ellipsometry was prepared on silicon wafers following the same procedure as described for the LBL film. Weight growth of films was investigated by a quartz crystal microbalance (QCM) 200 from Stanford Research Systems with 5 MHz quartz crystals. Circular dichroism (CD) spectra were obtained using a Mueller matrix polarimeter[130] and a Jasco J-815 CD spectrometer. Otherwise mentioned, optical responses were measured at the center of the films. Atomic force microscope (AFM) images were obtained by Bruker Dimension Icon AFM and multimode AFM with ScanAsyst mode. X-ray scattering data were obtained with a Bruker NanoStar Small-Angle X-ray Scattering System equipped with a Siemens Kristalloflex 770 X-Ray Generator, and a Cu K_α radiation (0.1542 nm) X-ray tube with peak power of 1.5 kW on a Hi Star Area 2D detector with 1 min of exposure time. Super-resolution confocal images were acquired using a Leica SP8 multi-fluorescent confocal microscope equipped with a white light laser combined with 592 depletion laser utilizing STED applications. Tilt-series BF-TEM (Bright field TEM) images were obtained from an aberration corrected energy filtering transmission electron microscope (Carl Zeiss, Libra 200 HT Mc C_s) operating at 200kV with an advanced tomography holder (E.A. Fischione Instruments, Model 2020).

3D TEM Tomography imaging. Epoxy cured and microtomed samples were placed on 200 mesh TEM grids (Ted Pella Inc.). All BF-TEM images were obtained with zero-loss filtering using in-column omega filter. Single-axis tilt-series of 62 and 69 BF-TEM images of two samples were acquired in range of -60˚ - +62˚ (buckled side, RH) and -66˚ - +70˚ (buckled side, LH) in tilt steps of 2˚. As fiducial markers for fine alignment, gold nanoparticles (5 nm)

were used. Full alignment of the tilt-series BF-TEM images (0.55 nm/pixel) were done by the commercial tomography reconstruction software package (JEOL, TEMography^{TM}) which can be applied the simple cross correlation technique. Based on the alignment of 2D projections, 3D tomographic reconstruction was carried out with the SIRT (simultaneous iterative reconstruction technique) using the same software[137].

Calculated CD spectra. Computations of CD spectra were performed using the wave-optics module embedded in the COMSOL Multiphysics module. The optical constants of gold were taken from elsewhere[138]. Simulated CD spectra were first calculated by subtracting the cross-section extinction of RH circularly polarized light (RCP) from that of LH circularly polarized light (LCP), and then the values were normalized to the maximum peak of the spectra. CD = extinction of LCP - extinction of RCP, where the extinction cross-section is the summation of the absorption cross-section and the scattering cross-section.

3.9 Supplementary Information

*Supplementary Movies 1-5 can be found at http://www.nature.com/nmat/journal/vaop/ncurrent/full/nmat4525.html#supplementary-information.

3.9.1 Methods for Parameters Calculations

1. PDMS is transparent enough to disregard dichroism in the wavelength ranges of interest, 200 – 800 nm (Fig. 3.16a).

2. LD of each NP layer was directly obtained from single-sided samples.
3. LB of each NP multilayer was obtained from measurement of single-sided samples after subtraction of LB contribution from the PDMS substrate. This was achieved plotting a polynomial fit of two far end regimes of wavelength and subtracting this contribution from measurements (Fig. 3.16c). LB of NP layers always have a peak at the plasmonic wavelength while LB of PDMS does not have any peaks in the wavelength ranges of interest.
4. LB of PDMS substrates were calculated from the polynomial fit results (Fig. 3.16c).
5. Magnitude of LD and LB were calculated from $\sqrt{LD^2 + LD'^2}$ and $\sqrt{LB^2 + LB'^2}$, respectively.
6. Angle of LD was obtained by using "*atan2*" function, such as $0.5 * \mathrm{ATAN2}(\mathrm{LD}, \mathrm{LD}')$. Because the *atan2* function can gather information of the signs of the input and will choose the proper quadrant of the computed angle, whereas simple "*atan*" function cannot.

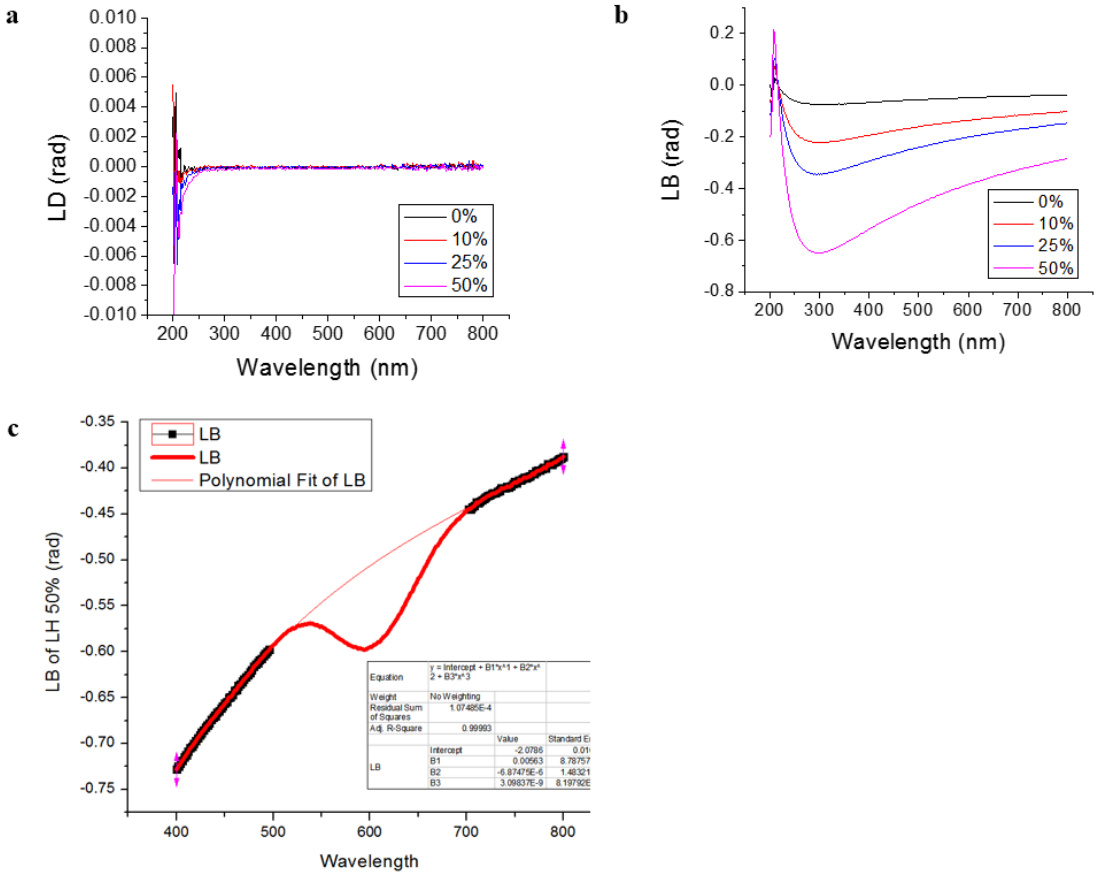

Figure 3.16. Optical activities of a PDMS substrate and buckled NP layer. a, LD of PDMS under ε = 0%, 10%, 25% and 50%. **b**, LB of PDMS under ε = 0%, 10%, 25% and 50%. **c**, LB of buckled side on PDMS, LH, under ε=50% and its polynomial fit of two far end regimes.

7. Calculated angles of LD and LB in the NP layers are same.

3.9.2 Comparison between Mueller Matrix Polarimeter and Commercial Instrument

CD spectra from most commercial equipment, including JASCO J-815, are based only on the M03 element of the Mueller matrix. Same measurements with sample being flipped by 180˚ along the *y*-axis will give M30 element. Comparing each M03 and M30 value from both pieces of equipment, polarimetry and JASCO J-815, will be interesting for us to see the difference and this will be very helpful for colleagues in the same field as well. M03 and M30

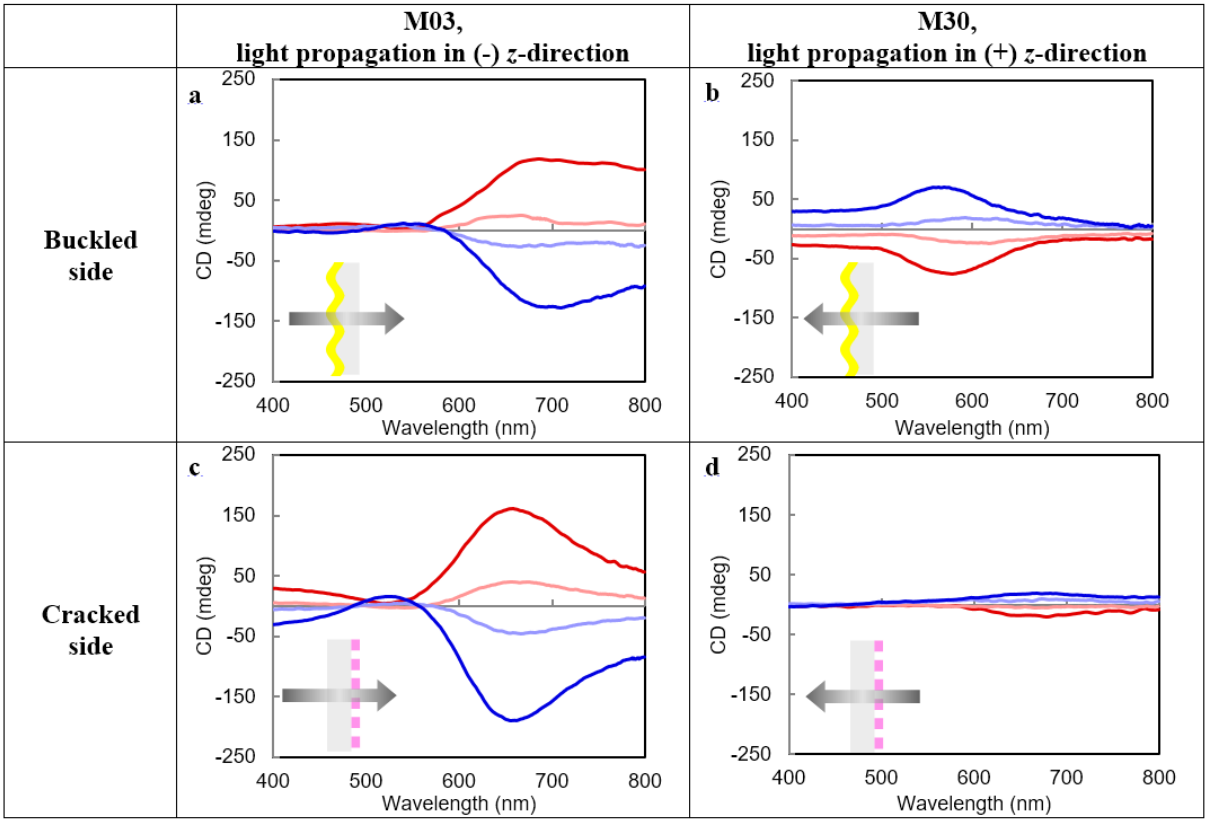

Figure 3.17. M03 and M30 elements from JASCO J-815. Spectra for LH and RH samples under ε = 0% and 50% for buckled side only (**a**, **b**) and cracked side only (**c**, **d**) on PDMS substrate. Light propagation in the negative and positive *z*-directions were tested by rotating samples by 180° around the *x*-axis. Insets: schematics of light propagation on samples.
M30 spectra of cracked side sample had very small intensities which corresponds well with the spectra from Mueller matrix polarimetry (Fig. 3.8d).

of single-sided samples from J-815 are not exactly same as those from Mueller matrix polarimetry. However, they are quite similar in terms of location of peaks and intensity increase upon stretching (Fig. 3.8, 3.17, and 3.18).

JASCO J-815 was also used for control experiments and CNT composites. Part of the

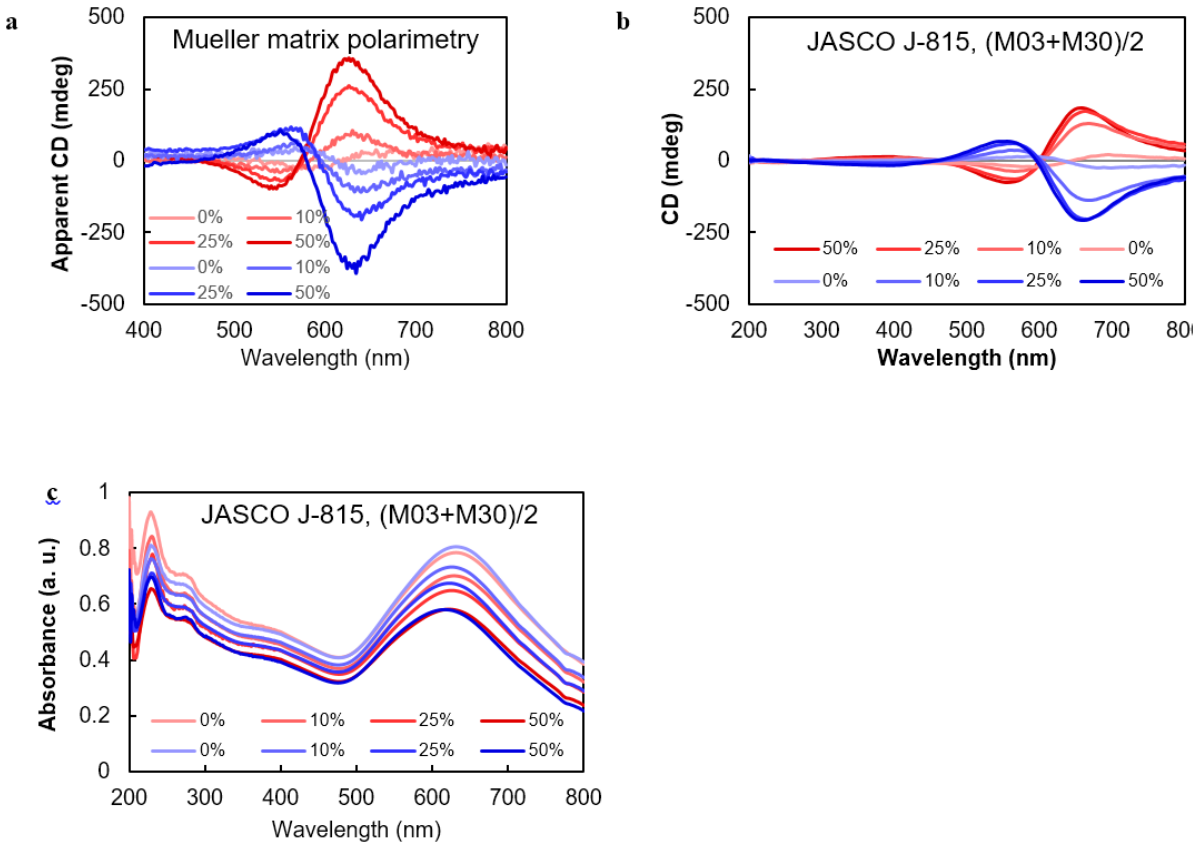

Figure 3.18. Comparison of apparent CD from Mueller matrix polarimetry and (M03+M30)/2 from JASCO J-815 of both side samples of $(PU/NP)_5$. a, Apparent CD spectra of $(PU/NP)_5$ from Mueller matrix polarimetry. **b**, (M03+M30)/2 CD spectra of $(PU/NP)_5$ from JASCO J-815. **c**, Corresponding absorbance spectra for **b**.

reason here is that our polarimetry device covered wavelength only up to 800 nm while CNT composites had chiroptical peaks in NIR. For double-sided CNT composites, (M03+M30)/2 was applied. Single spectra of either M03 or M30 for double-sided would contain artifacts or

multiple reflected light in between two NP layers. We would expect that the averaged should effectively calculate apparent CD[139–142]. Again, we still need to admit that this is not fully equivalent to the apparent CD provided by the Mueller matrix polarimetry. We include a comparison of (M03+M30)/2 of double-sided chiroptical nanocomposite samples, $(PU/NP)_5$, from polarimetry and J-815 (Fig. 3.18). Unless otherwise mentioned, CD spectra in this study were obtained from Mueller matrix polarimetry.

3.9.3 Differential Mueller Matrix for Calculation of CE_{linear}

Analysis of chiroptical activity by polar decomposition of distinct optical layers in stratified optical system should be the best way of recognizing CD_{NP}. We, however, still tried further to know if we can calculate amount of the contributions of CE_{linear}. Even though this has to be done with an assumption of optical "homogeneity" along the light path, calculations will expand our knowledge of optical properties and its prediction from matrix calculations.

Based on the Mueller matrix polarimetry measurement of single-sided samples, we were able to obtain optical properties of our samples, both circular (CD and CB) and linear (LD, LB, LD´ and LB´). With those real values, we were able to simulate differential Mueller Matrix corresponding to single-sided samples (i.e. single NP layer on a PDMS substrate). Then we compared the simulated values with experimentally obtained apparent CD.

For the clarity of codes, numbers of 1, 2 and 3 were assigned to each buckled, PDMS and cracked side, respectively. Thus, calculation for double-sided, buckled side only, and cracked side only were done with operations of J=J3.J2.J1, J=J2.J1 and J=J3.J2, respectively.

After analyzing components of differential Mueller matrix (L03) and comparing them to experimental values of apparent CD, we confirmed that chiroptical activity of buckled side has two principal contributions: chiral NP assemblies in buckled layer and combinatory effects of vectorial LD and LB. At the same time, chiroptical properties associated with cracked side arise primarily from the linear contributions. The rationales for the conclusion are:

1. Magnitude of simulated L03 components for two-layer system of buckled side on a PDMS substrate, were significantly lower than experimental CD from buckled side only samples (Fig. 3.19a).
2. Magnitude of simulated L03 components for two-layer system of cracked side on a PDMS substrate, were very closely matched with those from experimental apparent CD from cracked side only samples (Fig. 3.19b).

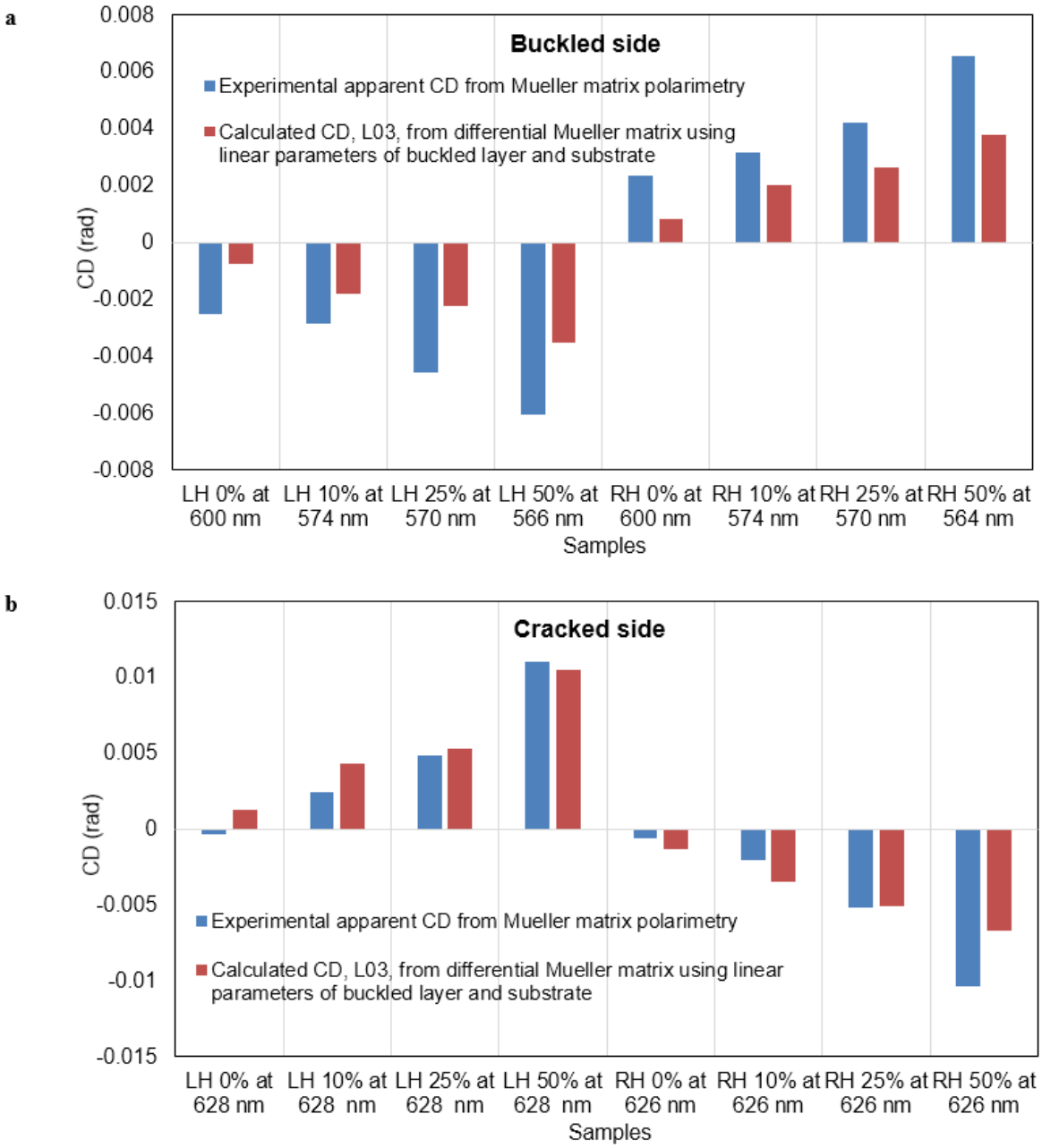

Figure 3.19. Comparison of Mueller matrix analysis between experimental and simulation. Apparent CD from experimental Mueller matrix polarimetry and simulated L03 component from differential Mueller matrix for two layer systems, buckled side only (**a**) and cracked side only (**b**) on PDMS substrate, were compared. Full simulation code and results of representative case (buckled side only, LH, ε = 0% at 600 nm) are in Note 3.1.

Note 3.1: Code and results for two layer system, buckled side only, LH, ε=0% at 600 nm

```
LD1m=0.0531994; (*Magnitude of LD of buckled layer*)
LB1m=0.010921392; (*Magnitude of LB of buckled layer*)
a1=-1.256170154; (*Calculated angle of LD in buckled layer. This is also used for angle of LB.*)
LD1=LD1m Cos[2 a1]; (*LD in buckled layer*)
LDp1=LD1m Sin[2 a1]; (*LD´ in buckled layer*)
LB1=LB1m Cos[2 a1]; (*LB in buckled layer*)
LBp1=LB1m Sin[2 a1]; (*LB´ in buckled layer*)
N1=(1/2) {{-LD1-I LB1,-LDp1-I LBp1},{-LDp1-I LBp1,LD1+I LB1}}; (*Calculation of differential Jones matrix for buckled layer, N1*)
J1=MatrixExp[N1]; (*Calculation of Jones matrix for buckled layer, J1*)
LB2=-0.0485; (*LB in PDMS. LB´ was nearly zero because the samples were stretched along the vertical direction. LD of PDMS is also zero in the wavelength range of interest. It is reasonable to disregard LB´ and LD in PDMS.*)
N2=(1/2) {{-I LB2,0},{0,I LB2}};(*Calculation of differential Jones matrix for PDMS layer, N2*)
J2=MatrixExp[N2]; (*Calculation of Jones matrix for PDMS layer, J2*)
J=J2.J1;
A={{1,0,0,1},{1,0,0,-1},{0,1,1,0},{0,I,-I,0}};
M=A.KroneckerProduct[J,Conjugate[J]].Inverse[A]; (*Conversion of Jones matrix to Mueller matrix, M*)
L=Chop[MatrixLog[M]]//MatrixForm (*Conversion of Mueller matrix to differential Mueller matrix, L*)
({
   {0, 0.0430084, 0.0313061, -0.000759322},
   {0.0430084, 0, -0.000155745, -0.00642121},
   {0.0313061, 0.000155745, 0, 0.0573334},
   {-0.000759322, 0.00642121, -0.0573334, 0}
  })
```

Overall, all the simulation data for single-sided cases are reasonably accurate. Logically we expanded the calculations for double-sided cases (three layers). However, simulations for three layer systems were less accurate and less valid. Simply due to optical parameters for each buckled and cracked layers (in the same sample) were obtained separately from two different single-sided samples. Consequently the values of LD and LB for every participating layer are not known with precision as in the case of single-sided samples, and these indeterminations can generate important errors in the final results. Additionally, buckled and cracked layers have both substantial reflectance, so multiple reflections through the PDMS substrate are possible and these are not taken into account in the simulations. However, we still compared CD values for the three layer systems (Fig. 3.20).

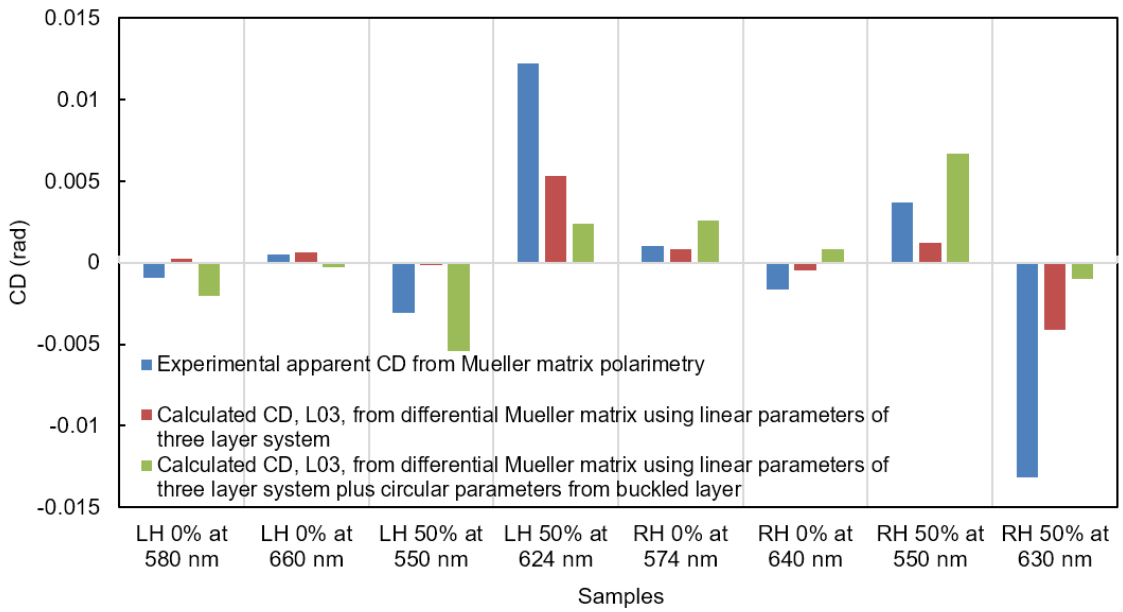

Figure 3.20. Comparison of Mueller matrix analysis between experimental and simulation for double-sided samples.
Full simulation code and results of representative case (double-sided, LH, ε=0% at 580 nm with incorporated parameters of linear from both buckled and cracked layer plus circular from buckled layer) are in Note 3.2.

Note 3.2: Code and results for three layer system, double-sided, LH, ε=0% at 580 nm, with incorporated parameters of linear from both buckled and cracked layers plus circular from buckled layer

```
LD1m=0.049296105; (*Magnitude of LD of buckled layer*)
LB1m=0.025488683; (*Magnitude of LB of buckled layer*)
a1=-1.261827079; (*Calculated angle of LD in buckled layer. This is also used for angle of LB.*)
LD1=LD1m Cos[2 a1]; (*LD in buckled layer*)
LDp1=LD1m Sin[2 a1]; (*LD´ in buckled layer*)
LB1=LB1m Cos[2 a1]; (*LB in buckled layer*)
LBp1=LB1m Sin[2 a1]; (*LB´ in buckled layer*)
CD1=-0.00229; (*CD in buckled layer*)
CB1=0.00019217; (*CB in buckled layer*)
N1 = (1/2) {{-LD1 - I LB1, -LDp1 - I LBp1 + CB1 - I CD1}, {-LDp1 - I LBp1 - CB1 + I CD1, LD1 + I LB1}}; (*Calculation of differential Jones matrix for buckled layer, N1*)
J1=MatrixExp[N1]; (*Calculation of Jones matrix for buckled layer, J1*)
LB2=-0.04891; (*LB in PDMS. LB´ was nearly zero because the samples were stretched along the vertical direction. LD of PDMS is also zero in the wavelength range of interest. It is reasonable to disregard LB´ and LD in PDMS.*)
N2=(1/2) {{-I LB2,0},{0,I LB2}}; (*Calculation of differential Jones matrix for PDMS layer, N2*)
J2=MatrixExp[N2]; (*Calculation of Jones matrix for PDMS layer, J2*)
LD3m=0.02950363; (*Magnitude of LD of cracked layer*)
LB3m=0.053419683; (*Magnitude of LB of cracked layer*)
a3=-1.139472338; (*Calculated angle of LD in cracked layer. This is also used for angle of LB.*)
LD3=LD3m Cos[2 a3]; (*LD in cracked layer*)
LDp3=LD3m Sin[2 a3]; (*LD´ in cracked layer*)
LB3=LB3m Cos[2 a3]; (*LB in cracked layer*)
LBp3=LB3m Sin[2 a3]; (*LB´ in cracked layer*)
```

```
N3=(1/2) {{-LD3-I LB3,-LDp3-I LBp3},{-LDp3-I LBp3,LD3+I LB3}}; (*Calculation of differential Jones matrix for cracked layer, N3*)
J3=MatrixExp[N3]; (*Calculation of Jones matrix for cracked layer, J3*)
J=J3.J2.J1;
A={{1,0,0,1},{1,0,0,-1},{0,1,1,0},{0,I,-I,0}};
M=A.KroneckerProduct[J,Conjugate[J]].Inverse[A]; (*Conversion of Jones matrix to Mueller matrix, M*)
L=Chop[MatrixLog[M]]//MatrixForm (*Conversion of Mueller matrix to differential Mueller matrix, L*)
({
   {0, 0.059426, 0.0508506, -0.00202861},
   {0.059426, 0, 0.000812155, -0.0553647},
   {0.0508506, -0.000812155, 0, 0.104398},
   {-0.00202861, 0.0553647, -0.104398, 0}
  })
```

3.9.4 Strong Polarization Rotation from CE_{linear}

Here we demonstrate that very strong polarization rotation in LBL films can originate from CE_{linear} by controlling angle between samples by rotation, and magnitude of linear parameters by stretching. We observed that measured rotatory optical activity was fluctuating by increasing the angle of rotation (Fig. 3.21). Maximum of ca. 1500 mdeg was obtained at certain angle with increased LB in polymeric substrate, ε = 50%. The other interesting observation here is the change of lobe patterns before and after stretching. The reason can be attributed as follows: before stretching, LD orientation of layers should have ca. 90˚ phase difference but they were synchronized after stretching.

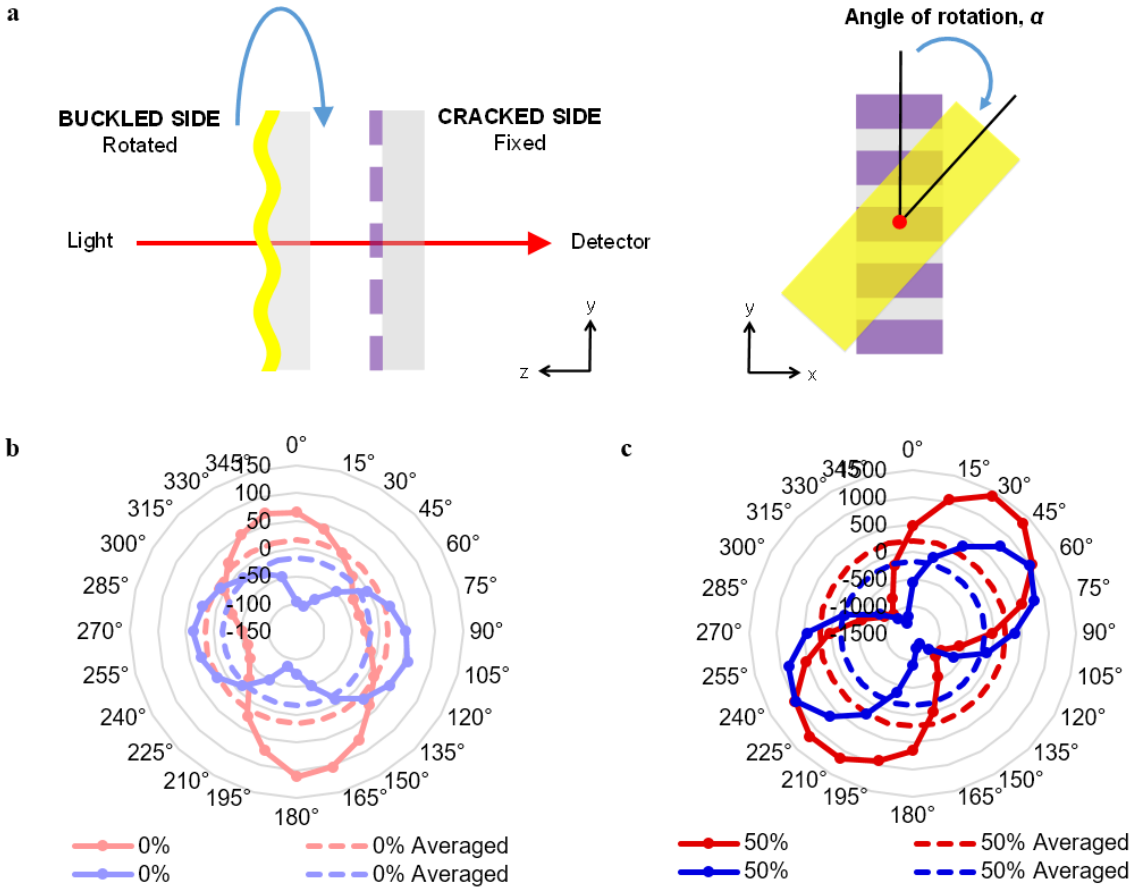

Figure 3.21. Linear optical anisotropy in stratified optical media made from buckled and cracked NP layers on PDMS. a, Schematics of the experimental setup. **b**, **c**, Apparent CD (mdeg, in vertical axis) obtained by rotating a buckled layer superposed on top of a fixed cracked layer under strains of 0% and 50%, respectively. Data under strains of 0% and 50% obtained at 650 nm and 628 nm, respectively, which were resonant wavelengths for cracked layers. Radial axis is for angle of rotation as described in **a**.

3.9.5 Control Experiments

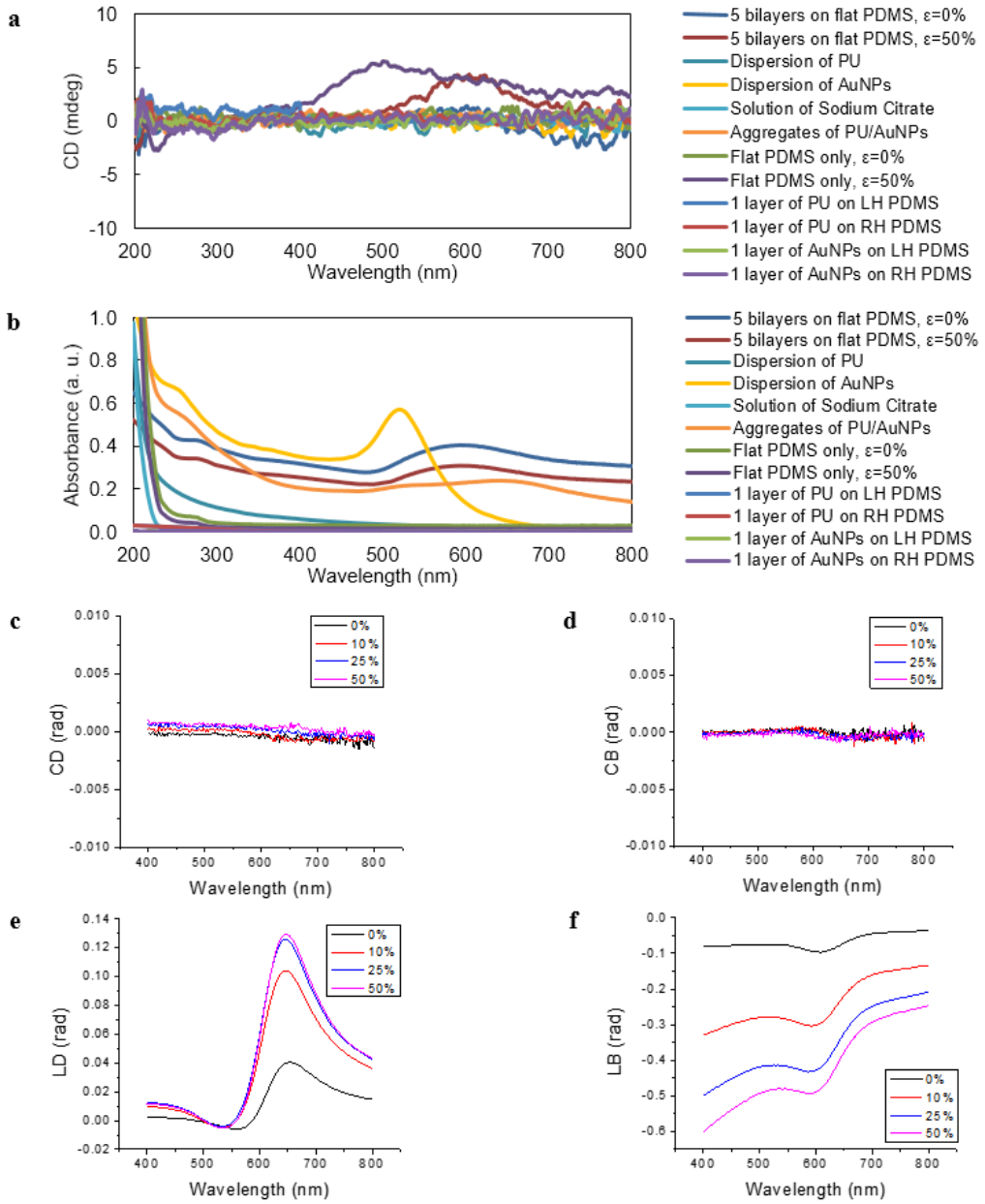

Figure 3.22. Control experiments on Au composite. a, CD spectra of various control samples for Au NP composite. **b**, Corresponding absorbance spectra for samples in **a**. For **a**,**b**, M03 and (M03+M30)/2 were measured on JASCO J-815 for solution and film samples, respectively. **c**-**f**, Apparent CD, CB, LD and LB of five bilayer deposited on flat PDMS under ε = 0% to 50% by Mueller matrix polarimetry, respectively. A dispersion of Au NPs with a peak absorbance of 0.63 had nearly zero CD activity; and all other control experiments displayed very small CD activity under strains in entire available range of wavelengths.

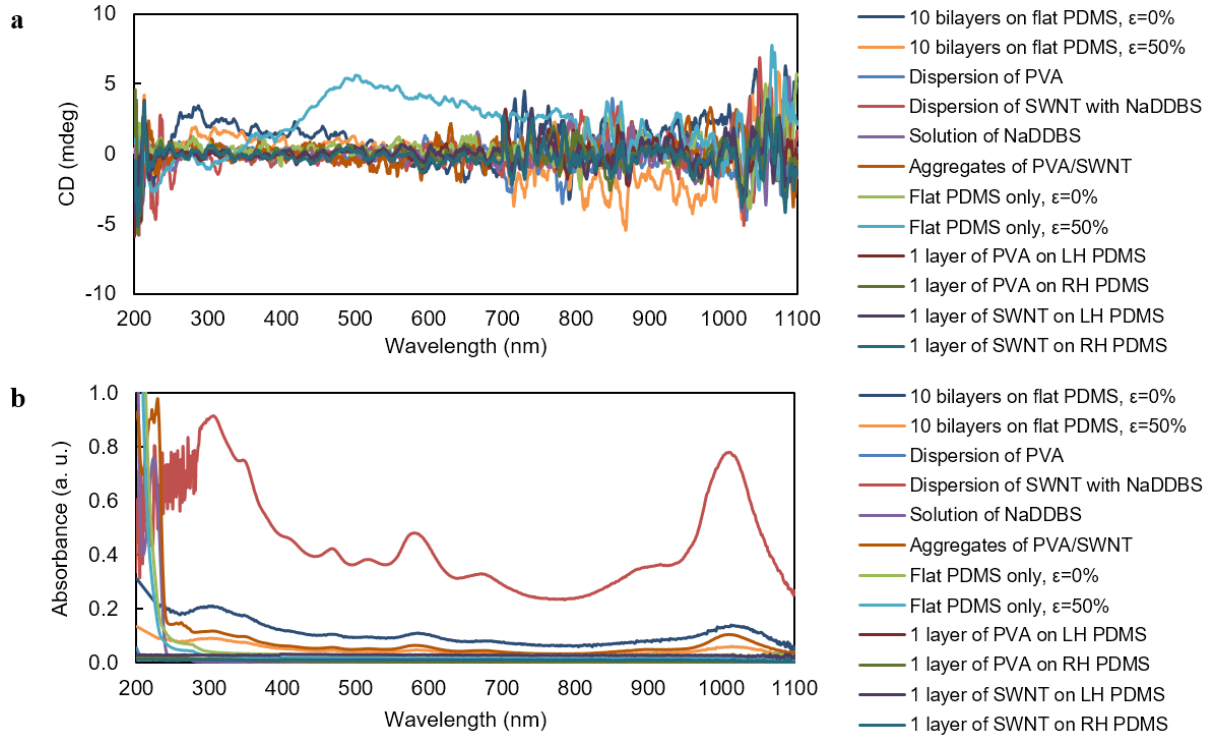

Figure 3.23. Control experiments on CNT composites. a, CD spectra of various control samples. **b**, Corresponding absorbance spectra of a. M03 and (M03+M30)/2 were measured on JASCO J-815 for solution and film samples, respectively.
A dispersion of (6,5) SWNTs with peak absorbance in the range of 0.5-0.9 had nearly zero CD and all other control experiments had small rotatory activity under stretching in the entire available range of wavelength.

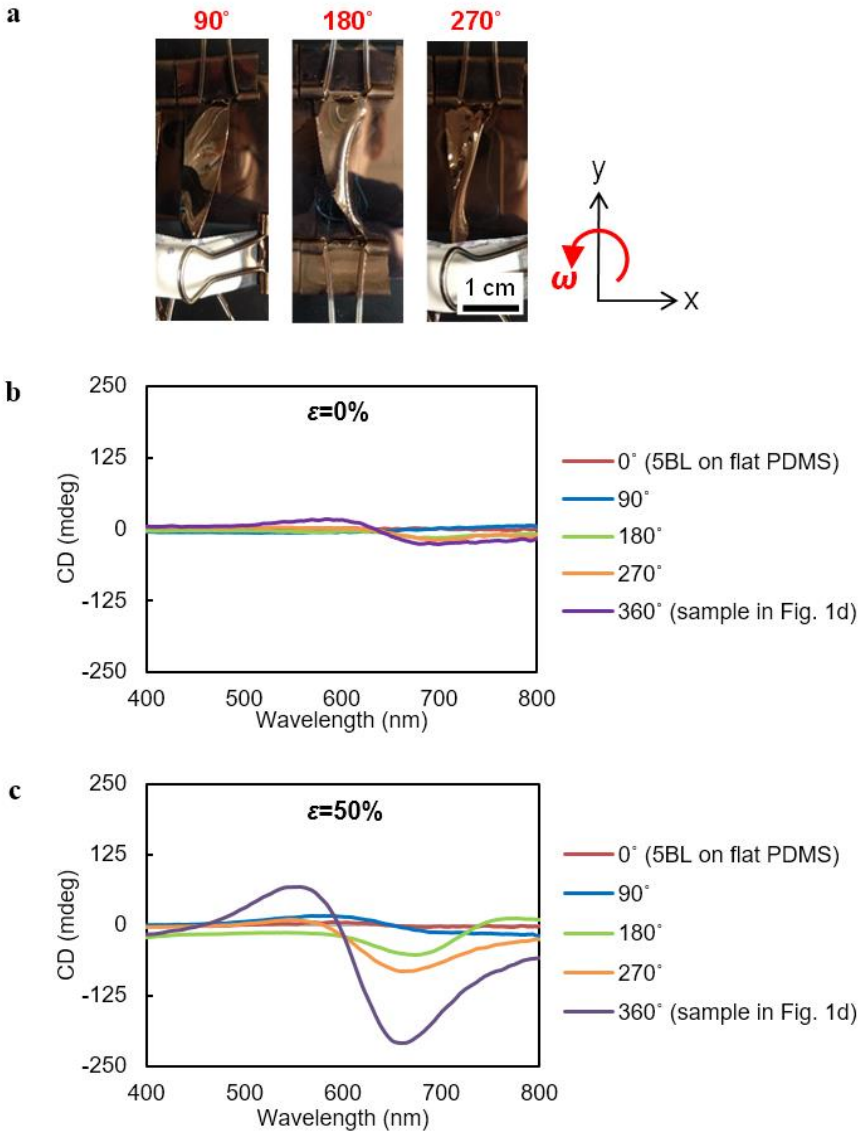

Figure 3.24. Emergence of CD depending on level of twist on Au composite. a, Photographs of samples under ω=90˚, 180˚ and 270˚ of twisting for $(PU/NP)_5$. ω is the rotational angle along the *y*-axis starting from the line of *x*-direction. **b**, **c**, CD, (M03+M30)/2, of $(PU/NP)_5$ depending on the level of twist under two different strain levels of 0% and 50%, respectively. Only RH samples were used for experiments. Twisting more than 360˚ made the surface of the samples severely rugged. Spectra obtained from JASCO J-815 spectrometer.

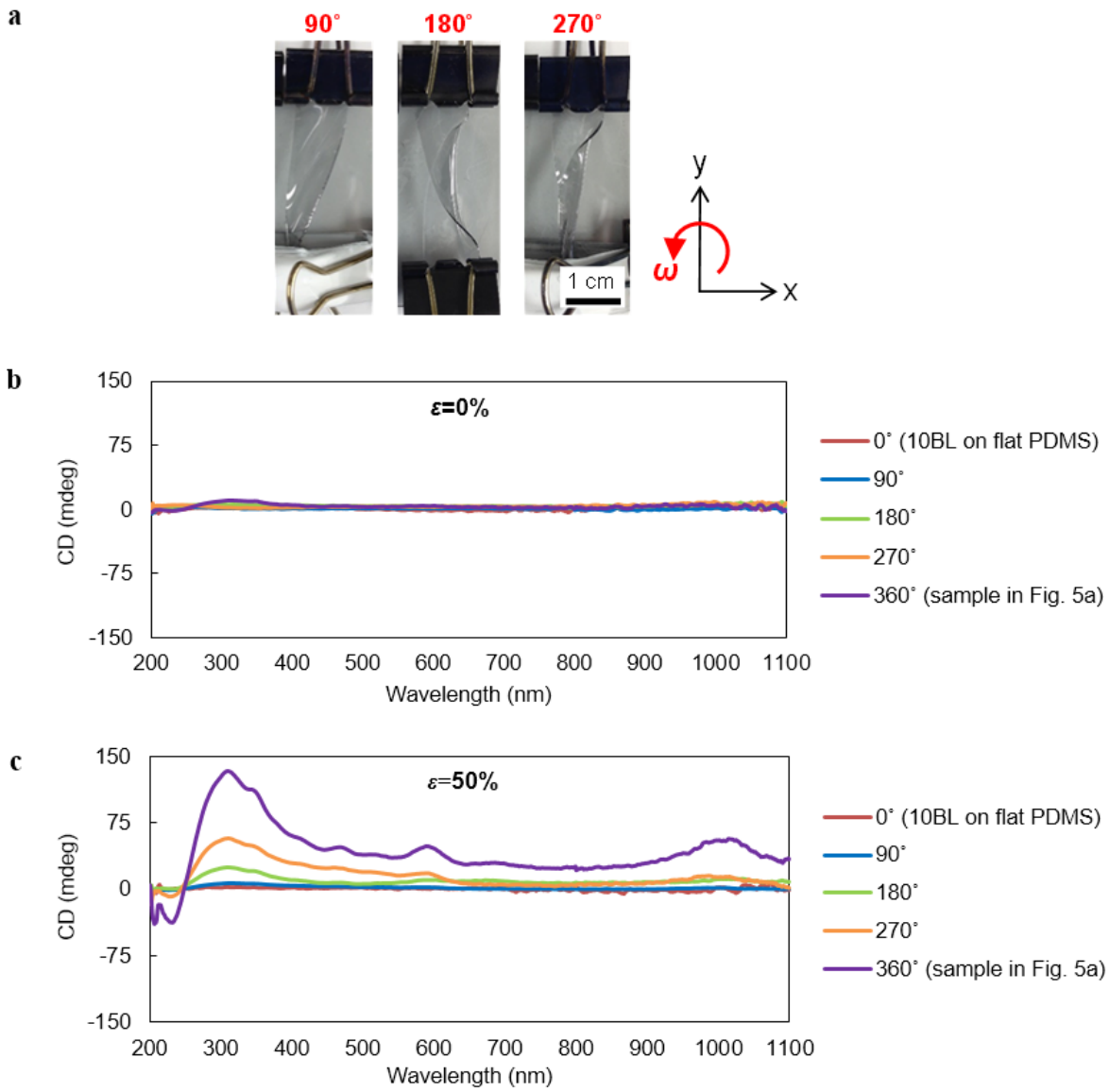

Figure 3.25. Emergence of chiroptical activity upon increase of the macroscale twist angle, ω, of the substrate on CNT composite. a, Photographic images of samples for ω = 90°, 180° and 270° for $(PVA/SWNT)_{10}$. **b**, **c**, CD spectra, (M03+M30)/2, of $(PVA/SWNT)_{10}$ for different ω under two different strain levels of ε = 0% and 50%, respectively. RH samples were only used for experiments.

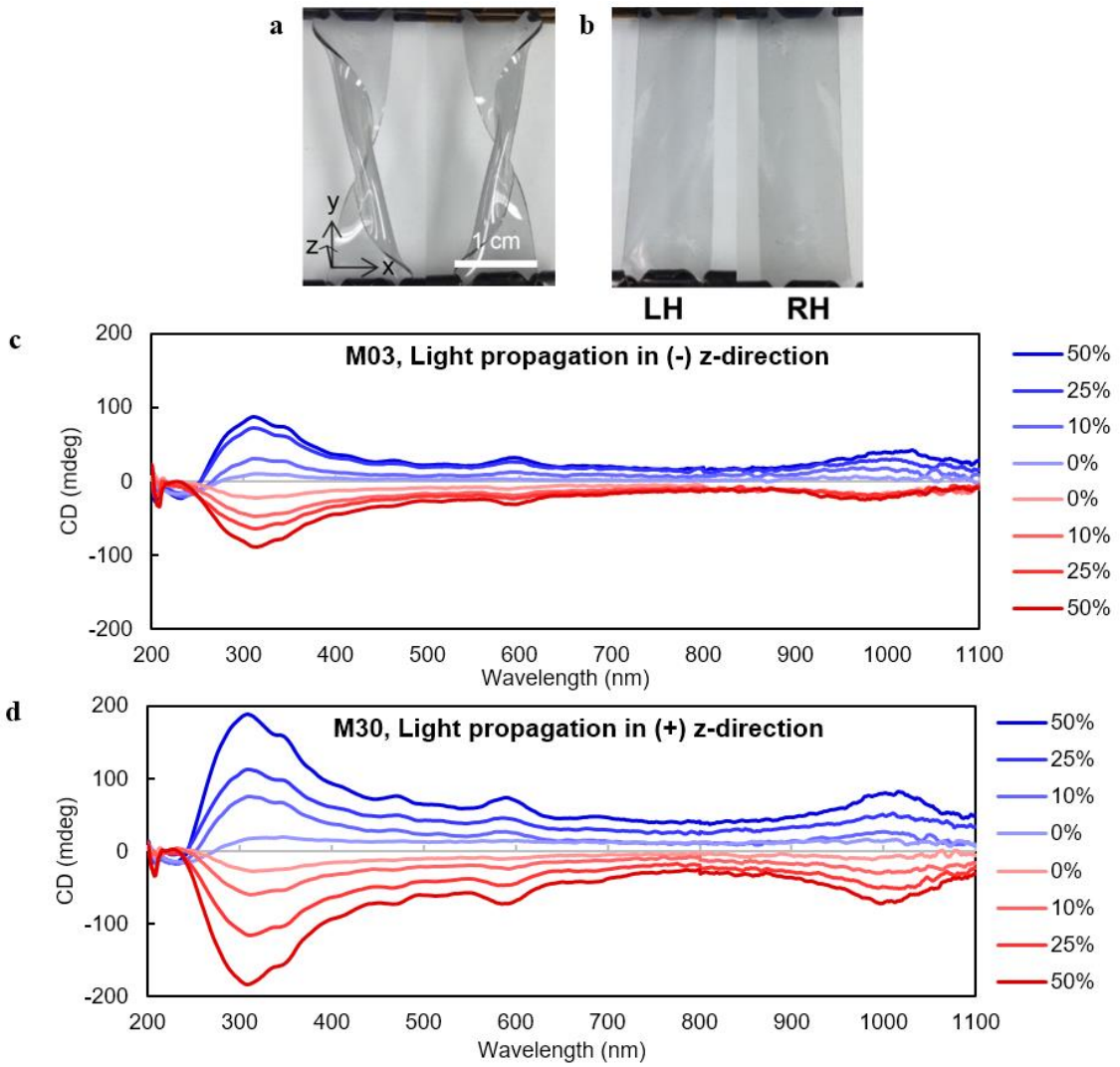

Figure 3.26. CNT Sample preparation and M03, M30 CD spectra. a, $(PVA/SWNT)_{10}$ were deposited on twisted PDMS substrates in opposite directions; right-handed Cartesian coordinates were used to denote directions of twisting and light propagation. **b**, Samples with left-handed and right-handed twists are denoted LH and RH, respectively as in the case of Au NPs. Scale for **a**-**b** is given in **a**. **c**, **d**, CD spectra from double-sided samples of LH and RH under ε = 0%, 10%, 25% and 50% with light propagation in negative and positive *z*-directions, respectively.

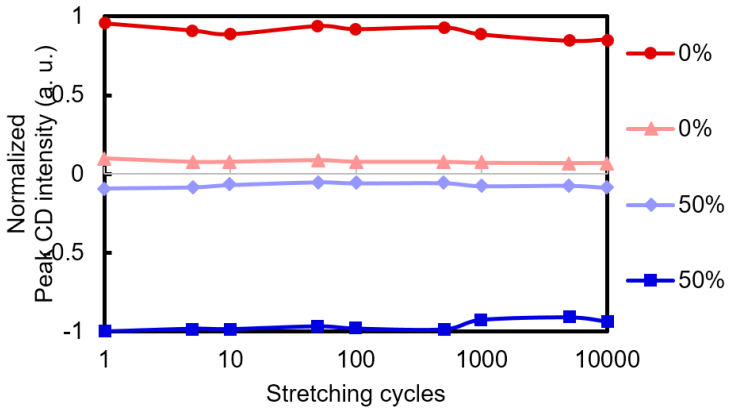

Figure 3.27. Reversibility test of Au composite. Peak CD, (M03+M30)/2, values of LH and RH samples up to 10,000 cycles of reversible stretching to 50% and releasing to 0%. Spectra obtained from JASCO J-815 spectrometer.

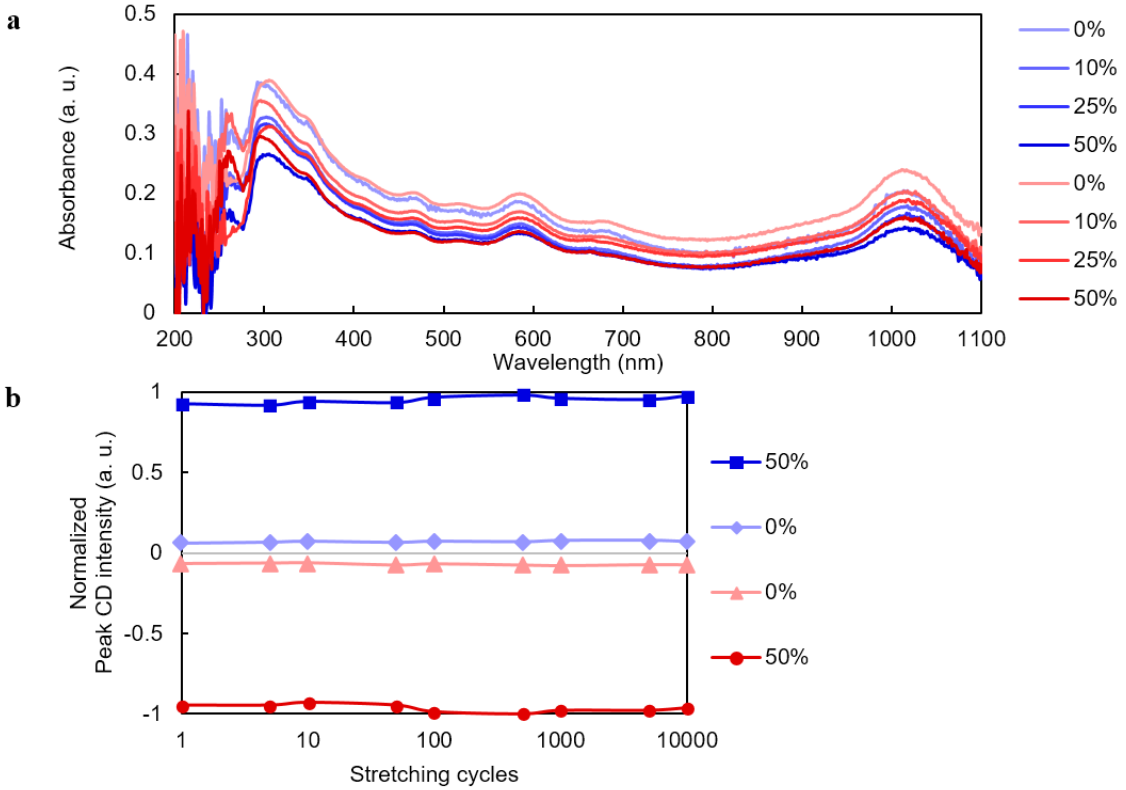

Figure 3.28. Absorbance spectra, and reversibility test of CNT composites. a, Absorbance spectra, (M03+M30)/2, of LH and RH samples under ε = 0, 10, 25 and 50% in Fig. 3.15b. **b**, Peak CD values of LH and RH up to 10,000 cycles of reversible stretching to 50% and releasing to 0%. Values were read at 300 nm.

3.9.6 Effect of Chain Length (Particle Density) for Chiroptical Activity.

We investigated chiroptical possibilities of linear contributions from dichroic NPs in discontinued or short chains combined with LB in strain polymer substrate. Same five bilayers were deposited by the same procedure to have decreased NP number density by more than one order of magnitude. The prepared samples had quite big absorbance up to 0.28 but had very small CD spectra (Fig. 3.29).

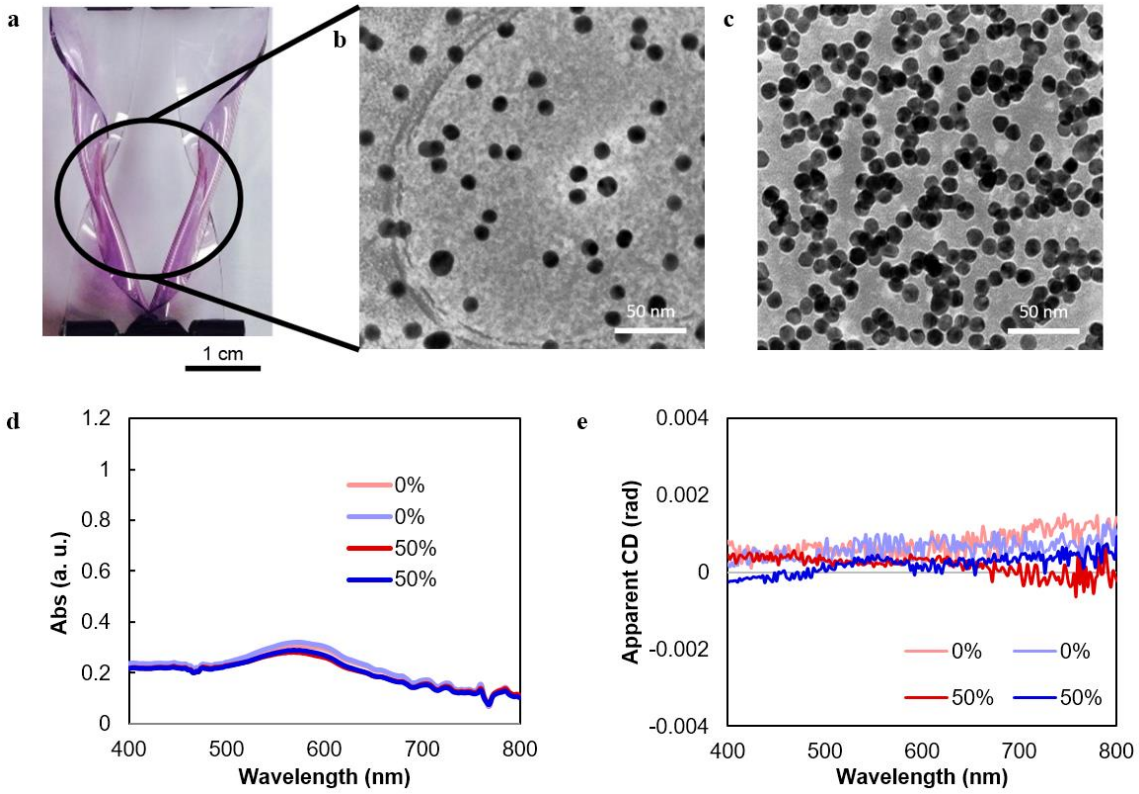

Figure 3.29. Samples containing less number of NPs and their optical response. a, Photographic image of a set of twisted form of $(PU/dilutedNP)_5$. **b**, **c**, TEM image of two bilayers of PU and diluted NPs and normal concentration of NPs used for most of the experiments, respectively. Particle number density in **b** and care in ca. tenfold difference. **d**, **e**, Absorbance and CD spectra of $(PU/dilutedNP)_5$ of LH and RH under ε = 0% and 50%, respectively. Apparent CD measured from Mueller matrix polarimetry.

13 nm Au NPs used and five bilayers deposited for all four cases

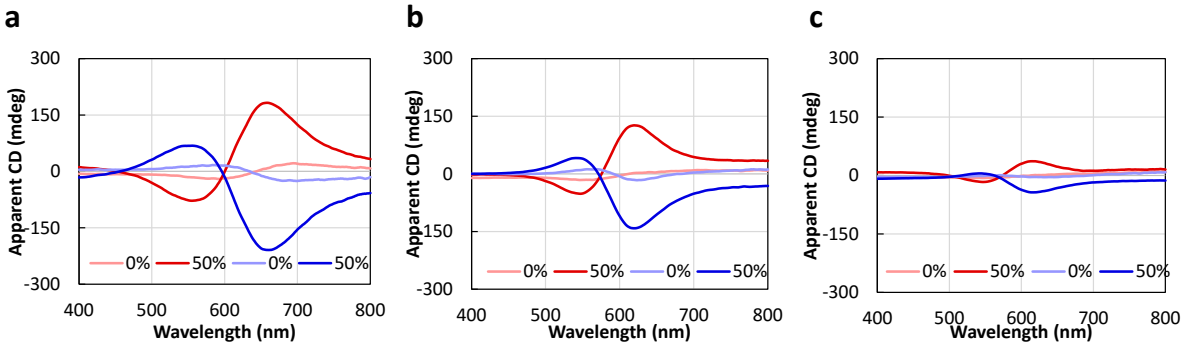

Figure 3.30. a, CD data in the main text with 20 min of dipping time into Au NP dispersion. **b**, CD data from 5 min of dipping time into Au NP dispersion. **c**, CD data from 1 min of dipping time into Au NP dispersion.

Different dipping times for Au NPs results in different NP fractions, as we learned from the previous study[55]. Apparent CD of double-sided samples were measured. 13 nm Au NPs used and five bilayers deposited for all four cases. We found a fact that with fewer NPs (which could mean shorter NP chains), CD peak under ε=50% blue-shifted: 658 nm, 625 nm and 610 nm (from **a** to **c**)

3.9.7 Effect of Particle Size for Chiroptical Activity.

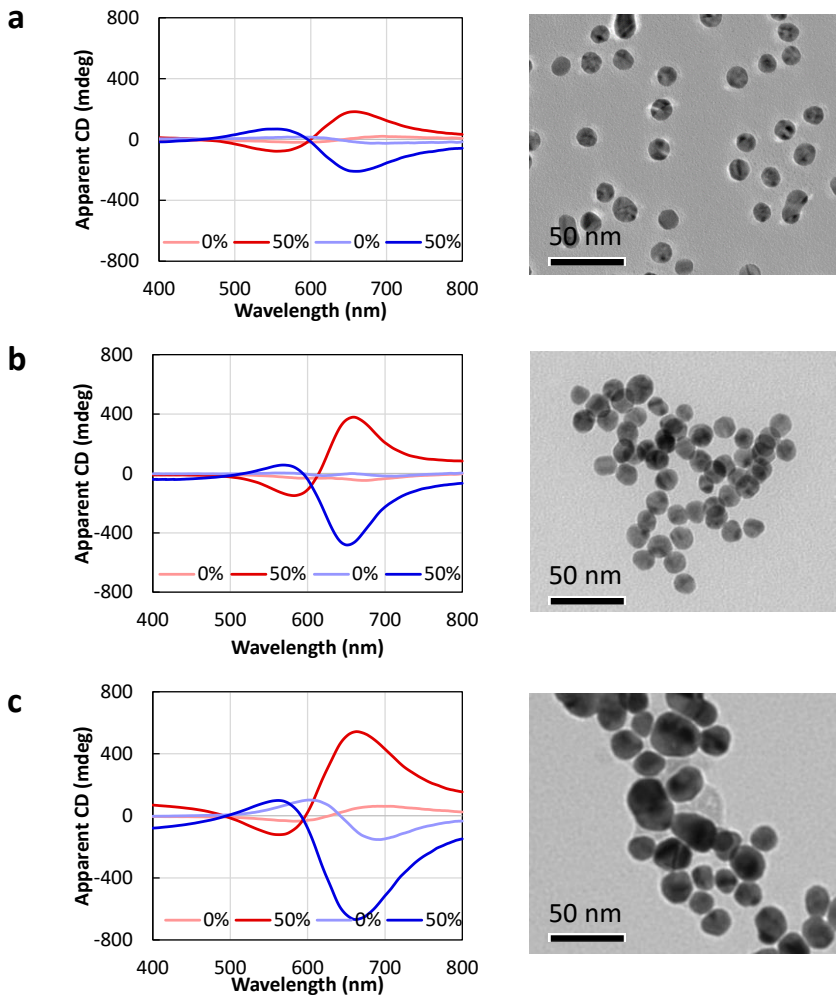

Figure 3.31. a, CD data in the main text with particle size of 13 ± 1 nm. **b**, CD data from particle size of 16 ± 2 nm. **c**, CD data from particle size of 37 ± 10 nm.

Different sized Au NPs were synthesized by changing amount of citrate surface stabilizer. Five bilayers deposited with controlled dipping time of 5 min for PU and 20 min for NPs. Apparent CD of double-sided samples were measured. CD peaks under ε=50% red-shifted: 658 nm, 663 nm and 668 nm (from **a** to **c**). This matches with the trend of the

absorption peak of NP dispersion: larger particles have peak at higher wavelengths. These (stronger extinction and red-shift pattern) was predicted by Mie theory

$$\sigma_{ext} = \frac{9V\epsilon_m^{3/2}}{c} \cdot \frac{\omega\epsilon_2(\omega)}{[\epsilon_1(\omega) + 2\epsilon_m]^2 + \epsilon_2(\omega 2)^2}$$

where *V* is the spherical particle volume, *c* the speed of light, ω the angular frequency of the exciting radiation, and ϵ_m is the dielectric constant of the surrounding medium. $\epsilon_1(\omega)$ and $\epsilon_2(\omega)$ denote the real and imaginary part of the dielectric function of the particle material, respectively ($\epsilon(\omega) = \epsilon_1(\omega) + i\epsilon_2(\omega)$). Extinction cross-section, σ_{ext}, increases as the volume ($4/3\pi R^3$) of spherical particle increases. Mie's solution to the Maxwell equation is valid for small nanoparticles, < 100 nm[143,144]. The red-shift is regarded as electromagnetic retardation in larger nanoparticles[145,146,147].

3.9.8 Spatial Homogeneity

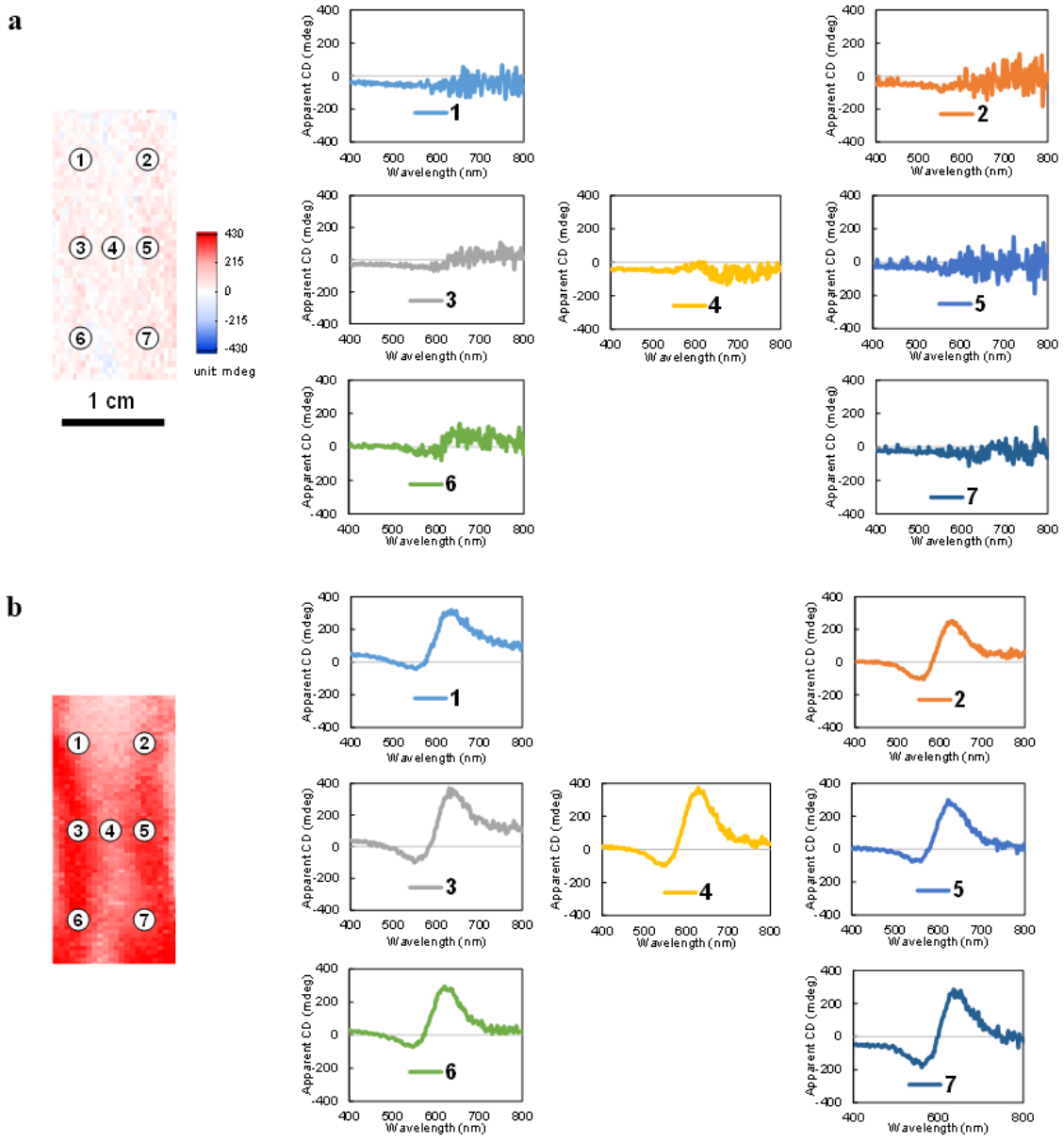

Figure 3.32. Spatial homogeneity and relevant apparent CD spectra of LH samples. With a beam size of 1.5 mm, CD spectra on seven representative spots on double-sided samples were measured and relevant spectra are presented: ε=0% (**a**), and ε=50% (**b**). Color CD bar and scale for images **a**-**b** are given in **a**.

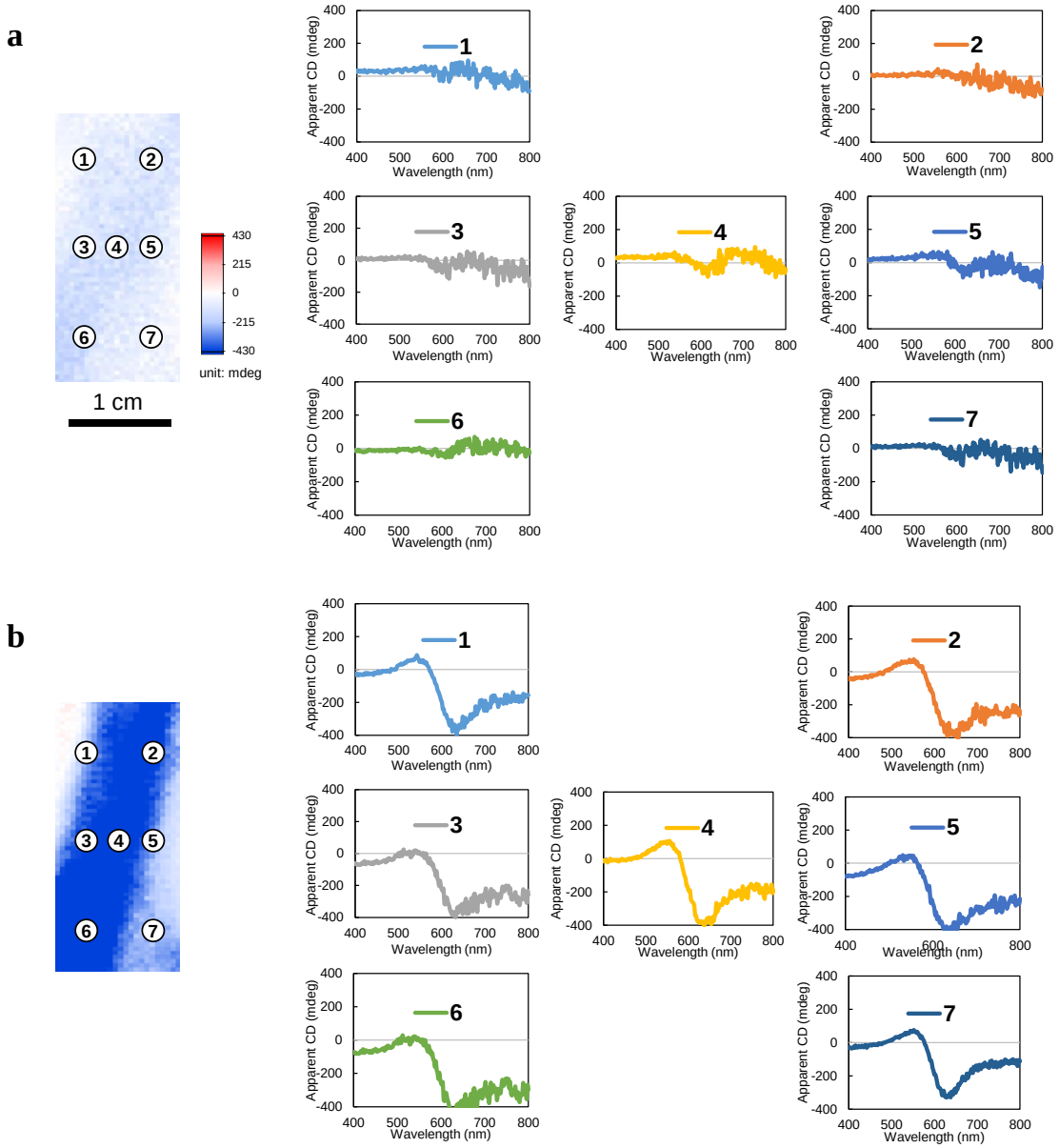

Figure 3.33. Spatial homogeneity and relevant apparent CD spectra of RH samples. With a beam size of 1.5 mm, CD spectra on seven representative spots on double-sided samples were measured and relevant spectra are presented: ε=0% (**a**), and ε=50% (**b**). Color CD bar and scale for images **a**-**b** are given in **a**.

LBL process is known for production of highly uniform coating with homogeneous film thickness throughout the substrate[12,148,149,46,121]. Multilayer deposition on twisted substrate were homogeneous and conformal (Fig. 3.1c).

Mapping of samples by Mueller matrix polarimetry showed how our NP layers were spatially homogeneous in large regions of samples. In addition to entire sample area mapping data (Fig. 3.1g, h), spectra for all interested wavelength regime was also obtained by polarimetry with a beam size of 1.5 mm diameter for representative 7 spots (Fig. 3.32 and 3.33). All the above data proved our chiroptical samples were homogeneous even under higher strains. However, we should note that samples had marginal optical inhomogeneity due to; 1) twisting and clamping makes the stress field to be in a gradient (Fig. 3.9d-i and Fig. 3.30) and 2) stress are higher in the center of the films and lower at the edges. Since shapes of buckles and cracks are dependent on local stress fields, geometry of assembled particles should have some differences over samples. Still, this inhomogeneity was extremely minor and only observed within very small areas such as at the edge or close to the clamps. All the above statements can be applied to more than 100 samples tested in the course of this work.

3.9.9 Bending Stresses and Buckling/Cracking Phenomena

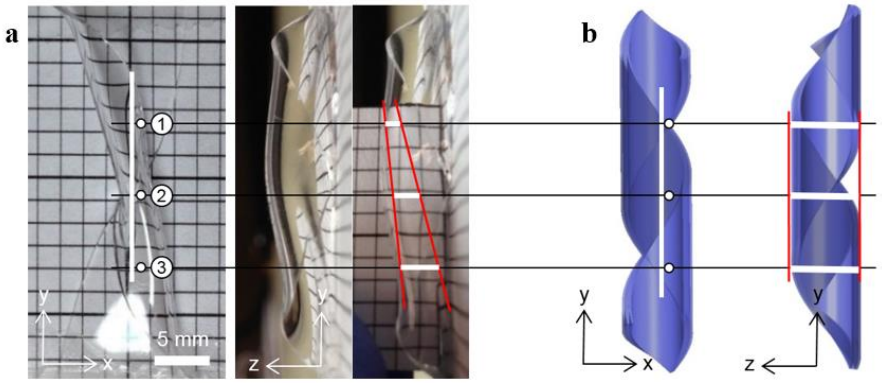

Figure 3.34. Curvature of substrate and bending stresses. a, Photographic image of twisted and clamped PDMS showing gradient of curvatures. **b**, Schematic of twist-only geometries showing same curvatures throughout the substrate.

Stress accumulated to each point was calculated by Hooke's law, (Eq. 3.3), for bending deformations:

$$\sigma_{\max} = E_s c_{\max} \kappa \qquad \text{(Eq. 3.3)}$$

where, E_s is elastic modulus of the substrate, c_{max} is distance from the neutral axis to the outermost surface of convex side, and κ is curvature (reciprocal of radius)[126]. For calculation, E_s of 2.6 MPa, C_{max} of 0.25 mm, and κ of 1500 m^{-1}, 874 m^{-1} and 583 m^{-1} for points of 1, 2 and 3 were used, respectively.

3.9.10 Theoretical Parameters of Buckling and Cracking Phenomena.

Composite LBL films on convex and concave sides were buckled and cracked, respectively, due to compressive and tensional forces occurring during relaxation to the flat state. Periodicity of buckles, λ, and cracks, d, as well as amplitude of buckles can be calculated as follows[84,150,151]:

$$\lambda = 2\pi t \left[\frac{(1-\nu_s{}^2)E_f}{(1-\nu_f{}^2)E_s}\right]^{1/3} \qquad \text{(Eq. 3.4)}$$

$$A = h\sqrt{\frac{\varepsilon_{pre}}{\varepsilon_c} - 1} \quad \text{where,} \quad \varepsilon_c = \frac{1}{4}\left[\frac{3(1-\nu_f{}^2)E_s}{(1-\nu_s{}^2)E_f}\right]^{2/3} \qquad \text{(Eq. 3.5)}$$

$$d = \frac{4t\sigma^*}{E_s\varepsilon} \qquad \text{(Eq. 3.6)}$$

Table 3.1. Definition of constants and their values for each chiroptical nanocomposites.

	$(PU/NP)_5$	**$(PVA/SWNT)_{10}$**
***t*, thickness of the multilayers**	40 nm	18 nm
ν_s, Poisson's ratio of the substrate in *z*-direction	0.18	0.18
ν_f, Poisson's ratio of the multilayers in *z*-direction	0.26	0.07
E_s, elastic modulus of the substrate	2 MPa	2 MPa
E_f, elastic modulus of the multilayers	125 MPa	1190 MPa
σ^*, ultimate strength of the multilayers	13 MPa	720 MPa
ε, strain to the *x*-axis in percent, (C_{max}/*radius*)*100	21.9%	21.9%

t values were obtained from Fig. 3.32. ν_f, E_f, and σ^* were measured from free-standing LBL films. Ability to obtain such data is one of advantages of LBL composites over some

other methods of composite preparation. Poisson's ratios of PDMS were measured to be v_{length} = 0.176 and v_{height} = 0.008.

From the above parameters we calculated periodicities of the buckles, λ, and cracks, d, for both chiroptical nanocomposites (Fig. 3.35) and they all give a close match with the experimentally measured values (Fig. 3.38, 3.44, 3.45, and Table 3.1 and 3.2). d was calculated/measured for the center of the film where equal magnitudes of tensional stresses were applied. Experimental values are measured from LH samples.

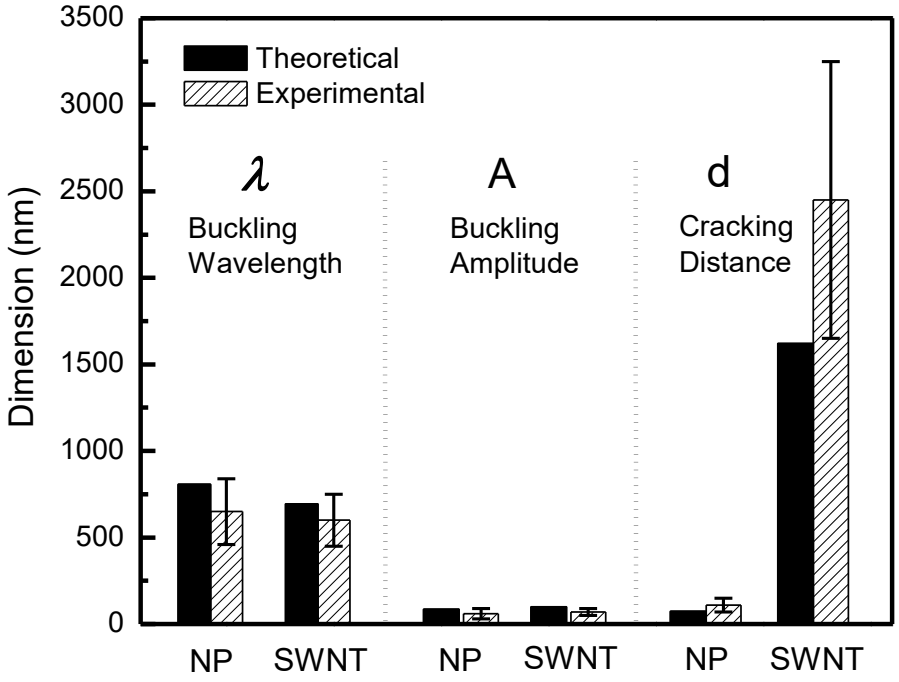

Figure 3.35. Comparison of theoretical and experimental parameter values. NP and SWNT signify NP composite, $(PU/NP)_5$, and SWNT composite, $(PVA/SWNT)_{10}$, respectively. Error bars are mean±s.d for 95% confidence (n=20).

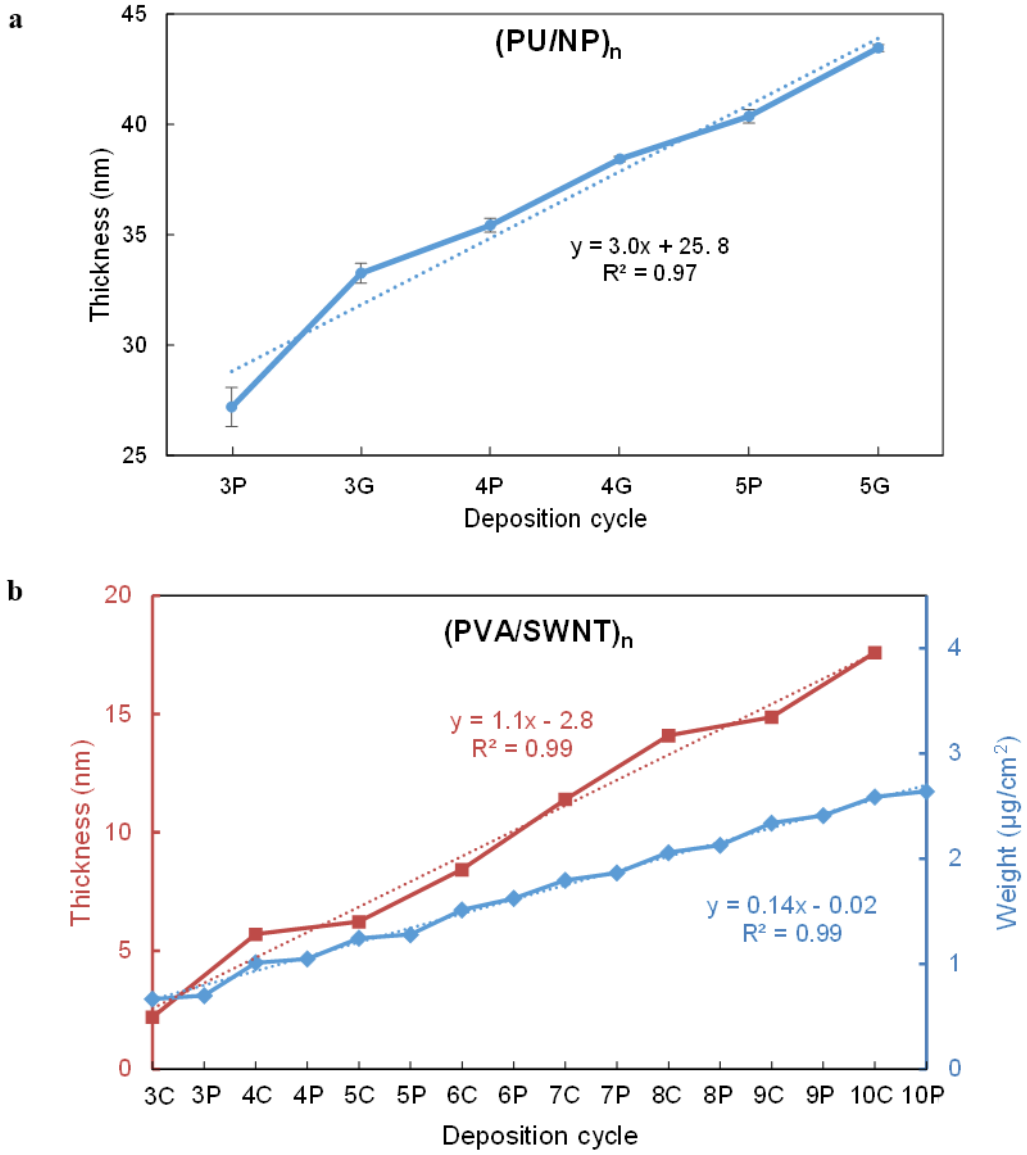

Figure 3.36. Multilayer growth profiles. a, Thickness of $(PU/NP)_5$ was measured by ellipsometry after deposition of each layer on silicon wafer. Polyurethane (3P, 4P, and 5P) and Au NP (3G, 4G, and 5G) layers with the same number correspond to one deposition cycle. Error bars are mean±s.d. for 95% confidence (n=3). **b**, Thickness and weight of $(PVA/SWNT)_n$ were measured by ellipsometry after deposition of each bilayer on silicon wafer and by quartz crystal microbalance frequency shifts after deposition of each layer on 5 MHz quartz crystals, respectively. Carbon nanotubes (3C, 4C, and 5C) and polyvinyl alcohol (3P, 4P, and 5P) layers with the same number correspond to one deposition step.

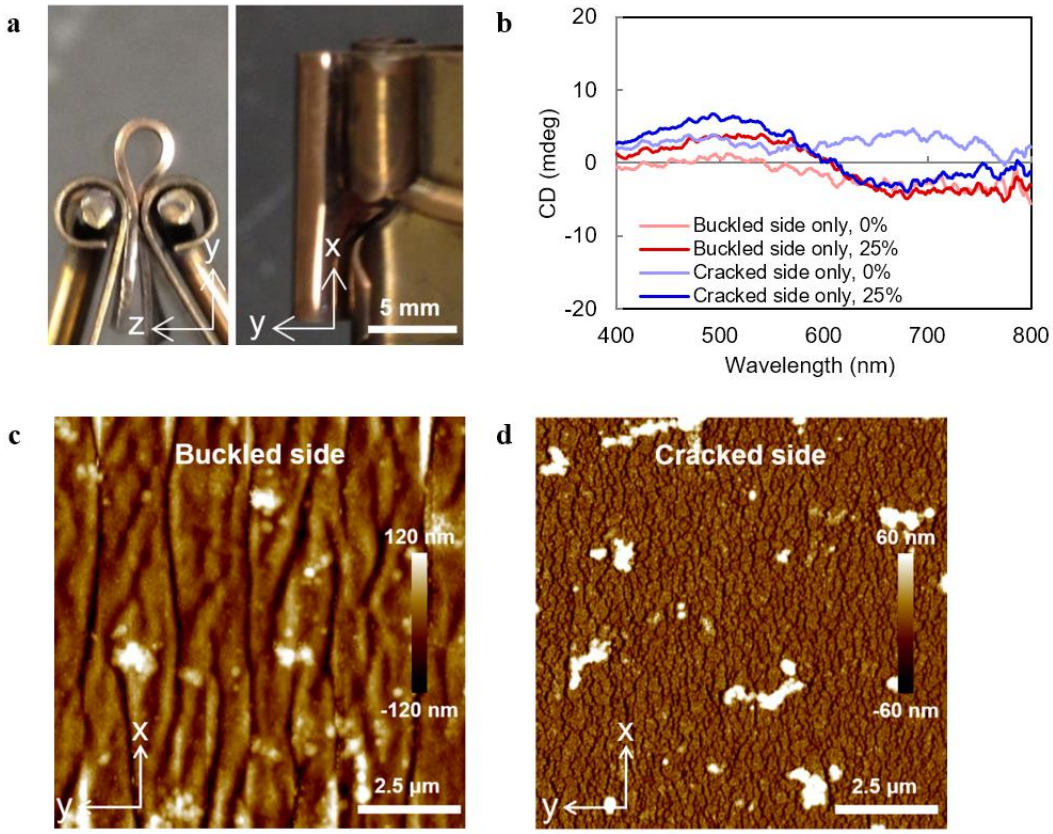

Figure 3.37. CD spectra and morphology without a strain gradient. a, Photographic images of the sample with constant curvature of 645 m^{-1}. Samples were released to have buckled and cracked sides and stretched along the *y*-axis. **b**, CD spectra, (M03+M30)/2, of buckled and cracked sides only under ε = 0% and 25%. **c**, **d**, AFM images of buckled and cracked sides of the composite films. CD spectra obtained from JASCO J-815 spectrometer.

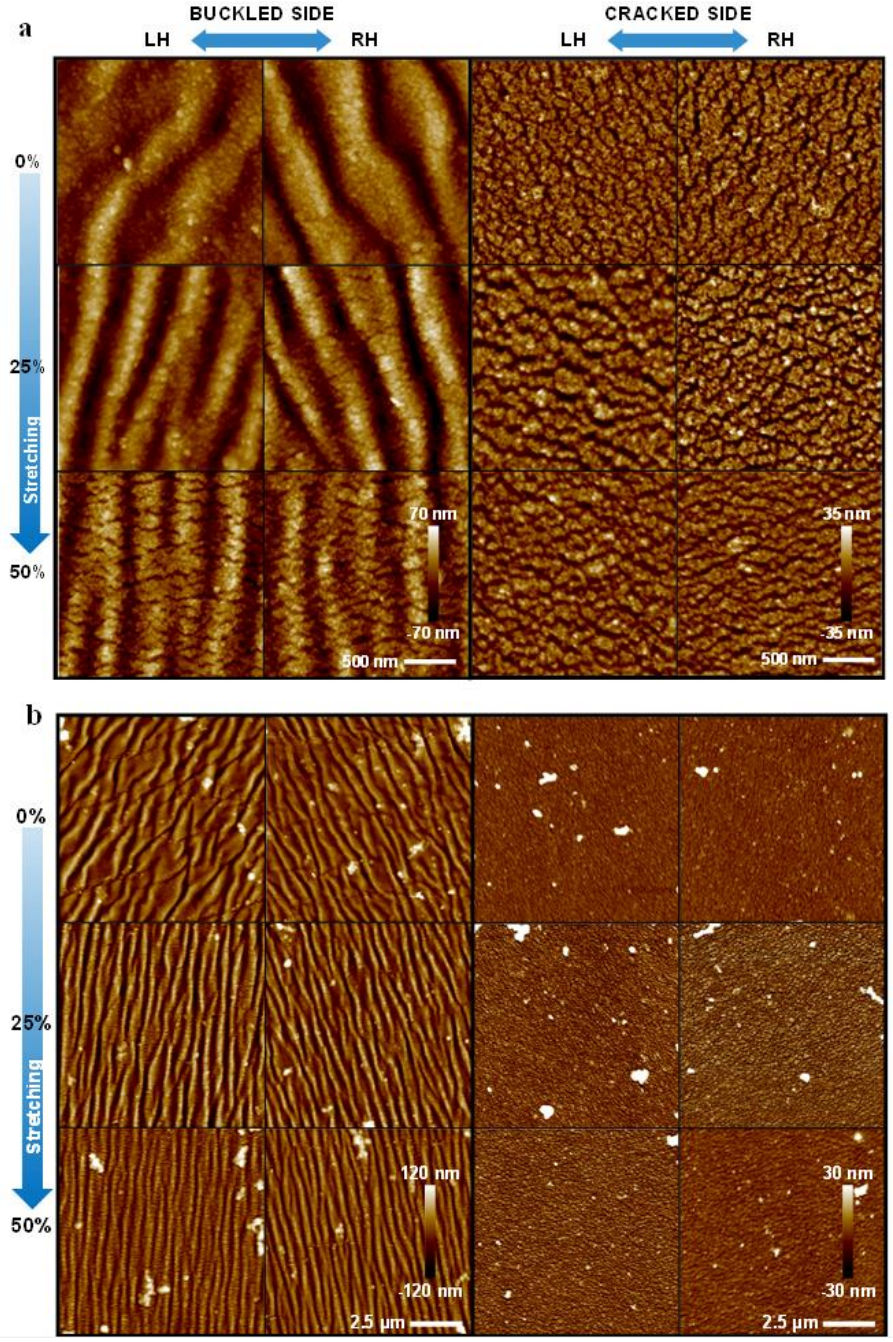

Figure 3.38. Large area AFM images with different deformation modalities of Au composites. a, Buckled and cracked sides of LH and RH samples of the composite films under ε = 0%, 25%, and 50%, respectively. **b**, Larger area images of **a**. Height (*z*-axis) and planar (*x*-*y* plane) scales for images are given lower right section of each data set.

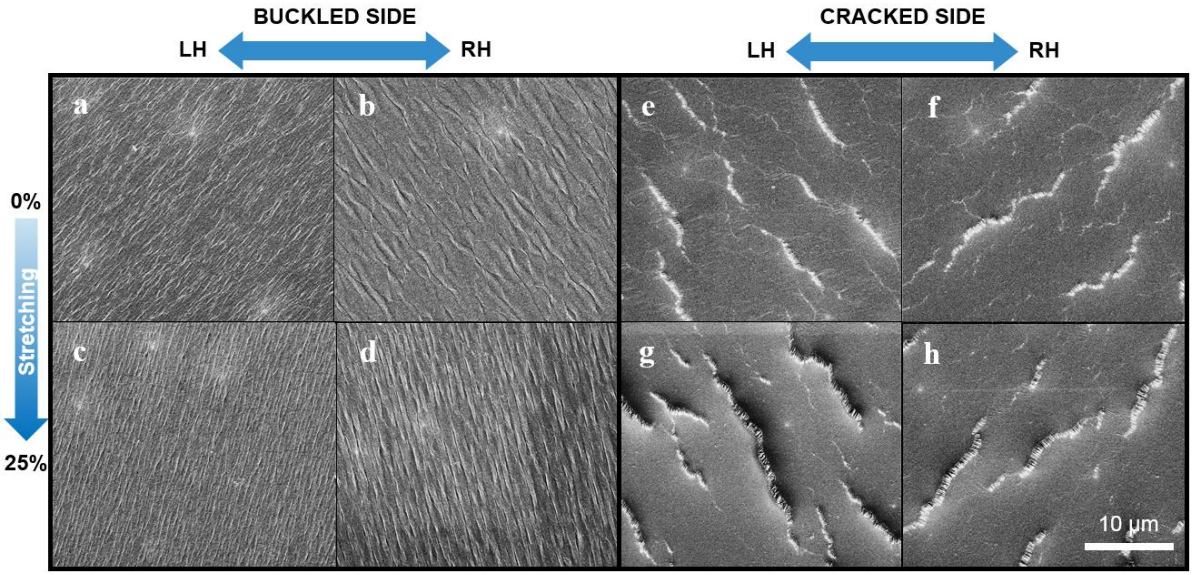

Figure 3.39. SEM surface images of CNT composites. a-h, Buckled and cracked sides of LH and RH samples under ε = 0%, and 25%, respectively. Scale for images **a-h** is given in **h**.

3.9.11 Interparticle Distance and Arrangements

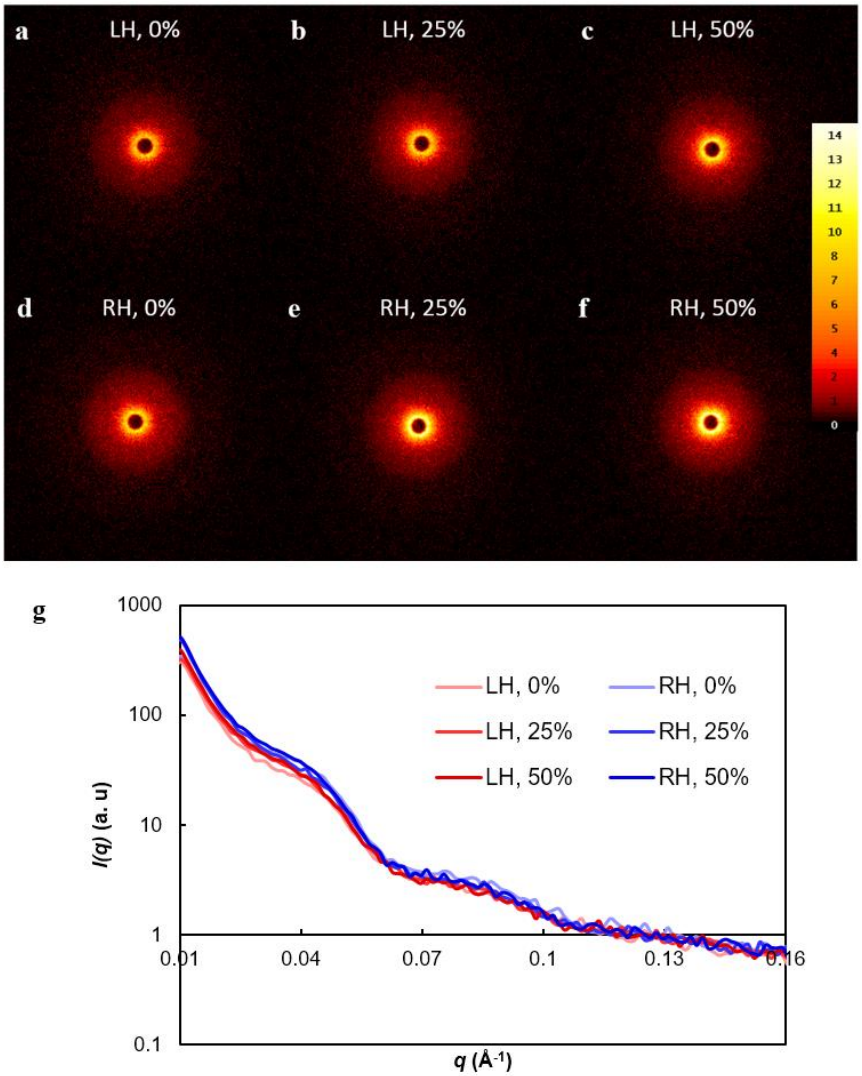

Figure 3.40. Small angle X-ray scattering (SAXS) measurements for interparticle distance. **a-f**, Beam patterns of LH and RH samples under ε=0%, 25% and 50%, respectively. **g**, Plot of intensity, *I(q)*, as a function of scattering vector, *q*. *d*-spacing, $2\pi/q^*$, values were averaged from six measurements to be 13.8 ± 0.1 nm.

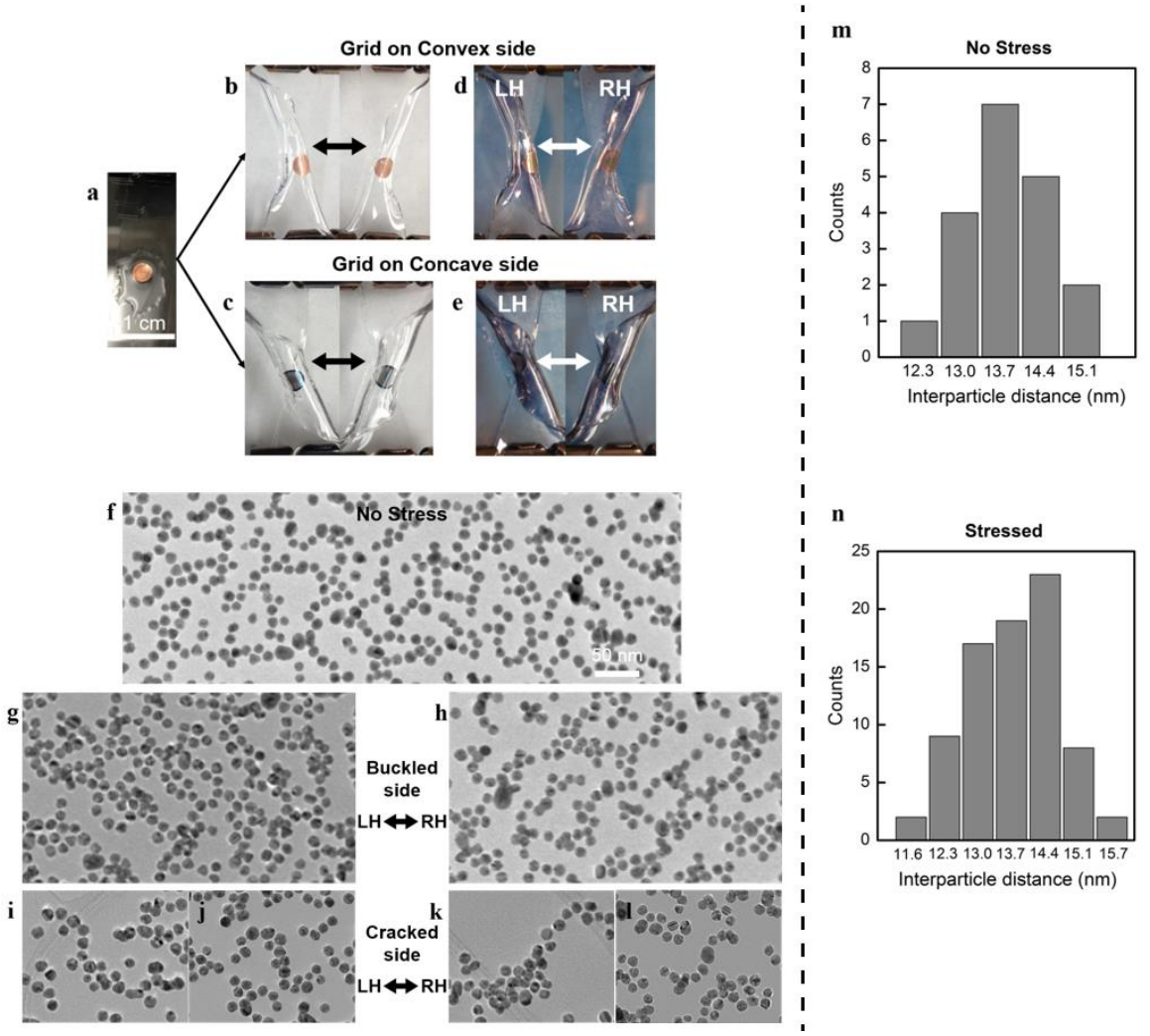

Figure 3.41. Reorganization of NPs into *S*-like chains under stresses. a-e, Photographic images of sample preparation: **a**, TEM grid was placed on the middle of the elastic substrate and then liquid-state PDMS was pasted around the grid, followed by curing. **b**, **c**, The substrates were coiled and clamped to have handedness. **d**, **e**, $(PU/NP)_2$ films were deposited onto the twisted substrates. The scale for **a-e** is given in **a**. **f**, TEM image of $(PU/NP)_2$ deposited on the flat grid. **g**, **h**, Buckled side TEM images of LH and RH from **d**, respectively. **i-l**, Cracked side TEM images of LH (**i**, **j**) and RH (**k**, **l**) from **e**. For TEM imaging, samples were relaxed to be flattened followed by removal of grids from the substrates. For **b**, **d**, and **c**, **e**, one and three substrates were used, respectively, in order to apply maximized stresses to the grid on each side and a large gradient of stresses throughout the samples. Scale for **f-l** is given in **f**. **m**, **n**, Distribution of the center-to-center distance between nanoparticles under no-stress (**f**, 13.8 ± 0.1 nm, *n*=40) and stressed states (**g-l**, 13.7 ± 0.1 nm, *n*=80), respectively.

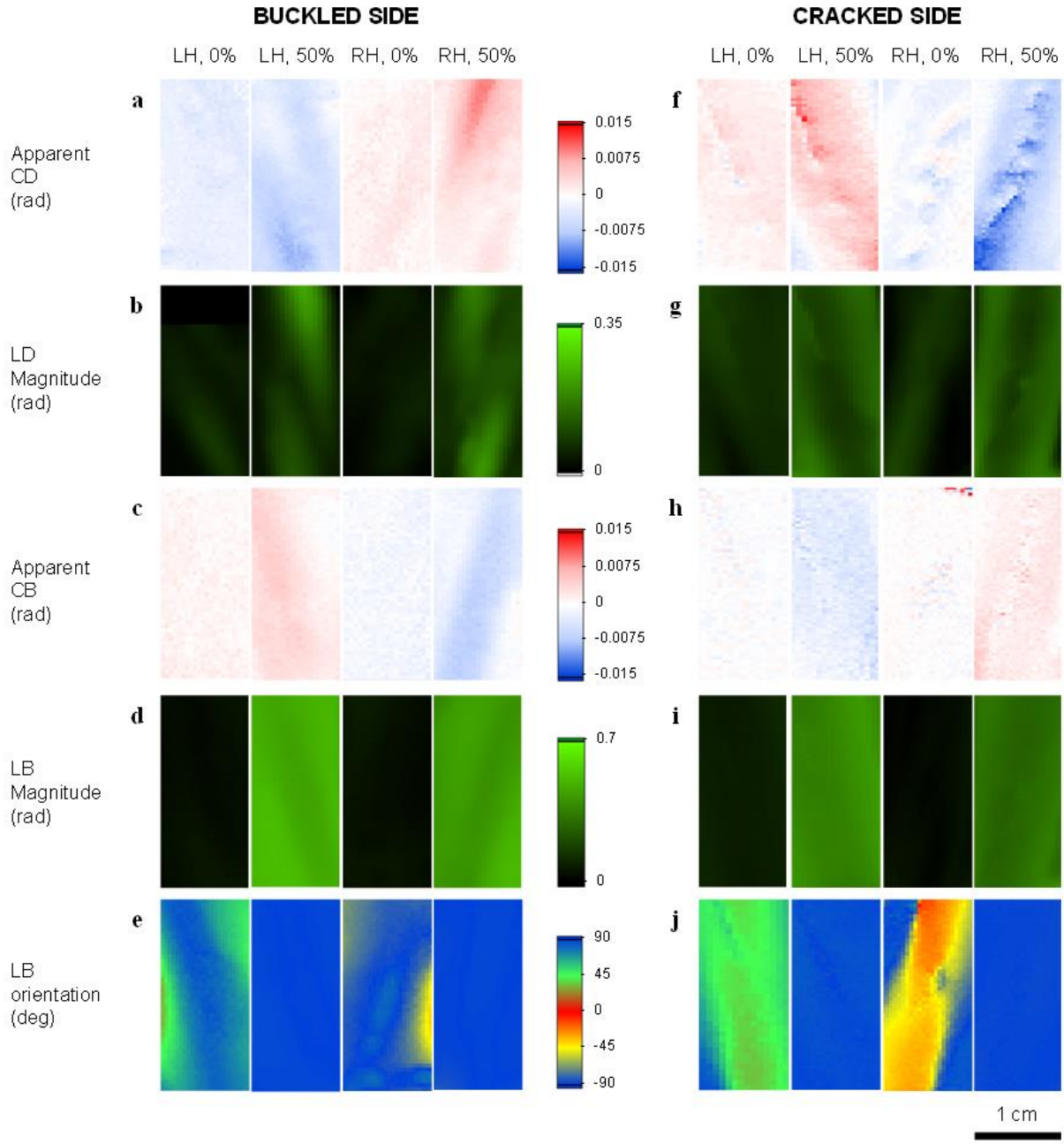

Figure 3.42. Mapping of single-sided samples. a-e, Apparent CD, LD magnitude, apparent CB, LB magnitude and LB orientation of LH and RH samples under strains of 0% and 50% buckled side. **f-j**, Apparent CD, LD magnitude, apparent CB, LB magnitude and LB orientation of LH and RH samples under strains of 0% and 50% on cracked side.

3.9.12 Dimensions of NP S-chains.

Dimensions of NP chains were measured from AFM height images and summarized in Fig. 3.45.

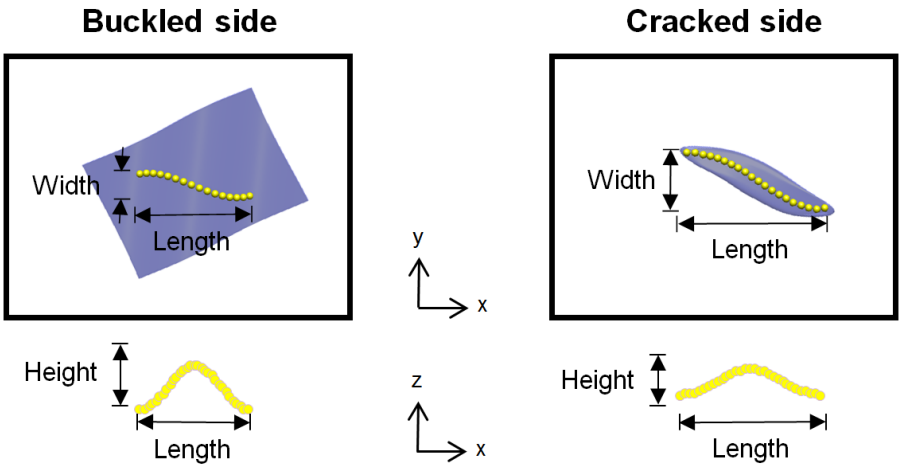

Figure 3.43. Schematic drawings showing unified dimension descriptors for chains of both buckled and cracked sides.

Length and Width: Directly measured from planar AFM height sensor images.

Height: For the buckled side, a section line in white color was drawn on the AFM height sensor image and the depth profiles are generated. Heights are obtained from the distance between the highest and the lowest values in the plot. For the cracked side, depth histograms of AFM image were generated and heights were taken from the distance between two peaks with the most and second-most dense populations.

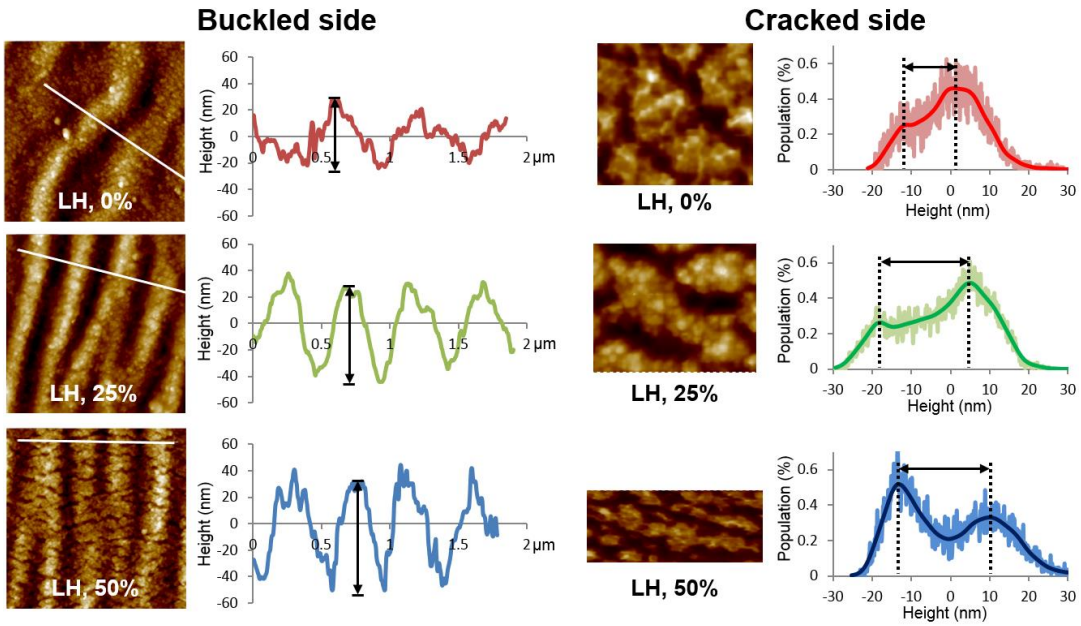

Figure 3.44. AFM images and relevant plots for geometry assessments. Left and right columns for the buckled and cracked sides of the composite films, respectively.

Table 3.2. Calculated number of NPs in *S*-chains. Error bars are mean±s.d. for 95% confidence (*n*=20).

	Buckled side	**Cracked side**
LH, ε=0%	49 ± 14	71 ± 7
LH, ε=25%	37 ± 5	48 ± 10
LH, ε=50%	31 ± 7	36 ± 10
RH, ε=0%	49 ± 14	70 ± 11
RH, ε=25%	35 ± 8	44 ± 6
RH, ε=50%	32 ± 8	38 ± 9

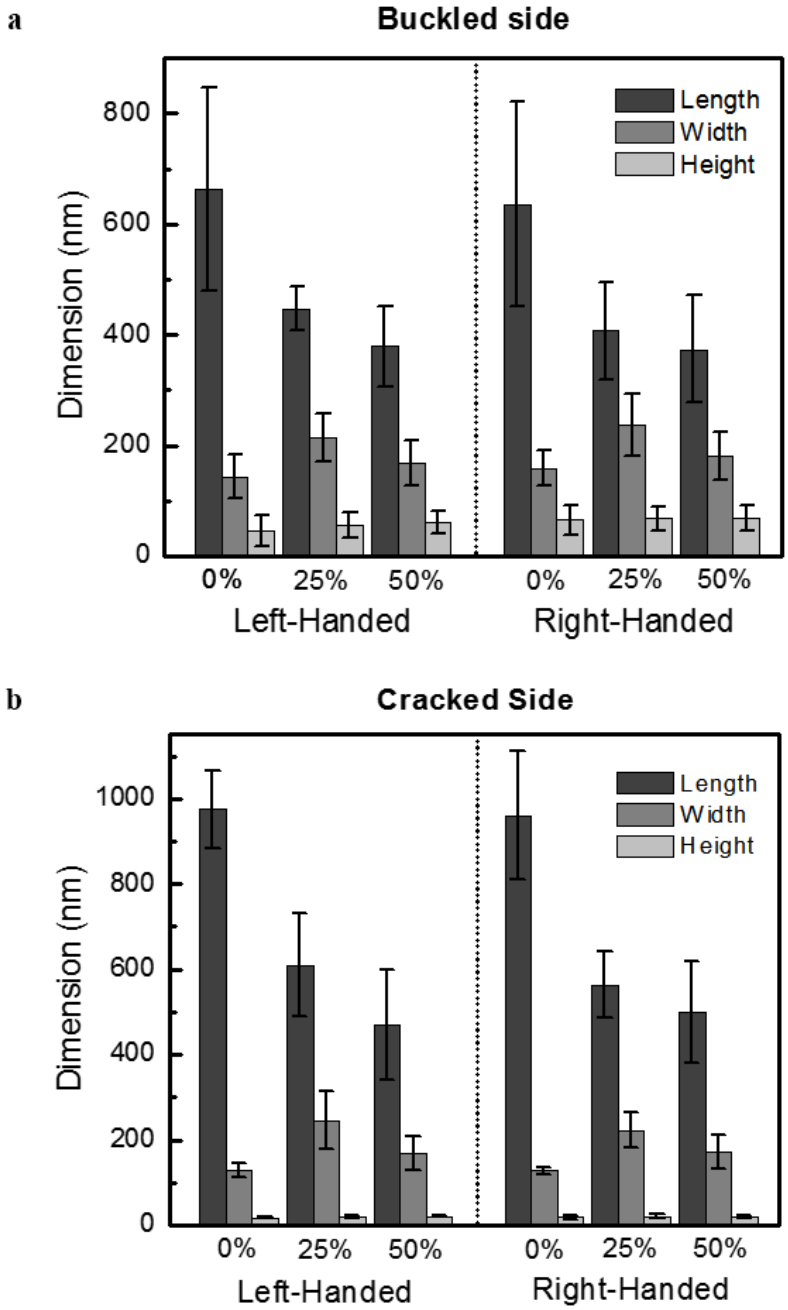

Figure 3.45. Dimensions of NP S-chains. Each dimension (length, width, and height) for each handedness and each side, buckled **a** and cracked **b**, of the composite films under ε =0, 25, and 50% was summarized as bar charts. Error bars are mean±s.d. for 95% confidence (n=20). Mean values for each dimension were used for construction of chain model for simulation.

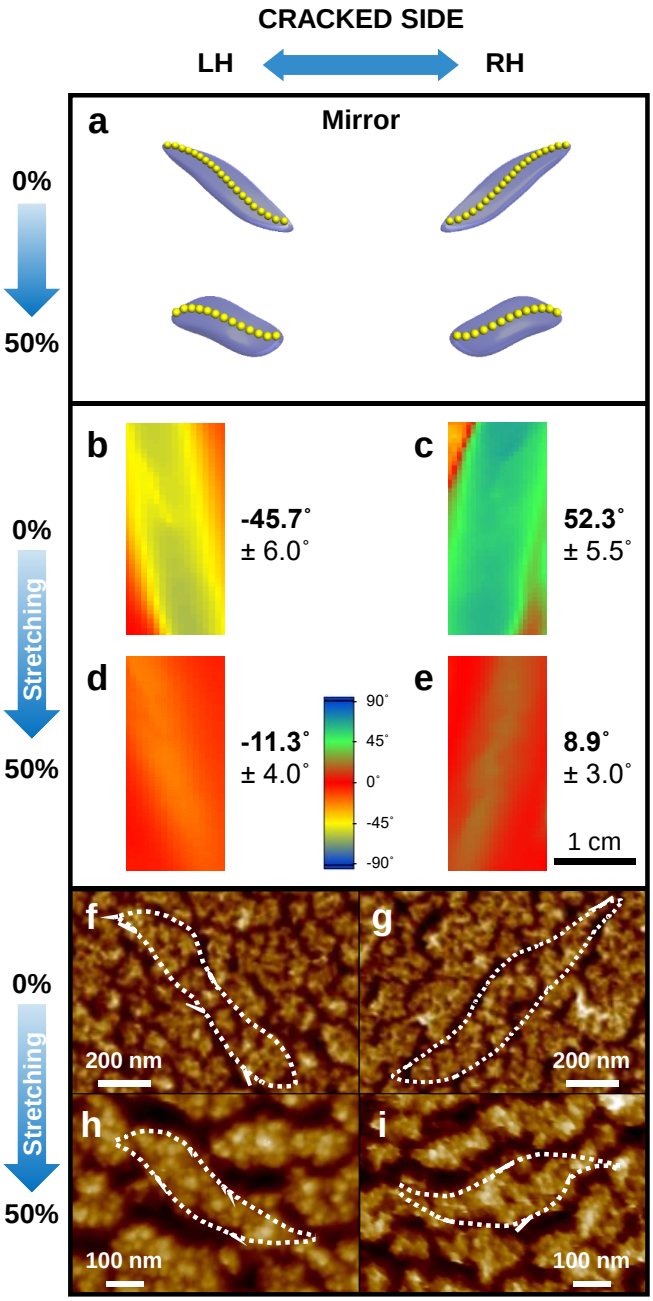

Figure 3.46. Orientation and alignment of NP chains on cracked side. All data in this figure set are from cracked side only. **a**, Schematic drawings of mirrored images of NP islands under ε = 0 and 50%. **b-e**, LD orientation of LH, ε = 0% (**b**), RH, ε = 0% (**c**), LH, ε = 50% (**d**) and RH, ε = 50% (**e**), respectively, obtained from plasmonic wavelengths. Numerically averaged values (n=20) written by the mapping data. Color angle bar and scale for images **b-e** are given in **d** and **e**, respectively. Angles are projectable using classical 2D Cartesian coordinates. **f-i**, Magnified AFM images of LH, ε = 0% (**f**), RH, ε = 0% (**g**), LH, ε = 50% (**h**) and RH, ε = 50% (**i**), respectively. Large area AFM images are in Fig. 3.34.

3.9.13 Chirality *F*-factor for *S*-chains.

We shall define the chirality factor as

$$F = \left(\frac{Width}{Length}\right) * \left(\frac{Height}{Length}\right) \qquad \text{(Eq. 3.7)}$$

where width, height and length represent the geometrical parameters as defined in Fig. 3.35, 3.43 and 3.44. Eq. 3.7 was applied to calculate chirality *F*-factor of chains for buckled side and values are summarized in Fig. 3.47. We assumed that arrangement of NPs into S-shaped chain can be described by trigonometric functions. The 3D chiral *F*-factor for chains made from identical NPs represents how much the geometry of the particle arrangement deviates from the achiral 1D straight line or 2D wavy line, which will have *F*=0.

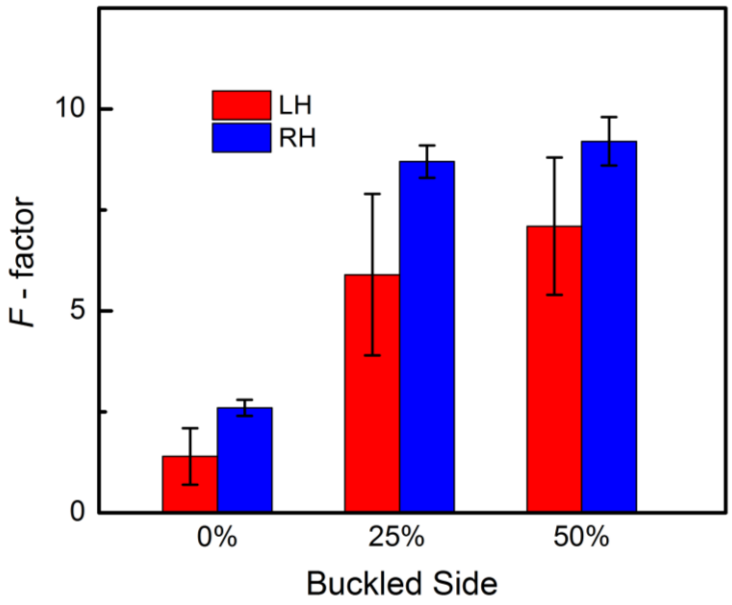

Figure 3.47. Chirality *F*-factor of NP chains. *F*-factor of LH and RH of chiroptical composites for buckled and cracked sides under ε = 0, 25, and 50%, respectively, are summarized as bar charts. Error bars are mean±s.d. for 95% confidence (*n*=20). *F*-factor values were multiplied by 100.

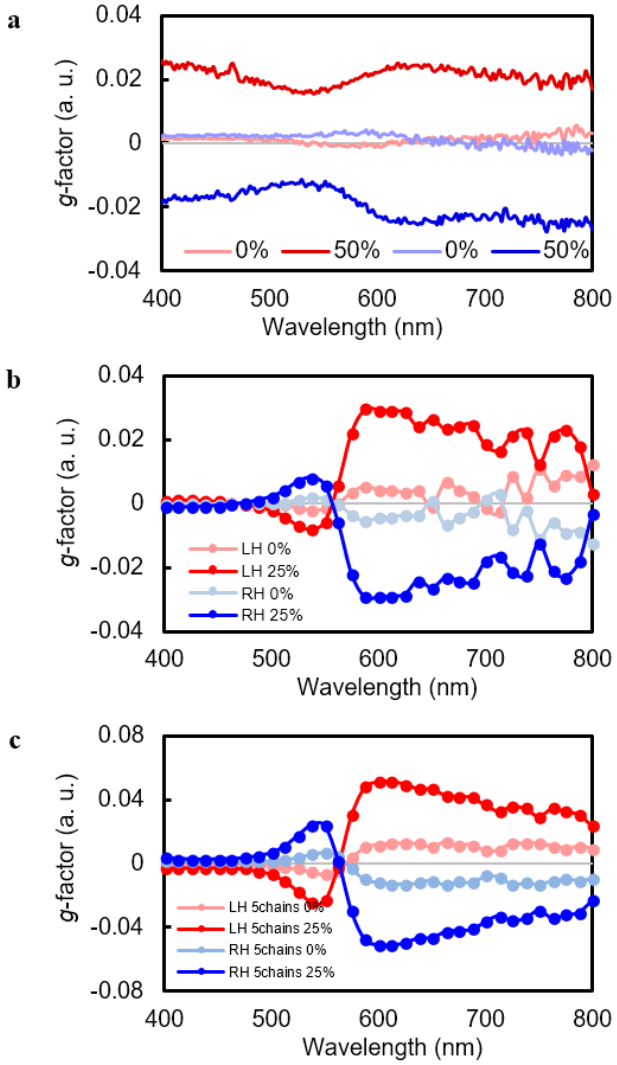

Figure 3.48. Experimental and calculated *g*-factors. a, *g*-factor spectra from CD_{NP} of buckled side of LH and RH under ε=0% and 50%. **b**, **c**, Calculated *g*-factor spectra from a single chain and an array of five chains, respectively.

Magnitude of *g*-factor: Chiral anisotropy *g*-factor is used as a measure to compare strength of optical activities of chiral systems. *g*-factor of 0.025 for RH, buckled side, under ε = 50% is one of the highest when compared to recently reported examples. Previous publications have disclosed *g*-factors as high as 10^{-2} (refs. [109,112]). One paper reported *g*-factors of ca. 0.3 (ref. [64]) for a special case of solid films obtained by angled deposition of metal.

3.9.14 Computational Simulations

CD spectra with differential absorbance were calculated by solving Maxwell equations using the finite element method (FEM)-based computational simulations, and were then converted into ellipticity. The electromagnetic wave module within COMSOL Multiphysics was used with governing Eq. 3.8 under scattered electric field conditions[152,153]. (ε_r: relative permittivity, μ_r: relative permeability, ε_0: permittivity of a vacuum. σ: conductivity, k_0: free-space wave number, κ: angular frequency)

$$\nabla \times \left(\frac{1}{\mu_r}\nabla \times \mathbf{E}\right) - k_0^2\left(\varepsilon_r - j\frac{\sigma}{\kappa\varepsilon_0}\right)\mathbf{E} = 0 \qquad \text{(Eq. 3.8)}$$

Values of CD as differential absorption at specific wavelengths were calculated by subtracting the extinction cross-section of right-handed circularly polarized light (RCP) from the extinction cross-section of left-handed circularly polarized light (LCP). LCP and RCP are expressed by the following Eq. 3.9 and 3.10 (ref. [154]) where E_0 is the amplitude of the electric field of incident light propagating along +z direction, and k is the wave number.

$$\text{LCP: } \mathbf{E}_L(z) = \frac{E_0}{\sqrt{2}}\left[\mathbf{E}_x e^{-jkz} + \mathbf{E}_y e^{-j\left(kz+\frac{\pi}{2}\right)}\right] \qquad \text{(Eq. 3.9)}$$

$$\text{RCP: } \mathbf{E}_R(z) = \frac{E_0}{\sqrt{2}}\left[\mathbf{E}_x e^{-jkz} + \mathbf{E}_y e^{-j\left(kz-\frac{\pi}{2}\right)}\right] \qquad \text{(Eq. 3.10)}$$

Extinction cross-section (σ_{ext}) is calculated by the sum of absorption cross-section (σ_{abs}) and scattering cross-section (σ_{scat})[152,153], Eq. 3.11. Absorption cross-sections were obtained by integrating resistivity loss (Q_{loss}) over the total volume of the nanoparticles and dividing by incident power flux (P_0), Eq. 3.12. Scattering cross-sections were calculated from integration of the dot product of the time-averaged power flux (Poynting vector, $\boldsymbol{\mathcal{P}}$) and the

surface normal vector (**n**) over the surface of nanoparticles and divided by incident power flux (P_0), Eq. 3.13.

$$\sigma_{ext} = \sigma_{abs} + \sigma_{scat} \qquad \text{(Eq. 3.11)}$$

$$\sigma_{abs} = \iiint_V Q_{loss} dV / P_0 \qquad \text{(Eq. 3.12)}$$

$$\sigma_{scat} = \oiint_S \boldsymbol{\mathcal{P}} \cdot \mathbf{n} dS \, / P_0 \qquad \text{(Eq. 3.13)}$$

The geometry of the chiral structures consists of an array of NPs[138] with a diameter of 13 nm from TEM images (Fig. 3.41). The distance between NPs was calculated to be constant (13.8 nm) for both buckled and cracked sides during stretching deformations from SAXS and TEM experiments (Fig. 3.40 and 3.41). NP chain models are displayed in Fig. 3.11a-d and 3.49. The refractive index (n_e) of the environment was set to be 1 as air. Simulations on left-handed geometries were performed and that of right-handed ones were mathematically calculated. Calculated CD spectra as differential absorption spectra are converted into ellipticity, then normalized by the number of Au NPs in their models and the highest amplitude of CD spectra obtained from ε = 25% models.

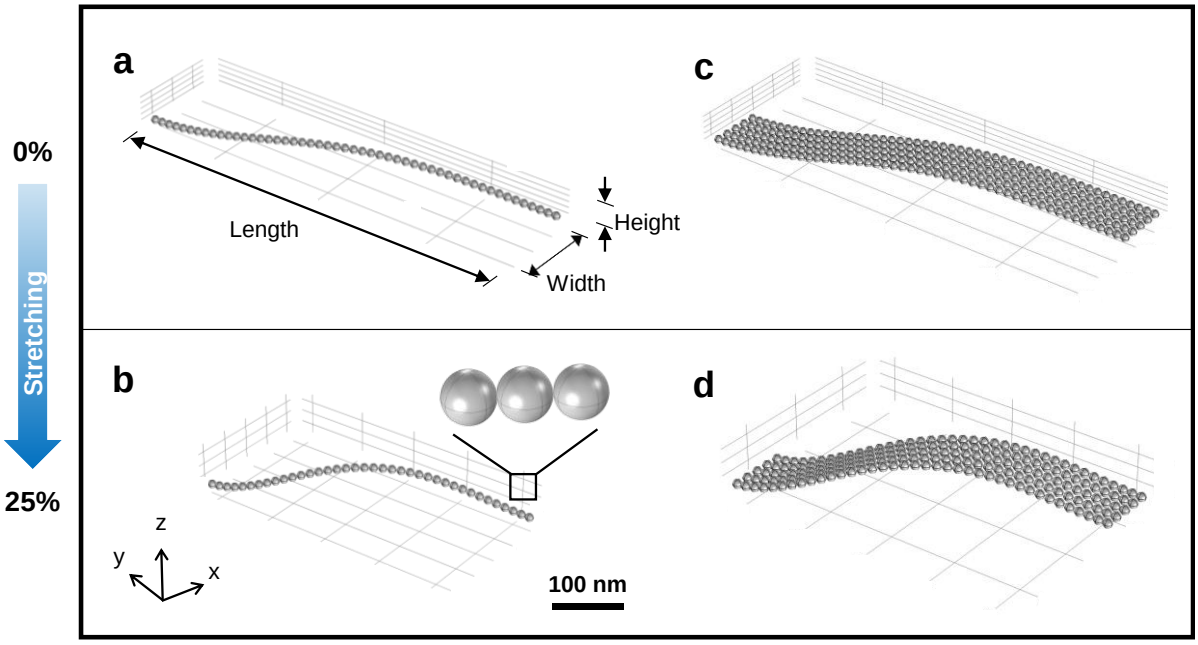

Figure 3.49. Buckled side, right-handed *S*-chains NP models used for simulation. a-d, A single chain and an array of five chains at strains of ε = 0% and ε=25%, respectively, with characteristic dimensions.

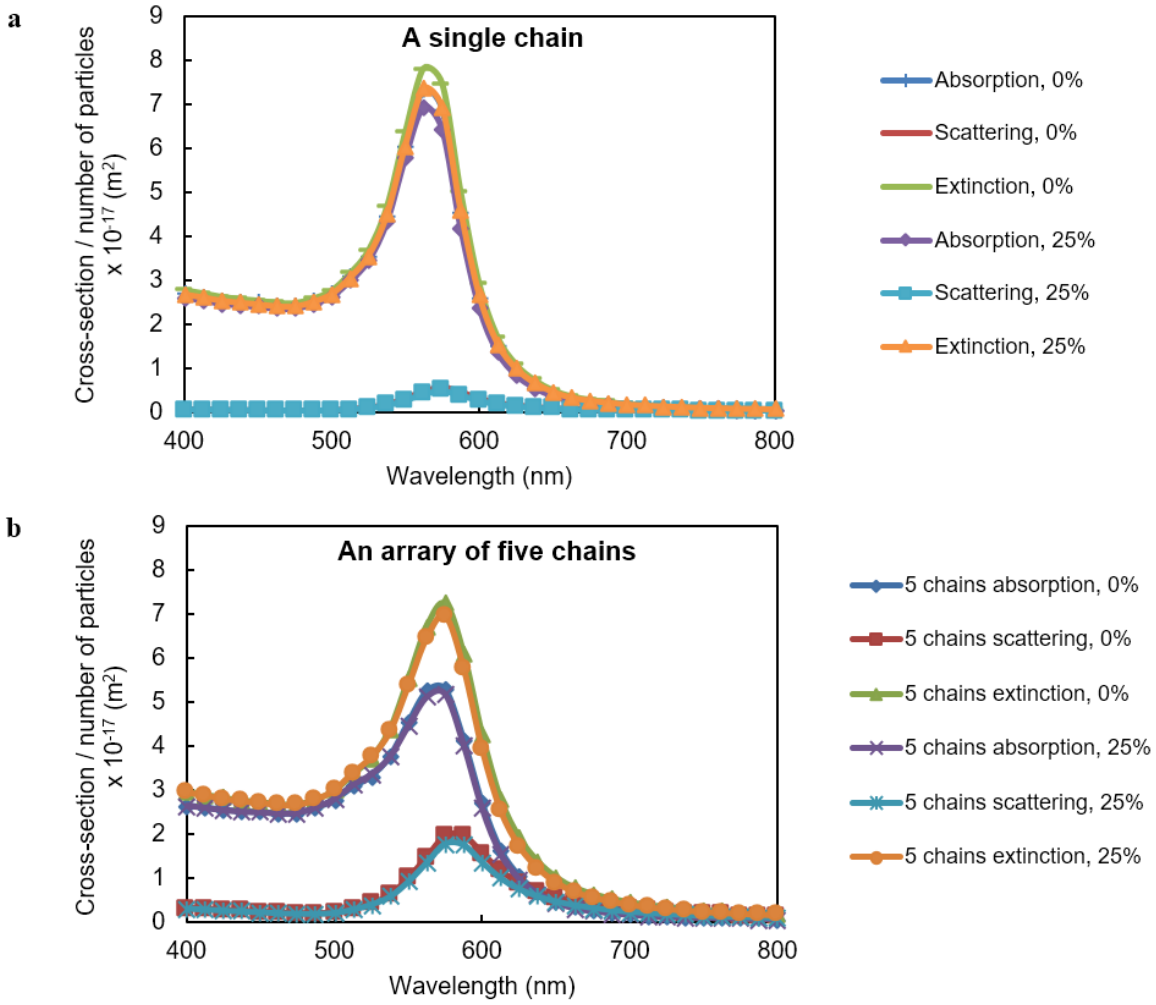

Figure 3.50. Calculated extinction cross-section of the LH buckled side for a single chain (a) and an array of five chains (b). Maximum peaks of extinctions are located near 562 nm and 575 nm for **a** and **b**, respectively.

CHAPTER IV

Conclusion and Future Directions

4.1 Conclusion

The field of nanotechnology developed tremendously during the past three decades in terms of fundamental understandings and practical applications for a number of independent fields. Interdisciplinary research triggered by innovation, is now heading towards converging technology, which has a holistic perspective. We focus on the fact that the facile and versatile LBL assembly methodology inherently has a holistic view toward science especially in terms of the wide variety of materials which can be incorporated/deposited and the breadth of possibilities for geometries and thereby unlimited functionalities. Fundamentals and technologies of LBL assembly hare comprehensively understood. This mature technology is now ready for transformative technical applications. This close interrelation between LBL assembly and converging technology presents enormous opportunities. The research presented in this work demonstrates LBL-assembled composites applicability as high performance multifunctional materials for converging technologies. Those applications allow facile control over compositions, structures, alignments and interfacial interactions.

In chapter II, we demonstrated how self-organized NPs can make excellent conducting pathways in both LBL and VAF composites. Mechanical and electrical properties of LBL and VAF were compared by structure-properties relations. Conductivity of LBL composites was further analyzed by percolation theory. Conducting NP networks formed during tensile stretching, had higher conductivity than theoretical predictions by percolation theory. The

high electron density and mobility from metallic filler particles offered additional practical use of the composites for voltage-controlled damping of vibration. We witnessed greater freedom of NP arrangement upon external stress, and this fundamental understanding has been applied to find unique optical activity utilizing plasmonic resonance of NP assemblies.

In chapter III, we demonstrated NPs can be organized into a three dimensional S-shape in order to become geometrically chiral. NP layers deposited on stressed, pre-accumulated substrates obtained chiral geometries and upon release of the stress returned to planar geometries. The chiral chain patterns obtained from the processes were reversibly tunable by elastic deformation of substrates, which accordingly tuned the polarization rotation of transmitted photons. We also addressed universality of the macro-to-nano chirality transfer method by showing that 3D S-patterns can be obtained from SWNTs and polymeric nanobeads. This new family of composites, with respect to mechanics and optics with low-cost manufacturability, scalability, uniformity, tunability, and optical homogeneity, provides a new perspective towards converging technology of reconfigurable photonic materials.

In summary, this dissertation is devoted to developing converging technologies using LBL-assembled composites. This dissertation is interdisciplinary study that ranges over chemical engineering, chemistry, nanotechnology, materials science, electronics, mechanics, and optics, and is corroborated by computational simulations and mathematical analysis. First, we prepared unique nanocomposites combining inorganic functional fillers in a polymeric matrix. Then, we proved that the nanofillers in the matrix can be reorganized upon external stress, which induced enhanced electrical conductivity and chirooptical activity with

reconfigurability. We further addressed the universality of the self-organization of NPs from fillers of SWNTs and polymeric beads.

4.2 Future Directions

Although we have created the design framework for the re-organization phenomena of Au NPs and SWNTs composites, many other aspects of the nanocomposites are still unexplored. Systematic study, changing parameters such as aspect ratio of NPs, electronic state of NPs (band gap), effect of different surface ligands, and molecular weight of polymer matrix, is a natural direction for our work. Extension of our findings to other nanomaterials, e.g. quantum dots, metallic nanorods, graphene and graphite sheets, magnetic NPs, or other natural/synthetic nanomaterials, is another interesting direction.

Even though we proved self-organization of NPs for advanced electrical and optical properties, there are more outstanding opportunities that need to be addressed. For example, battery electrodes and membranes (electrochemical), neural probes (nano-bio interface, neural) and drug carriers (bio) are the areas where converging nanotechnology can make significant strides. The qualities of LBL assemblies, such as their ability to construct highly integrated multilayer structures[33], their non-toxic water-based nature[29], their ability to work at room temperature, and the fact that they lend themselves to large scale production at a low cost with a short preparation time[13], are proving invaluable when addressing these areas. For instance, electronic and energy materials require qualities of high electron and ion exchange rate. Further, in the case of neural probes, the high temperature required by chemical vapor

deposition restrains the choice of materials considerably limiting performance[6]. Also, pharmacological applications will be benefited from a purely aqueous means for creating drug-carrier complexes[35].

After systematic understanding of re-organization phenomena and application into cross-related fields (electrochemical, bio, and neural) real impact may be found from commercialization of these materials. Inherent features of LBL assembly, such as simple, fast and low-cost processing operations, will likely be very helpful for commercialization. There are also several challenges in adapting the means of processing LBL films to achieve rapid assembly and maintain, or possibly increase, the control and flexibility of this approach. These efforts will lead LBL technologies toward ultimate translation in the commercial realm, and to new discoveries in cross-cutting fields of research.

In the end, the tremendous diversity of the available pool of nanocolloids and the versatility of the LBL assembly to combine multiple components into user-defined architectures, holds unlimited possibilities for converging materials design and research for many years to come.

BIBLIOGRAPHY

1. Roco, M. C. & Bainbridge, W. S. Converging technologies for improving human performance: Integrating from the nanoscale. *J. Nanoparticle Res.* **4,** 281–295 (2002).
2. Roco, M. C. The long view of nanotechnology development: the National Nanotechnology Initiative at 10 years. *J. Nanoparticle Res.* (2011). doi:10.1007/s11051-010-0192-z
3. Ozbay, E. Plasmonics: Merging Photonics and Electronics at Nanoscale Dimensions. *Science (80-.).* (2006).
4. Sahoo, S. K., Parveen, S. & Panda, J. J. The present and future of nanotechnology in human health care. *Nanomedicine Nanotechnology, Biol. Med.* (2007). doi:10.1016/j.nano.2006.11.008
5. Tarascon, J.-M. & Armand, M. Issues and challenges facing rechargeable lithium batteries. *Nature* **414,** 359–367 (2001).
6. Gatzen, H. H., Saile, V. & Leuthold, J. *Micro and Nano Fabrication, Tools and Processes*. (Springer-Verlag Berlin Heidelberg, 2015). doi:10.1007/978-3-662-44395-8
7. Decher, G., Eckle, M., Schmitt, J. & Struth, B. Layer-by-layer assembled multicomposite films. *Curr. Opin. Colloid Interface Sci.* **3,** 32–39 (1998).
8. Hammond, P. T. Form and Function in Multilayer Assembly: New Applications at the Nanoscale. *Adv. Mater.* **16,** 1271–1293 (2004).
9. Caruso, F. Nanoengineering of particle surfaces. *Adv. Mater.* **13,** 11–22 (2001).
10. Srivastava, S. & Kotov, N. Composite Layer-by-Layer (LBL) Assembly with Inorganic Nanoparticles and Nanowires. *Semicond. Nanocrystal Quantum Dots Synth. Assem. Spectrosc. Appl.* **41,** 197–216 (2008).
11. Decher, G. Buildup of ultrathin multilayer films by a self-assembly process: III. Consecutively alternating adsorption of anionic and cationic polyelectrolytes on charged surfaces. *Thin Solid Films* **210-211,** 831–835 (1991).
12. Nogueira, G. M., Banerjee, D., Cohen, R. E. & Rubner, M. F. Spray-Layer-by-Layer Assembly Can More Rapidly Produce Optical-Quality Multistack Heterostructures.

(2011). doi:10.1021/la200790g

13. Krogman, K. C., Cohen, R. E., Hammond, P. T., Rubner, M. F. & Wang, B. N. Industrial-scale spray layer-by-layer assembly for production of biomimetic photonic systems. *Bioinspir. Biomim.* **8,** 045005 (2013).
14. http://www.elegustech.com/ Elegus Technologies is commercializing an aramid nanofiber based battery separator, developed at the Kotov lab, Chemical Engineering, University of Michigan.
15. Fendler, J. H. Self-Assembled Nanostructured Materials. *Chem. Mater.* **8,** 1616–1624 (1996).
16. Hammond, P. T. Recent explorations in electrostatic multilayer thin film assembly. *Curr. Opin. Colloid Interface Sci.* (2000).
17. Ariga, K., Hill, J. P. & Ji, Q. Layer-by-layer assembly as a versatile bottom-up nanofabrication technique for exploratory research and realistic application. *Phys. Chem. Chem. Phys.* **9,** 2319 (2007).
18. Lee, D., Rubner, M. F. & Cohen, R. E. All-nanoparticle thin-film coatings. *Nano Lett.* **6,** 2305–2312 (2006).
19. Lee, S. W., Kim, B.-S., Chen, S., Shao-Horn, Y. & Hammond, P. T. Layer-by-Layer Assembly of All Carbon Nanotube Ultrathin Films for Electrochemical Applications. *JACS* (2008). doi:10.1021/ja807059k
20. Kim, B.-S., Park, W. & Hammond, P. T. Hydrogen-Bonding Layer-by-Layer-Assembled Biodegradable Polymeric Micelles as Drug Delivery Vehicles from Surfaces. *ACS Nano* (2008). doi:10.1021/nn700408z
21. Such, G. K., Johnston, A. P. R. & Caruso, F. Engineered hydrogen-bonded polymer multilayers: from assembly to biomedical applications. *Chem. Soc. Rev.* **40,** 19–29 (2011).
22. Bergbreiter, D. E. & Liao, K.-S. Covalent layer-by-layer assembly—an effective, forgiving way to construct functional robust ultrathin films and nanocomposites. *Soft Matter* **5,** 23 (2009).
23. Kotov, N. a. Layer-by-layer self-assembly: The contribution of hydrophobic interactions. *NanoStructured Mater.* **12,** 789–796 (1999).

24. Ochs, C. J., Such, G. K., Yan, Y., Van Koeverden, M. P. & Caruso, F. Biodegradable click capsules with engineered drug-loaded multilayers. *ACS Nano* **4,** 1653–1663 (2010).
25. Hsu, B. B. *et al.* Ordered and Kinetically Discrete Sequential Protein Release from Biodegradable Thin Films. *Angew. Chemie* (2014). doi:10.1002/ange.201403702
26. John F. Quinn, Angus P. R. Johnston, Georgina K. Such, A. N. Z. and F. C. Next generation, sequentially assembled ultrathin films: beyond electrostatics. *Chem. Soc. Rev.* (2007).
27. Quinn, J. F., Johnston, A. P. R., Such, G. K., Zelikin, A. N. & Caruso, F. Next generation, sequentially assembled ultrathin films: beyond electrostatics. *Chem. Soc. Rev.* **36,** 707–718 (2007).
28. Zhang, X., Chen, H. & Zhang, H. Layer-by-layer assembly: from conventional to unconventional methods. *Chem. Commun.* 1395–1405 (2007). doi:10.1039/B615590A
29. Tang, Z., Wang, Y., Podsiadlo, P. & Kotov, N. a. Biomedical applications of layer-by-layer assembly: From biomimetics to tissue engineering. *Adv. Mater.* **18,** 3203–3224 (2006).
30. Jiang, C. & Tsukruk, V. V. Freestanding nanostructures via layer-by-layer assembly. *Adv. Mater.* **18,** 829–840 (2006).
31. Izquierdo, a., Ono, S. S., Voegel, J. C., Schaaf, P. & Decher, G. Dipping versus spraying: Exploring the deposition conditions for speeding up layer-by-layer assembly. *Langmuir* **21,** 7558–7567 (2005).
32. Richardson, J. J., Mattias, B. & Caruso, F. Technology-driven layer-by-layer assembly of nanofilms. *Science (80-.).* **348,** aaa2491–aaa2491 (2015).
33. Lutkenhaus, J. L. & Hammond, P. T. Electrochemically enabled polyelectrolyte multilayer devices: from fuel cells to sensors. (2007). doi:10.1039/b701203a
34. Kildishev, A. V., Boltasseva, A. & Shalaev, V. M. Planar Photonics with Metasurfaces. *Science (80-.).* **339,** 1232009 (2013).
35. Hammond, P. T. Building biomedical materials layer-by-layer. *Mater. Today* **15,** 196–206 (2012).
36. Whitesides, G. M. & Grzybowski, B. Self-assembly at all scales. *Science* **295,** 2418–21

(2002).

37. Whitesides, G. M. & Boncheva, M. Beyond molecules: self-assembly of mesoscopic and macroscopic components. *Proc. Natl. Acad. Sci. U. S. A.* **99,** 4769–74 (2002).
38. Self-Assembly and Nanotechnology: A Force Balance Approach - Yoon S. Lee. at <http://www.wiley.com/WileyCDA/WileyTitle/productCd-0470248831.html>
39. Silvera Batista, C. A., Larson, R. G. & Kotov, N. A. Nonadditivity of nanoparticle interactions. *Science (80-.).* **350,** 1242477–1242477 (2015).
40. Liu, Y., Wang, Y. & Claus, R. O. Layer-by-layer ionic self-assembly of Au colloids into multilayer thin-films with bulk metal conductivity. *Chem. Phys. Lett.* **298,** 315–319 (1998).
41. Kumlangdudsana, P., Tuantranont, A., Dubas, S. T. & Dubas, L. Fabrication of microelectrodes using flow layer-by-layer self assembly of gold nanoparticles. *Superlattices Microstruct.* **52,** 1043–1051 (2012).
42. Basarir, F. & Yoon, T.-H. Sonication-assisted layer-by-layer deposition of gold nanoparticles for highly conductive gold patterns. *Ultrason. Sonochem.* **19,** 621–6 (2012).
43. Basarir, F. & Yoon, T.-H. Preparation of highly conductive gold patterns on polyimide via shaking-assisted layer-by-layer deposition of gold nanoparticles. *Colloids Surfaces A Physicochem. Eng. Asp.* **393,** 27–31 (2012).
44. Olichwer, N., Leib, E. W., Halfar, A. H., Petrov, A. & Vossmeyer, T. Cross-linked gold nanoparticles on polyethylene: resistive responses to tensile strain and vapors. *ACS Appl. Mater. Interfaces* **4,** 6151–61 (2012).
45. Joseph, Y. *et al.* Self-Assembled Gold Nanoparticle/Alkanedithiol Films: Preparation, Electron Microscopy, XPS-Analysis, Charge Transport, and Vapor-Sensing Properties †. *J. Phys. Chem. B* **107,** 7406–7413 (2003).
46. Decher, G. Fuzzy Nanoassemblies: Toward Layered Polymeric Multicomposites. *Science (80-.).* **277,** 1232–1237 (1997).
47. Mamedov, A. A. *et al.* Molecular design of strong single-wall carbon nanotube/polyelectrolyte multilayer composites. *Nat. Mater.* **1,** 190–4 (2002).
48. Rogers, J. A., Someya, T. & Huang, Y. Materials and Mechanics for Stretchable

Electronics. *Science (80-.).* (2010).

49. Ahn, J.-H. & Je, J. H. Stretchable electronics: materials, architectures and integrations. *J. Phys. D. Appl. Phys.* **45,** 103001 (2012).
50. Sekitani, T. & Someya, T. Stretchable, Large-area Organic Electronics. *Adv. Mater.* **22,** 2855–2855 (2010).
51. Park, S., Vosguerichian, M. & Bao, Z. A review of fabrication and applications of carbon nanotube film-based flexible electronics. *Nanoscale* **5,** 1727 (2013).
52. Sekitani, T. *et al.* A rubberlike stretchable active matrix using elastic conductors. *Science* **321,** 1468–72 (2008).
53. Sekitani, T. *et al.* Stretchable active-matrix organic light-emitting diode display using printable elastic conductors. *Nat. Mater.* **8,** 494–499 (2009).
54. Lipomi, D. J. & Bao, Z. Skin-like pressure and strain sensors based on transparent elastic films of carbon nanotubes. *Nat. Nanotechnol.* **6,** 788–792 (2011).
55. Kim, Y. *et al.* Stretchable nanoparticle conductors with self-organized conductive pathways. *Nature* **500,** 59–63 (2013).
56. Zhang, Y. *et al.* A mechanically driven form of Kirigami as a route to 3D mesostructures in micro/nanomembranes. *Proc. Natl. Acad. Sci.* **112,** 201515602 (2015).
57. Blees, M. K. *et al.* Graphene kirigami. *Nature* (2015). doi:10.1038/nature14588
58. Shyu, T. C. *et al.* A kirigami approach to engineering elasticity in nanocomposites through patterned defects. *Nat. Mater.* **14,** 785–789 (2015).
59. Lamoureux, A., Lee, K., Shlian, M., Forrest, S. R. & Shtein, M. Dynamic kirigami structures for integrated solar tracking. *Nat. Commun.* **6,** 8092 (2015).
60. Zhu, J., Shim, B. S., Di Prima, M. & Kotov, N. a. Transparent conductors from carbon nanotubes LBL-assembled with polymer dopant with π-π Electron transfer. *J. Am. Chem. Soc.* **133,** 7450–7460 (2011).
61. Pendry, J. B. A chiral route to negative refraction. *Science (80-.).* **306,** 1353–1355 (2004).
62. Zheludev, N. I. & Kivshar, Y. S. From metamaterials to metadevices. *Nat. Mater.* **11,** 917–924 (2012).

63. Hendry, E. *et al.* Ultrasensitive detection and characterization of biomolecules using superchiral fields. *Nat. Nanotechnol.* **5,** 783–787 (2010).
64. Yang, Y., da Costa, R. C., Fuchter, M. J. & Campbell, A. J. Circularly polarized light detection by a chiral organic semiconductor transistor. *Nat. Photonics* **7,** 634–638 (2013).
65. Mark, A. G., Gibbs, J. G., Lee, T.-C. & Fischer, P. Hybrid nanocolloids with programmed three-dimensional shape and material composition. *Nat. Mater.* **12,** 802–807 (2013).
66. Kuzyk, A. *et al.* DNA-based self-assembly of chiral plasmonic nanostructures with tailored optical response. *Nature* **483,** 311–314 (2012).
67. Tao, A., Sinsermsuksakul, P. & Yang, A. P. Tunable plasmonic lattices of silver nanocrystals. *Nat. Nanotechnol.* (2007). doi:10.1038/nnano.2007.189
68. Tao, A. R., Ceperley, D. P., Sinsermsuksakul, P., Neureuther, A. R. & Yang, P. Self-Organized Silver Nanoparticles for Three-Dimensional Plasmonic Crystals. *Nano Lett* (2008). doi:10.1021/nl802877h
69. Lin, M.-H., Chen, H.-Y. & Gwo, S. Layer-by-Layer Assembly of Three-Dimensional Colloidal Supercrystals with Tunable Plasmonic Properties. *JACS* (2010). doi:10.1021/ja103722p
70. Cunningham, A., Uhlig, S. M., Rockstuhl, C. & B€ Urgi, T. Coupling of Plasmon Resonances in Tunable Layered Arrays of Gold Nanoparticles. *J. Phys. Chem. C* **115,** 8955–8960 (2011).
71. Kim, Y. *et al.* Reconfigurable chiroptical nanocomposites with chirality transfer from the macro- to the nanoscale. *Nat. Mater.* (2016). doi:10.1038/NMAT4525
72. Rogers, J. A., Someya, T. & Huang, Y. Materials and Mechanics for Stretchable Electronics. *Science (80-.).* **327,** 1603–1608 (2010).
73. Fan, Z. *et al.* Toward the Development of Printable Nanowire Electronics and Sensors. *Adv. Mater.* **21,** 3730–3743 (2009).
74. Nolfi, S. & Floreano, D. *Evolutionary Robotics: The Biology, Intelligence, and Technology of Self-organizing Machines*. **00,** (MIT Press, 2000).
75. Torquato, S., Hyun, S. & Donev, A. Multifunctional composites: optimizing

microstructures for simultaneous transport of heat and electricity. *Phys. Rev. Lett.* **89,** 266601 (2002).

76. Baughman, R. H., Zakhidov, A. A. & de Heer, W. A. Carbon nanotubes--the route toward applications. *Science* **297,** 787–92 (2002).
77. Lee, P. *et al.* Highly stretchable and highly conductive metal electrode by very long metal nanowire percolation network. *Adv. Mater.* **24,** 3326–32 (2012).
78. Hu, L. *et al.* Stretchable, porous, and conductive energy textiles. *Nano Lett.* **10,** 708–14 (2010).
79. Chun, K.-Y. & Baik, S. Highly conductive, printable and stretchable composite films of carbon nanotubes and silver. *Nat. Nanotechnol.* **5,** 853–857 (2010).
80. Fuhrer, M. S. Crossed Nanotube Junctions. *Science (80-.).* **288,** 494–497 (2000).
81. Zhang, Y. *et al.* Polymer-embedded carbon nanotube ribbons for stretchable conductors. *Adv. Mater.* **22,** 3027–31 (2010).
82. Liu, K. *et al.* Cross-Stacked Superaligned Carbon Nanotube Films for Transparent and Stretchable Conductors. *Adv. Funct. Mater.* **21,** 2721–2728 (2011).
83. Recent Advances in Elastomeric Nanocomposites | Vikas Mittal | Springer. at <http://www.springer.com/us/book/9783642157868>
84. Yu, C., Masarapu, C., Rong, J., Wei, B. & Jiang, H. Stretchable supercapacitors based on buckled single-walled carbon-nanotube macrofilms. *Adv. Mater.* **21,** 4793–7 (2009).
85. Xu, F., Wang, X., Zhu, Y. & Zhu, Y. Wavy Ribbons of Carbon Nanotubes for Stretchable Conductors. *Adv. Funct. Mater.* **22,** 1279–1283 (2012).
86. Kim, D.-H. *et al.* Materials and noncoplanar mesh designs for integrated circuits with linear elastic responses to extreme mechanical deformations. *Proc. Natl. Acad. Sci. U. S. A.* **105,** 18675–80 (2008).
87. Park, J. *et al.* Three-dimensional nanonetworks for giant stretchability in dielectrics and conductors. *Nat. Commun.* **3,** 916 (2012).
88. Schlicke, H. *et al.* Freestanding films of crosslinked gold nanoparticles prepared via layer-by-layer spin-coating. *Nanotechnology* **22,** 305303 (2011).
89. Tang, Z., Kotov, N. A., Magonov, S. & Ozturk, B. Nanostructured artificial nacre. *Nat. Mater.* **2,** 413–8 (2003).

90. Podsiadlo, P. *et al.* LBL assembled laminates with hierarchical organization from nano- to microscale: high-toughness nanomaterials and deformation imaging. *ACS Nano* **3,** 1564–72 (2009).
91. Reuter, T. *et al.* Two-Dimensional Networks via Quasi One-Dimensional Arrangements of Gold Clusters. *Nano Lett.* **2,** 709–711 (2002).
92. Li, J. *et al.* Correlations between Percolation Threshold, Dispersion State, and Aspect Ratio of Carbon Nanotubes. *Adv. Funct. Mater.* **17,** 3207–3215 (2007).
93. Dirix, Y., Bastiaansen, C., Caseri, W. & Smith, P. Oriented Pearl-Necklace Arrays of Metallic Nanoparticles in Polymers: A New Route Toward Polarization-Dependent Color Filters. *Adv. Mater.* **11,** 223–227 (1999).
94. Pérez-Juste, J., Rodríguez-González, B., Mulvaney, P. & Liz-Marzán, L. M. Optical Control and Patterning of Gold-Nanorod-Poly(vinyl alcohol) Nanocomposite Films. *Adv. Funct. Mater.* **15,** 1065–1071 (2005).
95. Li, J. & Kim, J.-K. Percolation threshold of conducting polymer composites containing 3D randomly distributed graphite nanoplatelets. *Compos. Sci. Technol.* **67,** 2114–2120 (2007).
96. Park, M. *et al.* Highly stretchable electric circuits from a composite material of silver nanoparticles and elastomeric fibres. *Nat. Nanotechnol.* **7,** 803–9 (2012).
97. Mott, N. F. Conduction in non-crystalline materials. *Philos. Mag.* (2006). at <http://www.tandfonline.com/doi/abs/10.1080/14786436908216338>
98. Ma, Y. G., Liu, H. J. & Ong, C. K. Electron transport properties in CoAlO composite antidot arrays. *Europhys. Lett.* **76,** 1144–1150 (2006).
99. Kao, K.-C. & Hwang, W. *Electrical transport in solids : with particular reference to organic semiconductors*. (Taylor & Francis Group, 1981). at <http://www.tandfonline.com/doi/abs/10.1080/01418638108223774>
100. Jin, H.-J. & Weissmüller, J. A material with electrically tunable strength and flow stress. *Science* **332,** 1179–82 (2011).
101. Stauffer, D. & Aharony, A. *Introduction To Percolation Theory*. **6,** (CRC Press, 1994).
102. Scher, H. Critical Density in Percolation Processes. *J. Chem. Phys.* **53,** 3759 (1970).
103. Pasteur, L. Mémoire sur la relation qui peut exister entre la forme cristalline et la

composition chimique, et sur la cause de la polarisation rotatoire. *C. R. Acad. Sci. Paris* **26,** 535–538 (1848).

104. Chen, W. *et al.* Nanoparticle superstructures made by polymerase chain reaction: collective interactions of nanoparticles and a new principle for chiral materials. *Nano Lett.* **9,** 2153–9 (2009).
105. Peng, X. *et al.* Optically active single-walled carbon nanotubes. *Nat. Nanotechnol.* **2,** 361–5 (2007).
106. Yeom, J. *et al.* Chiral templating of self-assembling nanostructures by circularly polarized light. *Nat. Mater.* **14,** 66–72 (2015).
107. Govorov, A. O., Fan, Z., Hernandez, P., Slocik, J. M. & Naik, R. R. Theory of Circular Dichroism of Nanomaterials Comprising Chiral Molecules and Nanocrystals: Plasmon Enhancement, Dipole Interactions, and Dielectric Effects. *Nano Lett.* **10,** 1374–1382 (2010).
108. Valev, V. K., Baumberg, J. J., Sibilia, C. & Verbiest, T. Chirality and Chiroptical Effects in Plasmonic Nanostructures: Fundamentals, Recent Progress, and Outlook. *Adv. Mater.* **25,** 2517–2534 (2013).
109. Fedotov, V. A., Schwanecke, A. S., Zheludev, N. I., Khardikov, V. V. & Prosvirnin, S. L. Asymmetric Transmission of Light and Enantiomerically Sensitive Plasmon Resonance in Planar Chiral Nanostructures. *Nano Lett.* **7,** 1996–1999 (2007).
110. Schaaff, T. G. & Whetten, R. L. Giant Gold−Glutathione Cluster Compounds: Intense Optical Activity in Metal-Based Transitions. *J. Phys. Chem. B* **104,** 2630–2641 (2000).
111. Song, C. *et al.* Tailorable plasmonic circular dichroism properties of helical nanoparticle superstructures. *Nano Lett.* **13,** 3256–61 (2013).
112. Guerrero-Martínez, A. *et al.* Intense optical activity from three-dimensional chiral ordering of plasmonic nanoantennas. *Angew. Chem. Int. Ed. Engl.* **50,** 5499–503 (2011).
113. Liu, S. *et al.* Synthesis of chiral TiO_2 nanofibre with electron transition-based optical activity. *Nat. Commun.* **3,** 1215 (2012).
114. Gansel, J. K. *et al.* Gold Helix Photonic Metamaterial as Broadband Circular Polarizer. *Science (80-.).* **1513,** 1513–1515 (2011).

115. Frank, B. *et al.* Large-area 3D chiral plasmonic structures. *ACS Nano* **7,** 6321–9 (2013).
116. Yeom, B. *et al.* Chiral plasmonic nanostructures on achiral nanopillars. *Nano Lett.* **13,** 5277–83 (2013).
117. Zhao, Y. *et al.* Shell-engineered chiroplasmonic assemblies of nanoparticles for zeptomolar DNA detection. *Nano Lett.* **14,** 3908–13 (2014).
118. Li, Z. *et al.* Reversible plasmonic circular dichroism of Au nanorod and DNA assemblies. *J. Am. Chem. Soc.* **134,** 3322–5 (2012).
119. Schreiber, R. *et al.* Chiral plasmonic DNA nanostructures with switchable circular dichroism. *Nat. Commun.* **4,** 2948 (2013).
120. Ma, W. *et al.* Chiral plasmonics of self-assembled nanorod dimers. *Sci. Rep.* **3,** 1934 (2013).
121. Hu, T. *et al.* Self-organization of plasmonic and excitonic nanoparticles into resonant chiral supraparticle assemblies. *Nano Lett.* **14,** 6799–810 (2014).
122. Arruda, E. M. & Boyce, M. C. A three-dimensional constitutive model for the large stretch behavior of rubber elastic materials. *J. Mech. Phys. Solids* **41,** 389–412 (1993).
123. Mooney, M. A Theory of Large Elastic Deformation. *J. Appl. Phys.* **11,** 582 (1940).
124. Rivlin, R. S. Large Elastic Deformations of Isotropic Materials. IV. Further Developments of the General Theory. *Philos. Trans. R. Soc. A Math. Phys. Eng. Sci.* **241,** 379–397 (1948).
125. Yeoh, O. H. Some Forms of the Strain Energy Function for Rubber. *Rubber Chem. Technol.* **66,** 754–771 (1993).
126. Timoshenko, S. P. *Strength of Materials: Part 1-Elementary, Volumes 2-3*. (Van Nostrand Reinhold Company, 1958). at <https://books.google.com/books?id=6voengEACAAJ&pgis=1>
127. Govorov, A. O. & Fan, Z. Theory of chiral plasmonic nanostructures comprising metal nanocrystals and chiral molecular media. *Chemphyschem* **13,** 2551–60 (2012).
128. Zhang, H. & Govorov, A. O. Giant circular dichroism of a molecule in a region of strong plasmon resonances between two neighboring gold nanocrystals. *Phys. Rev. B* **87,** 075410 (2013).

129. Ben-Moshe, A. *et al.* Enantioselective control of lattice and shape chirality in inorganic nanostructures using chiral biomolecules. *Nat. Commun.* **5,** 4302 (2014).
130. Arteaga, O., Freudenthal, J., Wang, B. & Kahr, B. Mueller matrix polarimetry with four photoelastic modulators: theory and calibration. *Appl. Opt.* **51,** 6805–17 (2012).
131. Arteaga, O. Number of independent parameters in the Mueller matrix representation of homogeneous depolarizing media. *Opt. Lett.* **38,** 1131–3 (2013).
132. Ossikovski, R. & Arteaga, O. Statistical meaning of the differential Mueller matrix of depolarizing homogeneous media. *Opt. Lett.* **39,** 4470–3 (2014).
133. Arteaga, O. & Canillas, A. Analytic inversion of the Mueller-Jones polarization matrices for homogeneous media. *Opt. Lett.* **35,** 559–61 (2010).
134. Lu, S.-Y. & Chipman, R. A. Interpretation of Mueller matrices based on polar decomposition. *J. Opt. Soc. Am. A* **13,** 1106 (1996).
135. Coxeter, H. S. M. *Introduction to Geometry*. (Wiley, 1989). at <https://books.google.com/books?id=N8i1QgAACAAJ&pgis=1>
136. Pettofrezzo, A. J. *Matrices and Transformations*. (Courier Corporation, 2012). at <https://books.google.com/books?id=JlPCAgAAQBAJ&pgis=1>
137. Gilbert, P. Iterative methods for the three-dimensional reconstruction of an object from projections. *J. Theor. Biol.* **36,** 105–117 (1972).
138. Johnson, P. B. & Christy, R. W. Optical Constants of the Noble Metals. *Phys. Rev. B* **6,** 4370–4379 (1972).
139. Kuroda, R., Harada, T. & Shindo, Y. A solid-state dedicated circular dichroism spectrophotometer: Development and application. *Rev. Sci. Instrum.* **72,** 3802 (2001).
140. Shindo, Y. Application of polarized modulation technique in polymer science. *Opt. Eng.* **34,** 3369 (1995).
141. Hentschel, M., Schäferling, M., Weiss, T., Liu, N. & Giessen, H. Three-dimensional chiral plasmonic oligomers. *Nano Lett.* **12,** 2542–7 (2012).
142. Abdulrahman, N. A. *et al.* Induced chirality through electromagnetic coupling between chiral molecular layers and plasmonic nanostructures. *Nano Lett.* **12,** 977–83 (2012).
143. Link, S. & El-Sayed, M. A. Size and Temperature Dependence of the Plasmon Absorption of Colloidal Gold Nanoparticles. *J. Phys. Chem. B* **103,** 4212–4217 (1999).

144. Jain, P. K., Lee, K. S., El-Sayed, I. H. & El-Sayed, M. A. Calculated absorption and scattering properties of gold nanoparticles of different size, shape, and composition: applications in biological imaging and biomedicine. *J. Phys. Chem. B* **110,** 7238–48 (2006).

145. Link, S. & El-Sayed, M. a. Shape and size dependence of radiative, non-radiative and photothermal properties of gold nanocrystals. *Int. Rev. Phys. Chem.* **19,** 409–453 (2000).

146. Doremus, R. H. Optical Properties of Small Gold Particles. *J. Chem. Phys.* **40,** 2389 (1964).

147. Sönnichsen, C., Franzl, T., Wilk, T., Plessen, G. von & Feldmann, J. Plasmon resonances in large noble-metal clusters. *New J. Phys.* **4,** 93–93 (2002).

148. DeLongchamp, D. M. & Hammond, P. T. Multiple-Color Electrochromism from Layer-by-Layer-Assembled Polyaniline/Prussian Blue Nanocomposite Thin Films. *Chem. Mater.* **16,** 4799–4805 (2004).

149. Podsiadlo, P. *et al.* Layer-by-layer assembled films of cellulose nanowires with antireflective properties. *Langmuir* **23,** 7901–6 (2007).

150. Genzer, J. & Groenewold, J. Soft matter with hard skin: From skin wrinkles to templating and material characterization. *Soft Matter* **2,** 310 (2006).

151. Volynskii, A. L., Bazhenov, S., Lebedeva, O. V., Ozerin, A. N. & Bakeev, N. F. Multiple cracking of rigid platinum film covering polymer substrate. *J. Appl. Polym. Sci.* **72,** 1267–1275 (1999).

152. Jin, J.-M. *The Finite Element Method in Electromagnetics*. (Wiley, 2014). at <https://books.google.com/books?hl=en&lr=&id=64xPAwAAQBAJ&pgis=1>

153. Cheng, D. K. *Field and Wave Electromagnetics*. (Pearson Education, Limited, 2013). at <https://books.google.com/books?id=nQFKngEACAAJ&pgis=1>

154. Kenyon, I. R. *The Light Fantastic: A Modern Introduction to Classical and Quantum Optics*. (Oxford University Press, 2008). at <https://books.google.com/books?id=piTeWaYb-LEC&pgis=1>

155. Yan, W. *et al.* Self-assembly of chiral nanoparticle pyramids with strong R/S optical activity. *J. Am. Chem. Soc.* **134,** 15114–21 (2012).

156. Plum, E., Fedotov, V. A., Schwanecke, A. S., Zheludev, N. I. & Chen, Y. Giant optical gyrotropy due to electromagnetic coupling. *Appl. Phys. Lett.* **90,** 223113 (2007).